Retrieval of Aerosol Optical Depth Over Land by Inverse Modeling of Multi-Source Satellite Data

Wu, Yerong

DOI
10.4233/uuid:21d34d79-fc42-429d-860f-e6d17e0ca635

Publication date
2018

Document Version
Final published version

Citation (APA)
Wu, Y. (2018). *Retrieval of Aerosol Optical Depth Over Land by Inverse Modeling of Multi-Source Satellite Data*. [Dissertation (TU Delft), Delft University of Technology]. https://doi.org/10.4233/uuid:21d34d79-fc42-429d-860f-e6d17e0ca635

Important note
To cite this publication, please use the final published version (if applicable).
Please check the document version above.

Retrieval of Aerosol Optical Depth Over Land by Inverse Modeling of Multi-Source Satellite Data

Retrieval of Aerosol Optical Depth Over Land by Inverse Modeling of Multi-Source Satellite Data

Proefschrift

ter verkrijging van de graad van doctor
aan de Technische Universiteit Delft,
op gezag van de Rector Magnificus prof. dr. ir. T.H.J.J. van der Hagen,
voorzitter van het College voor Promoties,
in het openbaar te verdedigen op maandag 8 januari 2018 om 12:30 uur

door

Yerong WU

Master of Science in Cartography and Geographical Information System,
Beijing Normal University, China
geboren te Xiangtan, Hunan, China.

Dit proefschrift is goedgekeurd door de

promotor: Prof. dr. M. Menenti
copromotor: Dr. M. de Graaf

Samenstelling promotiecommissie:

Rector Magnificus,	voorzitter
Prof. dr. M. Menenti,	Technische Universiteit Delft
Dr. M. de Graaf,	Technische Universiteit Delft & KNMI
Onafhankelijke leden:	
Prof. dr. M. Verstraete	University of the Witwatersrand, South Africa
Prof. dr. ir. H.W.J. Russchenberg	Technische Universiteit Delft
Prof. dr. A.P. Siebesma	Technische Universiteit Delft
Dr. J.P. Veefkind	Technische Universiteit Delft & KNMI
Dr. R.C. Levy	NASA Goddard Space Flight Center, USA

TU Delft Delft University of Technology

Keywords: Aerosol optical depth, aerosol type, aerosol vertical distribution, Bidirectional reflectance distribution function, Satellite observations, Radiative transfer model, Lookup table, Ill-posed problem

Printed by: Optima Grafische Communicatie, the Netherlands

Front & Back: Designed by Yerong Wu

ISBN 978-94-6361-052-0

An electronic version of this dissertation is available at
http://repository.tudelft.nl/.

To my parents

Contents

Summary

The Aerosol Optical Depth (AOD), a measure of the scattering and absorption of light by aerosols, has been extensively used for scientific research such as monitoring air quality near the surface due to fine particles aggregated, aerosol radiative forcing (cooling effect against the warming effect by carbon dioxide CO_2), aerosol long-term trend analysis and the climate change on regional and global scale.

Aerosols vary greatly over time and space. This is because of the short lifetime of aerosols (a few hours to a week), and also because of the heterogeneous distribution of sources and the variable effectiveness of atmospheric mixing though turbulence. To monitor aerosols, observations by space-borne instruments have a huge advantage (nearly global coverage daily) over ground-based measurements (point observation). Global quantitative aerosol information has been derived from satellite measurements for decades. The MODerate resolution Imaging Sepctroradiometer (MODIS) AOD product is proven to be mature and is extensively applied in different scientific fields. The current AOD product generated with the collection 6 (C6) Dark Target (C6_DT) algorithm over land is still suffering from errors or biases due to parameterization, assumptions, modeling, and retrieval techniques as well as ill-posed problems, presenting large uncertainties including regional bias, angular effects and a large number of unphysical negative values. Chapter 1 discusses the challenges and limitations in the current satellite aerosol retrieval algorithm.

Owing to the use of static aerosol properties (predefined aerosol models and fixed vertical profile over the globe), the MODIS algorithm may give serious errors since aerosols can change over time and are distributed very diversely at different altitude levels. To quantify these errors, in Chapter 3 the sensitivity of AOD retrieval to the variation of aerosol vertical profiles and types with the MODIS algorithm is evaluated by a set of experiments. It was found that the AOD retrieval shows a high sensitivity to different vertical profiles and types.

As suggested by the sensitivity study, it is necessary to investigate the impact of dynamical aerosol properties in a real case. To do this, an adaptive development of the MODIS C6_DT algorithm was implemented to consider realistic aerosol vertical profile in the retrieval (Chapter 4). MODIS and Cloud-Aerosol Lidar and Infrared Pathfinder Satellite Observation (CALIPSO) measurements were used. Inferred from CALIPSO data, the vertical profile was applied into the new algorithm to generate an accurate Top Of the Atmosphere (TOA) reflectance for the retrieval. The AOD retrieval was compared between C6_DT and the new algorithm with cases of heavy smoke and dust. The difference in the retrieval was significant between C6_DT and the new algorithm, which demonstrated that C6_DT would give large errors in the retrieval for these cases.

In the MODIS algorithm, the assumption of the surface with isotropic reflection (Lambertian) is inconsistent with the well-known fact that the surface has a strong anisotropic reflection (non-Lambertian), and could lead to large uncertainties in estimating the surface contribution to satellite measurements, with resulting errors in the AOD retrieval.

Chapter 5 describes a newly developed algorithm (BRF_DT) by considering non-Lambertian surface reflectance characterized by Bidirectional Distribution Reflectance Function (BRDF), where the surface reflection is described by four reflectance properties — bidirectional, directional-hemispherical, hemispherical-directional, and bihemispherical reflectance and coupled into the radiative transfer process to generate an accurate TOA reflectance. In addition, a parameterization of spectral relationship inherited from C6_DT was applied to constrain the surface BRF. The remaining three components are determined by MODIS BRDF/albedo product. As shown by sample plots and histograms as well as analysis and comparison against AERONET measurements, the AOD retrievals were significantly improved by BRF_DT especially for areas with heavy aerosol loading.

For the case of areas with light aerosol loading, the parameterization of spectral surface BRF should be further refined to yield a better retrieval. Chapter 6 shows that a new parameterization was derived for the BRF_DT algorithm (called BRF_DT2) by using 3 years of BRF data from AERONET-based Surface Reflectance Validation Network (ASRVN). The contribution to the TOA reflectance dominated by the surface BRF was well estimated. As a result, negative retrievals and angular biases were significantly reduced in BRF_DT2. A summary of the current and future research of satellite aerosol retrieval is introduced in Chapter 7.

Samenvatting

De Aerosol Optische Dikte (AOD), een grootheid die de hoeveelheid verstrooiing en absorptie van licht door aërosolen kwantificeert, is uitgebreid gebruikt in wetenschappelijke studies, zoals de monitoring van luchtkwaliteit nabij het aardoppervlak door fijnstof, de aërosol-stralingsforcering (verkoelend effect in tegenstelling tot het verwarmende effect door kooldioxide CO2), aërosol langetermijn-trendanalyse, en klimaatveranderingen op regionale en mondiale schaal.

Aërosolen variëren sterk in tijd en ruimte. Dit is het gevolg van de korte verblijftijd van aërosolen in de atmosfeer (van een paar uur tot een week), en ook door de heterogene verdeling van bronnen en de variabele effectiviteit van atmosferische turbulente mixing. Om aërosolen te monitoren, zijn waarnemingen door satellietinstrumenten zeer voordelig (bijna complete mondiale bedekking) ten opzichte van grondwaarnemingen (puntwaarnemingen). Mondiale kwantitatieve aërosolinformatie is afgeleid uit satellietwaarnemingen in de afgelopen decennia. MODerate Imaging resolution Spectroradiometer (MODIS) AOD heeft zich bewezen als een state-of-the-art product en is uitgebreid toegepast in het wetenschappelijke veld. Desondanks heeft het huidige AOD product, geproduceerd door het Collection 6 (C6) Dark Target (C6_DT) algoritme over land, te maken met veel fouten en afwijkingen door parametrisaties, aannames, modellering, simulaties, and retrievaltechnieken in het algoritme en door het wiskundige ondergedetermineerde probleem (meer onbekenden dan waarnemingen), resulterend in een relatieve lage nauwkeurigheid, inclusief regionale afwijkingen, hoekafhankelijkheden en een grote hoeveelheid niet-fysische negatieve waarden. Hoofdstuk 1 beschrijft de uitdagingen en de beperkingen in het huidige satellietretrieval-algoritme.

Door het gebruik van constante aërosoleigenschappen (voorgedefinieerde aërosolmodellen en constante verticale profielen rond de aarde), kan het MODIS algoritme serieuze fouten in de retrieval geven, omdat aërosolen in de tijd kunnen veranderen en ze zeer divers over verschillende hoogtelagen zijn verdeeld. Om deze fouten te kwantificeren, wordt in hoofdstuk 3 de gevoeligheid van de AOD retrieval als functie van de variatie van aërosol verticale profielen en aërosoltypes door het MODIS algoritme, in een aantal experimenten geëvalueerd. Dit bracht een grote gevoeligheid van de AOD retrieval voor verschillende profielen en typen aan het licht.

Als gesuggereerd door de gevoeligheidsstudie, is het nodig om de invloed van dynamische aërosolprofielen met echte data te onderzoeken. Hiervoor werd een aangepaste versie van het MODIS C6_DT algoritme gemaakt, om een realistisch aërosol verticaal profiel in de retrieval mogelijk te maken (hoofdstuk 4). MODIS en Cloud-Aerosol Lidar and Infrared Pathfinder Satellite Observation (CALIPSO) metingen werden gebruikt. Afgeleid uit CALIPSO-metingen, werd het verticale profiel gekoppeld aan het nieuwe algoritme, om een nauwkeurige reflectantie aan de top van de atmosfeer te genereren voor de retrieval. De AOD retrievals uit C6_DT en het nieuwe algoritme werden vergeleken voor gevallen met dikke rookpluimen en (woestijn)stof. Een significant verschil werd aangetoond tussen C6_DT en het nieuwe algoritme, wat demonstreert dat C6_DT grote

fouten geeft in deze gevallen.

In het MODIS algoritme wordt aangenomen dat het oppervlak een isotrope (Lambertiaanse) reflector is, wat inconsistent is met het bekende feit dat het oppervlak een sterke anisotrope (niet-Lambertiaanse) reflectantie heeft, wat kan leiden tot grote onzekerheden in de schatting van de oppervlaktebijdrage aan de satellietmetingen, met fouten in de retrieval tot gevolg. In hoofdstuk 5 wordt een nieuw ontwikkeld algoritme (BRF_DT) beschreven, dat gebruik maakt van niet-Lambertiaanse oppervlakte-eigenschappen, gekarakteriseerd door Bidirection Distribution Reflectance Function (BRDF), waarin de reflectantie van het oppervlak wordt beschreven door vier componenten - bi-directionele, directioneel-hemisferische, hemisferisch-directionele, en bi-hemisferische reflectantie en gekoppeld aan het stralingstransport-proces, om een nauwkeurige reflectantie aan de top van de atmosfeer te genereren. Tegelijkertijd wordt een parametrisatie van de spectrale relatie overgenomen van C6_DT om de oppervlakte BRF te beschrijven. De drie overgebleven componenten worden bepaald met het MODIS BRDF/albedo product. Zoals wordt getoond in zowel voorbeeldgrafieken en histogrammen als analyses en vergelijkingen met AERONET-metingen, worden de AOD retrievals aanzienlijk verbeterd door BRF_DT, met name in gebieden met hoge aërosolconcentraties.

1

Introduction

The eternal mystery of the world is its comprehensibility.

Albert Einstein

1

1.1. Importance of atmospheric aerosol

An atmospheric aerosol is a suspension of liquid or solid particles distributed in the air, with a radius ranging from a few nm to over 100 μm. Aerosols from natural sources, e.g., volcanic ash, sea spray, dust, and human activities e.g., industrial emission, forest fire smoke and fossil fuel burning affect human health, cloud formation, precipitation, and climate change (GCOS, 2007; IPCC, 2013) (see Figure 1.1). Near land surfaces, high

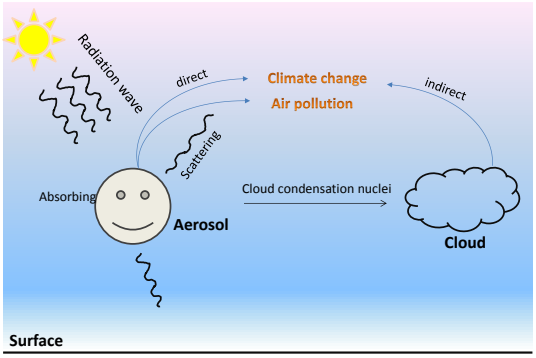

Figure 1.1: Schematic of aerosol effects on air quality and climate. Aerosols have an important impact on climate by their direct and indirect effects. Most aerosols (except black carbon) can directly absorb and scatter solar radiation, cooling the atmosphere globally (direct effects). On the other hand, aerosols can play a role as cloud condensation nuclei (CCN) through their hygroscopic properties, affecting cloud formation and albedo (indirect effects). In addition, aerosols aggregated and lifted in the boundary layer of the atmosphere can lead to air pollution. For example, these aerosols significantly reduce the visibility. Collocated with viruses, they can be inhaled by human causing human disease (e.g., lung disease and flu).

concentrations of aerosols can lead to poor air quality. In general, all aerosols are inhaled by humans, but small aerosols penetrate the lungs deeper, causing more damage, such as fine aerosols with aerodynamic diameter < 2.5 μm combined with various micro-organisms (Laden et al., 2000; Samet et al., 2000; Pope III et al., 2002; Pope III and Dockery, 2006). In addition, these aerosols can substantially reduce visibility because they scatter and absorb solar radiation. Recently, many events of severe air pollution in Beijing, China occurred (see Figure 1.2) because much of the aerosol load comes from vast arid zones to the east of the city. The rapid industrialization of the country especially the region around the capital has made this problem even worse, in terms of aerosol density, event frequency, as well as health impact.

Aerosols also have a significant impact on climate due to their direct and indirect effects (Kaufman et al., 2002; Myhre, 2009; IPCC, 2013). Most aerosols affect the climate directly by cooling the atmosphere globally through reflecting solar radiation into outer space, whereas absorbing aerosols e.g., black carbon, locally warm the atmosphere and cool the surface; this is also called the direct effect of aerosol. The net effect of aerosols is cooling, as compared to greenhouse gases CO_2 which lead to warming. As for indirect effects on climate, aerosols can play a role as cloud condensation nuclei through their hygroscopic properties, and influence the formation and albedo of clouds and further influence the precipitation locally and globally.

Aerosols are distributed unevenly in the atmosphere, showing a strong variability in

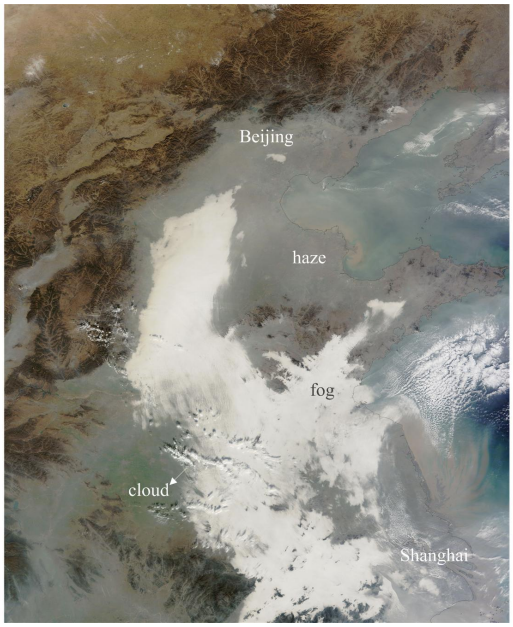

Figure 1.2: Haze in Eastern China, observed by MODIS/Terra on Dec 7th, 2013. The brightest areas indicates cloud or fog. Haze is given as gray color. Figure courtesy of NASA MODIS rapid response team.

space and time. Aerosols can move with the wind, sink by their gravity and be removed by the weather e.g., precipitation and cloud formation, on a regional scale, to yield a rapid change or fluctuation in their concentration and chemical composition.

Many studies have been done to obtain aerosol properties with ground-based and space-borne instruments. Observing the earth from space, satellites have the unique advantage of large or even global coverage. Therefore, they have been extensively used to retrieve aerosol properties, such as the single viewing satellite sensor MODerate Resolution Imaging SpectroRadiometer (MODIS) (Remer et al., 2005; Levy et al., 2007b, 2013b; Hsu et al., 2004, 2006, 2013; Sayer et al., 2013, 2015, 2016), the Advanced Very High Resolution Radiometer (AVHRR) (Stowe et al., 1997; Mishchenko et al., 1999), multi-angle viewing sensor Advanced Along-Track Scanning Radiometer (AATSR) (North, 2002; North et al., 1999; Grey et al., 2006; Thomas et al., 2009), Multi-angle Imaging SpectroRadiometer (MISR) (Martonchik et al., 1998, 2002, 2009; Keller et al., 2007), PoLarization and directionality of the Earth's Reflectances (POLDER) (Tanré et al., 2011; Herman et al., 2005; Dubovik et al., 2011), and active detection sensors Cloud-Aerosol Lidar and Infrared Pathfinder Satellite Observation (CALIPSO) (Liu et al., 2008b,a).

One aerosol property, Aerosol Optical Depth (AOD), describes the radiation attenuation in the atmosphere and has gained a lot of attentions from the scientific community. This is because AOD can be applied to characterize aerosol concentrations and evaluate the impact of aerosols on climate. AOD is used to indicate the aerosol amount or particulate matter concentration (aerodynamic diameter $< 2.5\ \mu$m, PM2.5) near the surface (e.g., Chu et al., 2003; Engel-Cox et al., 2004; Nicolantonio. et al., 2007; Hoff and Christo-

pher, 2009; Wu et al., 2012). It is also used to estimate the aerosol direct radiation forcing (e.g., Yu et al., 2006; Bellouin et al., 2008; Myhre, 2009), as well as for long-term trend analysis of aerosol (e.g, Li et al., 2009; Zhang and Reid, 2010; Guo et al., 2011) and data assimilation studies (Zhang and Reid, 2010; Hyer et al., 2011; Liu et al., 2011; Schwartz et al., 2014).

1.2. The MODIS AOD product

To retrieve AOD, the MODIS Dark Target (DT) AOD algorithm has been proven to be mature. The algorithm has experienced several generations of developments (Remer et al., 2005; Levy et al., 2007b,a, 2013b) and extensive and rigorous validations against the ground "truth" data collected by AErosol Robotic NETwork (AERONET) (e.g., Levy et al., 2005, 2010; Tao et al., 2015; Wu et al., 2017b). Because of this and its high spatial (10 km × 10 km at near-nadir) and temporal resolution (nearly daily coverage over the globe), the MODIS AOD product has become one of the most popular aerosol products and been widely applied in different scientific fields.

The accuracy of the DT algorithm critically depends on the presence of a dark target in each scene. This is not a problem over the ocean, which is mostly very dark outside of the sun glint. However, a lack of really dark targets could be a major source of errors over land. Problems areas include arid zones, desert and urban regions. Currently, the MODIS Collection 6 DT (C6_DT) AOD product over ocean has a relatively high accuracy with Expected Error (EE, one standard deviation in Gaussian function) of +(0.04 + 10%), -(0.02 + 10%) (Levy et al., 2013b). However, the accuracy of the MODIS AOD over land is still low, with EE of ±(0.05 + 15%) (Levy et al., 2013b). Three well-known causes of the low accuracy are listed below:

1. For each retrieval, the performance of the MODIS C6_DT algorithm is highly dependent on the number of the MODIS measurements (Levy et al., 2013b; Wu et al., 2017b). These measurements are chosen by the dark target selection (Levy et al., 2007b) and averaged over the box of 20 × 20 pixels (500 m resolution) in an image in the retrieval. A high number of measurements (e.g., ≥ 50) can lead to a high quality AOD with C6_DT algorithm, while fewer measurements e.g., ≤ 20, lead to a lower quality AOD. In fact, the MODIS science team recommends to use the AOD product with the best quality only, which would result in a huge reduction (about 50%) in AOD retrievals (Wu et al., 2017b).

2. The MODIS C6_DT algorithm presents a regional bias in the AOD retrieval. The overestimation (about 15% in average) of the retrieval has been found in Eastern China (Tao et al., 2015; Wu et al., 2017b), and in North America (Wu et al., 2017b). Eck et al. (2013) and Wu et al. (2017a), showed that there was a significant bias over biomass-burning areas in South Africa.

3. The MODIS C6_DT algorithm gives a strong angular dependence of the retrieval (Wu et al., 2017b, 2016a). In the algorithm, the retrievals are much better at a small scattering angle (the angle between the direction of the solar incident flux and the direction of the reflected flux into the view of the sensor) than at a large scattering angle. More details about this are discussed in section 5.4.2 and 6.4.2.

The current uncertainty level of AOD retrievals over land leads to a large uncertainty (±0.03 or 15 ~ 20%) in the global mean AOD (Levy et al., 2013b) that can not well meet the need of the precision ($\delta\tau$: 0.01 ~ 0.02) in the estimate of direct aerosol forcing (e.g., McComiskey et al., 2008). For the estimation of PM2.5 concentration near the surface, it can lead to even large errors (> 20%) along with other meteorology factors (e.g., Hoff and Christopher, 2009). To be specific, the regional biases and angular dependence challenge the estimate of the surface-level PM2.5 concentration using MODIS AOD data. This mainly leads the relationship between AOD and PM2.5 concentration to vary across different regions, i.e., difficult to apply in other regions, though the estimate also depends on other conditions such as the aerosol vertical profile, humidity and aerosol chemical composition as well as wind velocity and direction. (e.g., Engel-Cox et al., 2004; Gupta et al., 2006; Koelemeijer et al., 2006; Hutchison et al., 2008; Liu et al., 2007; Wu et al., 2012). Although the method that uses multi-source satellite AOD products calibrated with AERONET data can significantly improve the accuracy in predicting surface PM2.5 concentration(van Donkelaar et al., 2016), it may not perform well where there is few AERONET sites/data since the AOD data were not well calibrated. For assimilation studies, the systematic bias of MODIS AOD data (e.g., regional bias) can degrade analyses and forecasts, such as resulting in a large number of outliers(e.g., Zhang and Reid, 2006; Zhang et al., 2008). Although empirical corrections proposed by Zhang and Reid (2006) were used to reduce the bias and benefited data assimilation (Zhang and Reid, 2006; Zhang et al., 2008; Shi et al., 2011; Saide et al., 2013), they may also introduce some unknown artificial errors into the assimilated data. Recently, the importance of aerosols and their climate impacts on regional scale (mainly over land) has been highlighted by aerosol trend analysis Chin et al. (2014), which means the analysis can be seriously affected by the regional bias in AOD, if used this data. In summary, all the applications have strongly demonstrated the urgent needs for reducing the uncertainties, biases, angular dependence in the MODIS AOD retrievals.

1.3. Potential source of errors in the AOD retrieval

The low accuracy of the AOD retrieval is caused by many potential error sources, such as cloud mask, instrument calibration, surface effects and aerosol properties (Li et al., 2009; Kokhanovsky et al., 2010). The instrument calibration is dependent on the sensor quality, e.g., signal to noise ratio, and calibration method applied. i.e whether on-board or vicarious, which directly determines the quality of the satellite measurements and affects the retrieval accuracy. This issue is more related to the measurement, and should be better left to the instrument team. Presently, the cloud mask method is well developed (Ackerman et al., 1998, 2010; Martins et al., 2002), which removes the pixels of clouds or contaminated by a cloud i.e cloud brightening effect. Additionally, thin-cirrus can be accurately detected and removed in the MODIS C6 algorithm (Levy et al., 2013b).

However, in the AOD retrieval algorithm, it is still a challenging task to deal with the issue of the surface effects and aerosol properties. Many attempts have been made towards resolving this for decades, but there are many limitations, which are shown below.

Aerosol properties

In the AOD retrieval, it is necessary to understand the aerosol optical properties, such as the single scattering albedo and phase function. This is because these properties determine the efficiency of aerosol scattering and absorption and directly affect the algorithm accuracy. For the MODIS AOD product, the first mature version Collection 4 (C4) was described in Remer et al. (2005), where three non-dust or fine models (Kaufman et al., 1997; Remer and Kaufman, 1998; Remer et al., 1998) and one dust model were characterized. With the single-view measurement by MODIS, it is not possible to retrieve the non-dust model simultaneous with AOD and surface reflectance in the algorithm. Thus, it was assumed that the non-dust model could be selected and applied according to seasons and geography.

Later, to pursue more reliable AOD retrievals, these aerosol models were further refined in the second-generation retrieval algorithm collection 5 (C5), by performing cluster analysis (Omar et al., 2005) for the aerosol climatology of almucantar retrievals (Levy et al., 2007b,a). In C5, the spheroid shape of the dust particles was applied instead of the sphere shape, which is consistent with the recent studies in Dubovik et al. (2002b, 2006). Nevertheless, the assumption about the non-dust model choice in C4 still remained in C5, and even in the latest version C6_DT (Levy et al., 2013b). This assumption could cause problems when some unusual aerosol source arises since the fine aerosol model is predefined in the AOD retrieval. As an example, in this thesis it is shown that smoke by a forest fire that appears in North America (Canada) (Lee et al., 2015) and in South Africa (Eck et al., 2013) would be wrongly assumed by the algorithm. As a result, serious errors could be introduced in the retrieval. The retrieval would be better if it included a realistic aerosol model.

Another aerosol property, i.e. its vertical profile, should be well defined. Many studies have assumed that most aerosols are statically located in the atmosphere boundary layer (below 3 - 4 km, near the surface) (e.g., Hsu et al., 2004; Levy et al., 2007b; Thomas et al., 2009). This is true for most cases where aerosols are lifted from the ground. However, in many cases aerosols can reach much higher elevations due to either convection or high altitude source injection (volcanoes or pyrocumulus), such as the dust layers that can reach high altitude (3 to 6 km) in North Africa and Arabian Peninsula (e.g., Liu et al., 2008a), and the smoke plumes that can rise up to 6 to 9 km by wildfire over North America (e.g., Lee et al., 2015). Additionally, the negative bias of the retrievals presented in the heavy dust region (Levy et al., 2010; Sayer et al., 2013) is probably due to neglecting the elevated dust layer. Therefore, a more comprehensive study has been carried out to include a dynamic distribution of the aerosol layer.

Estimation of surface effects

To retrieve the AOD over land, it is necessary to accurately estimate the surface reflected radiance and distinguish it from the aerosol signal. This is because under low to moderate atmospheric opacity, terrestrial surfaces can contribute significantly to the planetary radiance at the Top Of Atmosphere (TOA), due to their high reflectance compared to that atmospheric constituents. It is not an easy task to achieve this, since the contribution from a bright surface to the TOA radiance can be higher than the one from the atmosphere, which makes it difficult to separate the aerosol contribution from the TOA

radiance (Hsu et al., 2013). In addition, the complicated anisotropic reflection at the land surface itself makes this task more challenging.

A simple approach has been developed that takes advantage of dark or darker surfaces at different bands to obtain a relatively accurate estimation of the atmosphere contribution to the radiance at TOA, by two versions of the algorithms MODIS DT and Deep Blue. The MODIS DT land AOD algorithm makes use of the presence of a dark surface at two visible channels 0.47 μm and 0.66 μm and the approximate transparency of the atmosphere at a relatively long wavelength 2.12 μm, to estimate the effects of atmospheric scattering and surface reflection on the TOA reflectance (Remer et al., 2005; Levy et al., 2007a,b, 2013b). The MODIS Deep Blue AOD algorithm is similar, but uses the characteristics of a darker surface at blue channels 0.412 μm and 0.470 μm and little absorption by dust at a red channel (e.g., 0.670 μm) (Hsu et al., 2004, 2006).

By taking account of the surface anisotropic reflection, the algorithms can yield a relatively good retrieval of AOD (Lyapustin et al., 2011a,b; Yang et al., 2014). Nevertheless, some shortages or problems should be pointed out. The algorithm in Lyapustin et al. (2011a,b) is critically computationally complex and time-consuming because it needs to process a large amount of accumulated satellite data over multiple days. As for the algorithm developed by Yang et al. (2014), there are mistakes in the calculation of the transmitted radiance and the surface contribution. To balance the complexity or computational efficiency and the accuracy, a simple and reliable framework is needed for the retrieval, with respect to the effects of surface anisotropic reflection in the retrieval (see Chapter 5).

Algorithm intrinsic errors

The algorithm intrinsic errors are the errors that occur in the retrieval with a "perfect" measurement. These errors are usually related to the approach applied in the algorithm. In the retrieval procedure, two major approaches have been developed: LookUp Table (LUT) and radiative transfer modeling. Through pre-calculation, the LUT approach has been adopted by most authors in the retrieval since this approach is fast and can well balance computational cost and accuracy, whereas radiative transfer modeling has not been widely applied due to its highly computational cost.

Nevertheless, using the LUT approach, some intrinsic errors could happen (Levy et al., 2007b; Kokhanovsky et al., 2010). However, few authors have investigated these errors in detail. In this thesis, it is shown that these errors are mainly attributed to the underlying assumptions and the optimization techniques applied in the retrieval. A better AOD could be retrieved if the intrinsic errors are well understood and evaluated.

Summary

As we discussed above, the potential source errors in the algorithm mainly lie in the inappropriate assumptions of the aerosol model and static aerosol vertical distribution over the globe, and the underestimation/overestimation of the surface contribution to the TOA radiance, not considering the surface anisotropic reflection. In addition, algorithm intrinsic errors are also a major source of uncertainty in the retrieval.

1.3.1. Scope and objectives

Given the limitations and potential source errors in recent studies as aforementioned, the main research question in this thesis now can be formulated as:

How to improve the Aerosol Optical Depth retrieval over land with MODIS measurements?

To this end, a new algorithm should be developed by accurately characterizing aerosol and surface properties such as a realistic aerosol model, dynamic vertical profile and surface anisotropic reflection. To achieve the goal, the main problem is subsequently divided into four specific questions:

1. What are the main weaknesses in the current MODIS C6_DT AOD retrieval algorithm?
2. How sensitive is the AOD retrieval over land to aerosol vertical profiles and types using the MODIS algorithm?
3. How to couple the surface anisotropic reflection into radiative transfer modeling to yield a better retrieval?
4. How to account for the angular effects and improve the AOD retrieval?

1.4. Outline

This dissertation is organized in seven chapters to answer the above questions:

Chapter 2 presents the basic theory of the satellite AOD retrieval. The simulation of TOA radiance is introduced with the related aerosol properties and the surface reflection. In addition, a brief review of the MODIS AOD algorithm is given here (**related to Question 1**).

Chapter 3 investigates the sensitivity of aerosol optical depth retrieval with the MODIS algorithm to aerosol vertical distributions and types (**related to Question 2**). The algorithm is completely recoded in another programming language that allows to manipulate it and do experiments. Four experiments were performed, using different aerosol properties including 3 possible non-dust aerosol models and 14 vertical distributions. The algorithm intrinsic uncertainty was investigated as well as the interplay effect of aerosol vertical profile and type on the retrieval.

Chapter 4 applies the knowledge from the previous study (chapter 3) to a real case, giving evaluations on the impact of aerosol vertical distribution on the retrieval using CALIPSO and MODIS data (**related to Question 2**). An adaptive development of the MODIS C6_DT algorithm was implemented to consider realistic vertical profiles in the retrieval. This new algorithm makes use of aerosol vertical profile extracted from CALIPSO measurements to generate an accurate TOA reflectance for the retrieval, where the profile is assumed to be a single and homogeneous layer horizontal, represented as a Gaussian function with a single variable of the mean height in the vertical. The AOD retrieval with C6_DT and with our new algorithm for cases of heavy dust and smoke was compared.

Chapter 5 focuses on improving the aerosol optical depth retrieval by considering the anisotropic reflection of the surface. A new algorithm called BRF Dark Target was developed in which the framework of the radiative transfer theory with a Lambertian surface

was changed into the one with a non-Lambertian surface (**related to Question 3**). The surface Bidirectional Reflectance Distribution Function (BRDF) is adopted to determine: bidirectional, directional-hemispherical, hemispherical-directional and bihemispherical reflectance, and included into the radiative transfer equation to generate an accurate TOA reflectance. The results are compared to C6_DT and validated with AERONET data.

Chapter 6 reduces the angular bias of the retrieval by the dark target algorithm by refining the parameterization of the spectral surface Bidirectional Reflectance Factor (BRF) at visible and shortwave infrared wavelengths (**related to Question 4**). For areas with low aerosol loading, the contribution of the surface BRF to the TOA reflectance becomes dominant and should be estimated more precisely. We update the parameterization of surface reflectance using 3 years of data acquired by the AERONET-based surface reflectance validation network (ASRVN). In addition, the Normalized Distribution Vegetation Index (NDVI) was removed from the parameterization due to its angular dependence. The results were compared with the ones in Chapter 5 and the ones in C6_DT.

Chapter 7 presents a summary of the main results and contributions of the satellite AOD retrieval over land. Suggestions and recommendations are given for future research such as the development of a higher spatial resolution (3 km ×3 km) product and the extension to a broader spectrum of land surface conditions, including a bright surface (desert).

2

Aerosol retrieval from satellite measurements: algorithm basics

2.1. Introduction

In the previous chapter, we discussed the potential source of errors in the current MODIS algorithm, which motivated the goal of this investigation as a whole: how to improve the MODIS AOD retrieval over land.

As a first step towards this, the chapter gives insight into the AOD retrieval algorithm, including the parameters required for Radiative Transfer (RT) modeling and retrieval techniques. Section 2.2 introduces the aerosol properties including AOD, the size distribution, single scattering albedo and scattering phase function. Several typical aerosol types were considered in this evaluation. Section 2.3 illustrates the analytical RT equation for the simulation of Top Of Atmosphere (TOA) reflectance. A LookUp Table (LUT) approach is introduced in section 2.4. Section 2.5 presents two major models of the surface reflection (isotropic and anisotropic reflection) used in the aerosol retrieval algorithm. Section 2.6 presents a method to account for single scattering by an aerosol mixture (nondust mixed with dust aerosols). Aerosol measurements are briefly introduced in section 2.7, including MODIS and CALPSO data, as well as ground based AERONET data. Finally, a brief review of the operational MODIS algorithm is given in section 2.8, including the assumptions and "a priori" surface and aerosol properties and how to deal with the ill-posed problem (more unknowns than measurements), as well as the retrieval approach (LookUp Table). A conclusion is drawn in section 2.9.

2.2. Aerosol properties

Solar radiation is scattered and absorbed by atmospheric aerosols. To describe the attenuation (scattering and absorption) of incident light by aerosols, the aerosol optical depth (AOD, τ) is introduced, which is the integral of the aerosol extinction coefficient β_{ext} over the altitude z in the atmosphere, given as:

$$\tau(z) = \int_0^z \beta_{ext}(z')\mathrm{d}z' \tag{2.1}$$

Assuming a direct radiance I_0 traversing an aerosol layer straightly (i.e. ignoring the scattering), the attenuation of the radiance is expressed as (e.g., Van de Hulst, 1957; Liou, 2002):

$$I = I_0 \exp(-\tau/\mu) \tag{2.2}$$

This equation is the so-called Beer-Bouguer-Lambert law, which illustrates the exponential attenuation of the direct radiance I_0. Note that μ in equation 2.2 is the cosine value of the zenith angle θ of I_0. A complete description of the radiation transfer process is introduced in section 2.3.

For the attenuation, aerosol size is the determining parameter. This is because the size of aerosol particles is comparable to the wavelength of the light which is well explained by Lorenz-Mie theory (e.g., Mie, 1908). The extinction of the radiation is dependent on the size distribution, shape (e.g., sphere or non-sphere) and chemical composition (related to complex refractive index $(m + ki)$) of the aerosols.

Figure 2.1 shows that the scattering patterns are significantly different with different size particles. The small spherical aerosol (e.g., 10^{-4} μm relative to the wavelength of the

incident light) tends to equally scatter the radiation in the forward and backward directions. When the aerosol becomes larger, the scattered radiation becomes increasingly larger in the forward direction. The aerosols that have different chemical compositions

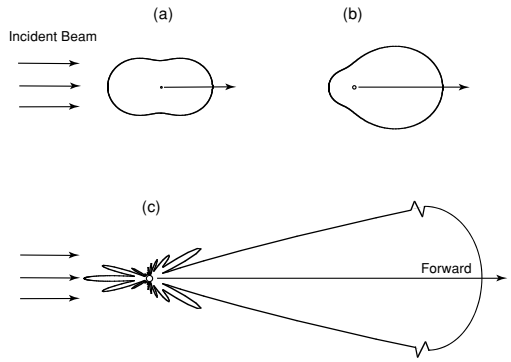

Figure 2.1: The visible light of 0.5 μm scattered by 3 different aerosol particles. Spherical shape is assumed for the particles with the size: (a) 10^{-4} μm, (b) 0.1 μm, and (c) 1 μm. Figure is from Liou's book (Figure 1.4 in page 7 in Liou (2002)).

behave differently in the transmission and absorption of the radiation with wavelength.

Let the absorbing and scattering efficiencies of a particular aerosol type be defined as $Q_{abs} = \sigma_{abs}/(\pi r^2)$ and $Q_{sca} = \sigma_{sca}/(\pi r^2)$ [dimensionless], respectively. The cross section σ_{abs} and σ_{sca} in units of area [cm^2] represent the interaction of the beam with the geometrical area of a particle. In the simple case where there is only a single aerosol type, the net effect of the absorbing and scattering properties can be parameterized in term of the ratio of its cross sections $\sigma_{abs}/\sigma_{sca}$, or of the ratio of its efficiencies Q_{abs}/Q_{sca}. The extinction cross sections σ_{ext} or efficiency Q_{ext} is the sum of absorbing and scattering cross sections or efficiencies, respectively, e.g., $\sigma_{ext} = \sigma_{abs} + \sigma_{sca}$ or $Q_{ext} = Q_{abs} + Q_{sca}$. The single scattering albedo (SSA, ω_0) is the ratio $\sigma_{sca}/\sigma_{ext}$. Weak or strong absorbing aerosols are defined by their SSA. Most aerosols are scattering and weakly-absorbing particles except for the black carbon aerosols which are strongly absorbing. Given as the value of the complex refractive index, σ_{sca} and σ_{abs} is obtained using Mie formulae. A numerical calculation of Mie formulae (MIEV code) has been implemented by Wiscombe (1980), which shows accurate reproduction of spherical aerosol optical properties. The corresponding scattering phase function p is also determined to describe the angular pattern of the radiation scattering by the aerosol, which is given as (e.g., Liou, 2002):

$$p = \frac{2\pi}{k^2 \sigma_{sca}} (i_1 + i_2) \tag{2.3}$$

Where i_1 and i_2 are the intensity functions which are functions of the particle radius r, the index of refraction m, the incident wavelength λ, and the scattering angle Θ, and $k = 2\pi/\lambda$.

For a group of aerosols, the absorbing and scattering quantities are described as absorbing β_{abs} and scattering *coefficients* β_{sca} in units of inverse length [cm^{-1}], which are

obtained by integrating the absorbing/scattering cross sections or efficiencies over the size distribution $N(r)$ in unit of $[\mathrm{cm}^{-3}\mu\mathrm{m}^{-1}]$ of the group aerosols, e.g,

$$\begin{aligned} \beta_{abs} &= \int \sigma_{abs} N(r) \mathrm{d}r \\ \beta_{sca} &= \int \sigma_{sca} N(r) \mathrm{d}r \end{aligned} \tag{2.4}$$

The size distribution $N(r)$ is defined in Appendix A. Similarly, the phase function P for the group of aerosols is calculated as:

$$P = \frac{2\pi}{k^2 \beta_{sca}} \int [i_1(r) + i_2(r)] N(r) \mathrm{d}r \tag{2.5}$$

The size distribution $N(r)$ can be represented by different functions such as power-law, gamma and log-normal function (e.g., Liang, 2003). One of the distributions, log-normal size distribution has been widely applied in a number of satellite aerosol algorithm and *in-situ* AERONET site (e.g., Martonchik et al., 1998; Dubovik et al., 2002a; Remer et al., 2006; Levy et al., 2007b,a), since the assumption of lognormality allows accurate calculation of optical properties for most aerosols (Levy et al., 2007a).

2.2.1. Aerosol type

There are three major sources of aerosols in the atmosphere (Kokhanovsky, 2008). Aerosols can be generated from the oceanic surface due to wave breaking, i.e., sea salt. Aerosols can originate from the land surface e.g., desert dust, forest fire, volcanic ash and industrial emissions. Some aerosols can be generated by gas-to-particle conversion through chemical reactions between gaseous constituents, and/or by aggregation. Aerosols produced from the land surface can be classified into different types based on their source region and chemical composition. Three main aerosols from the land surface are discussed below.

Atmospheric dust mainly originates from dry regions by the wind. Specifically, the mobilization of dust over erodible terrain depends on the cube of the wind speed at the surface and is dispersed in the boundary layer by the wind shear. Dry regions are North Africa (e.g., Sahara desert and Libian deserts), the Middle East (Saudi Arabian lowlands) and North West China (e.g., Takla Makan and Gobi deserts). They all fall roughly in broad latitude belts corresponding to the sinking branches of the Hadley cell of the general circulation of the atmosphere, and in both hemisphere, well known as “global dust belt” (e.g., Prospero et al., 2002; de Graaf, 2006; Liu et al., 2008a). Dust particles are sometimes lifted to high altitude (> 3 km) and can be transported far away from the source region, presenting a large horizontal and vertical coverage. By design, Mie theory only applies to spherical particles, and that the shape of dust particles is generally far from spherical, hence requiring more complex models. Fortunately, by assuming that coarse aerosols are randomly oriented spheroids, Dubovik et al. (2006) have successfully modeled the dust optical properties (e.g., ω_0 and P) by creating a bridge between T-matrix method in Mishchenko and Travis (1994) and geometric-optics-integral equation method in Yang and Liou (1996).

Smoke originates from the combustion of biomass such as forest and grass. Biomass-burning can occur in the areas with abundant vegetation under both wet and dry conditions, e.g., wet areas: Indonesia, Amazon basin and Siberia; dry areas: Southern Africa, Brazil, Canada and Australia. Southern Africa has been found to be the world's largest biomass-burning source (e.g., Crutzen and Andreae, 1990; Giglio et al., 2006; van der Werf et al., 2010; Eck et al., 2013). Small particles (radii: $0.1 - 1\ \mu$m) are produced in the process of biomass combustion (e.g., Kokhanovsky, 2008). Smoke has an important effect on global climate. This is because the high hygroscopicity of smoke particles makes them very efficient cloud condensation nuclei (CCN), affecting cloud albedo and precipitation (e.g., de Graaf, 2006). Smoke particles can also absorb solar radiation due to the generally strong light absorption (e.g., black carbon).

Urban industrial particles are produced by urban and industrial emissions, e.g., emissions from power plants, industries and mobile sources. The source of emissions has changed with time due to human activities. In earlier studies, urban industrial aerosols are mainly located in developed countries such as the eastern US and western Europe (e.g., Remer et al., 2005). Later, Levy et al. (2007a) have demonstrated that there are more urban industrial aerosol present in most Asia regions. Recently, China (eastern part) has been suffering more and more serious air pollution (see Figure 1.2) due to urban and industrial emissions that are due to the rapid economic development (e.g., Wu et al., 2012; Guo et al., 2016b,a). These particles can have a significant impact on human daily life. Since most aerosols are emitted at or near the surface, and since they often remain confined in the lower atmospheric layers due to gravitational settling, they tend to affect visibility and air quality etc. For instance, the aggregated aerosol near the surface affects the traffic (e.g., an airplane takes on and off). In addition, the inhalation of polluted air and in particular fine aerosol particles collocated with viruses by humans and animals can cause severe ailments (e.g., lung disease and flu). Most of urban industrial aerosols have been found to have weakly-absorbing properties (e.g., Remer and Kaufman, 1998; Dubovik et al., 2002a; Remer et al., 2005; Levy et al., 2007a, 2013b). The thick layers of urban and industrial aerosols can largely scatter the solar radiation into outer space and significantly reduce the atmospheric temperature.

2.3. Radiative Transfer in the atmosphere

The radiation transmitted in the atmosphere is a complicated process that requires us considering not only the attenuation of the direct radiation (the same as Beer-Bouguer-Lambert law in equation 2.2), but also the scattering of radiation. In the solar spectral range, the total change of the radiance in a layer of a plane parallel atmosphere can be described as (e.g., Kuznetsov et al., 2012; Liou, 2002):

$$\mu \frac{\mathrm{d}I(\tau,\mu_s,\mu,\phi)}{\mathrm{d}\tau} = -I(\tau,\mu_s,\mu,\phi) + \frac{\omega_0(\tau)}{4\pi}\int_0^{2\pi}\mathrm{d}\phi'\int_{-1}^{1}P(\tau,\Theta)I(\tau,\mu_s,\mu',\phi')\mathrm{d}\mu' + \frac{\omega_0(\tau)}{4\pi}F_0P(\tau,\Theta)e^{-\tau/\mu_s} \tag{2.6}$$

This equation is known as the radiative transfer equation, where P is scattering phase function. On the right hand side, the first term I indicates the attenuation of radiance in

the direction of the transfer, the second term describes the scattering of radiation coming into the medium along the direction of the transfer (or multiple scattering), and the third term represents the single scattered solar radiation. The summary of the second and third term is the so called source function, indicating the scattering of the radiation.

In equation 2.6, the directions of solar incident radiation and diffuse radiation are described by the corresponding zenith angles (θ_s and θ) and the relative azimuth angle ϕ. μ_s, μ are the cosine value of the corresponding zenith angles, i.e. $\mu_s = \cos(\theta_s)$ and $\mu = \cos(\theta)$. Θ is the scattering angle, which is equivalent to $\Theta = \cos^{-1}(-\cos\theta_s\cos\theta + \sin\theta_s\sin\theta\cos\phi)$. F_0 is the parallel solar beam.

If the optical properties of the medium and their boundary conditions are known, then we can solve the radiative transfer equation with approximations and numerical methods.

2.3.1. Radiative Transfer code

The analytical RT equation has been implemented by a series of numerical methods. Four frequently used RT codes were introduced and discussed in (Kotchenova et al., 2008). These codes are MODTRAN (moderate resolution atmospheric transmittance and radiance code) (Berk et al., 1999; Acharya et al., 1999), RT3 (radiative transfer) (Evans and Stephens, 1991), 6SV1.1 (second simulation of a satellite signal in the solar spectrum, vector, version 1.1) (Kotchenova and Vermote, 2007) and SHARM (spherical harmonics) (Lyapustin, 2005). Initially developed from the LOW resolution TRANsmittance 7 (LOWTRAN7) model, MODTRAN (version 4) can model the absorption and scattering in the atmosphere with high spectral resolution up to 1 cm^{-1} and is preferable for the simulation or atmospheric correction of narrow band and hyperspectral radiometric data. SHARM is applied for Multi-Angle Implementation of Atmospheric Correction (MAIAC) with MODIS data (Lyapustin et al., 2011a,b, 2012). Similar to SHARM, 6S with has been used for the MODIS atmospheric correction (Vermote et al., 1997).

Due to the inaccurate parameterization of the phase function (Henyey-Greenstein function) and neglecting polarization, MODTRAN may lose some accuracy in the simulation of TOA radiance (Kotchenova et al., 2008). The Henyey-Greenstein (HG) function is a simplified expression of the aerosol phase function which is represented with asymmetry factor g of aerosol particles, defined as (Henyey and Greenstein, 1941):

$$P_{\mathrm{HG}}(\cos\Theta) = (1-g^2)/(1+g^2-2g\cos\Theta)^{3/2} \tag{2.7}$$

HG function can flatten the peak scattering in the forward direction. For instance, dust usually has a peak forward scattering due to their large particle size (effective radius = 0.68). Using HG function can obscure the forward scattering of dust and cause some errors in the RT process, resulting in uncertainties in the aerosol retrieval. Without considering the polarization effect, it can give a significant error in the retrieval (Levy et al., 2004). This problem can occur in SHARM since it does not take into account the effect of the polarization. With a high customization in atmospheric properties (atmospheric profile and aerosol optical properties) and accurate simulation, RT3 is used for the operational MODIS aerosol retrieval over land algorithm (Levy et al., 2007b, 2010, 2013b). It is preferable to use RT3 code in our study since it can reduce the inconsistency between the algorithms by us and the MODIS team.

2.4. Simulation with a Look-Up Table approach

Confronted with a large amount of satellite data, the method of direct RT calculation has not been widely applied in aerosol retrieval algorithm due to its extreme computational cost. The function relating TOA spectral radiance to e.g. AOD can be constructed in tabular from, i.e a Look Up Table (LUT), that can be applied to retrieve aerosol properties, e.g., as implemented in the MODIS algorithm. The LUT approach is fast and has been implemented in a number of retrieval algorithms with different space-borne sensors (e.g., Martonchik et al., 1998; Hsu et al., 2004; Remer et al., 2005; Levy et al., 2007b; Thomas et al., 2009). The LUT describes the radiation-field in the upper and lower atmosphere within the sun-surface-sensor system, including the radiance reflected by the atmosphere, the downward (upward) transmitted radiance at the atmospheric bottom and top, respectively, and the atmospheric backscattering ratio. The LUT accounts for these processes by using effective atmospheric spectral reflectance and transmittance obtained by re-sampling a large number of cases calculated with a RT code without knowing the reflectance at the underlying surface. After the calculation, they are stored in the LUT, indexed as illumination and viewing geometries (see Figure 2.2), wavelengths and aerosol properties. If the surface reflection is known, then we can simulate the TOA radiance by coupling with surface reflectance using LUT approach.

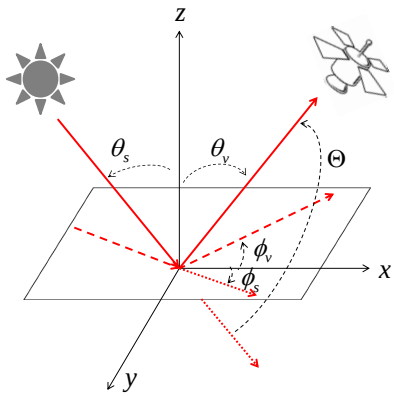

Figure 2.2: Schematic of illumination and viewing geometry on the surface target. The red solid lines (black dash curves) indicate the directions of the incident and reflected radiation, which are described as solar zenith angle θ_s and viewing zenith angle θ_v (measured from zenith direction z), and solar azimuth angle ϕ_s and viewing azimuth angle ϕ_v (measured from horizontal direction x). The dotted red lines represent the extension of the direction of the incident radiation. The scattering angle Θ is given as the angle between the direction of the incident radiation and the one of the reflected radiation received by the sensor.

2.5. The surface below the aerosol layer

Land surface usually has a strong impact on the satellite aerosol retrieval due to the strong radiation reflection. Moreover, the surface reflection cannot be easily modeled in the retrieval algorithm. The surface can be quite diverse with different land cover types and terrain, such as mountains with green forest and bare soil, and urban area with the

mixture of buildings and green vegetations, showing different reflectance characteristics.

For an accurate AOD retrieval, one needs to understand the reflection characteristic of the underlying surface and separate the surface and atmospheric contributions to the radiometric measurements. A lot of algorithms assume the surface to be a Lambertian reflector, i.e., isotropic reflection in all direction (e.g., Hsu et al., 2004; Levy et al., 2007b), to reduce the computational complexity and the number of unknown variables in the retrieval.

If the surface is assumed to be a Lambertian reflector, the contributions of the surface and the atmosphere to the radiance measured at TOA can be separated (Kaufman et al., 1997), viz (see Figure 2.3).

$$\rho^*_\lambda(i,v) \quad = \quad \rho^a_\lambda(i,v) + \frac{T_\lambda(i)\,T_\lambda(v)\,\rho^s_\lambda}{1 - s_\lambda \rho^s_\lambda}, \tag{2.8}$$

where radiance is normalized to the related reflectance through equation 2.9,

$$\rho(i,v) = \frac{\pi I(i,v)}{\cos\theta_s F_0} \tag{2.9}$$

the symbol "i" means the direction of the incident or solar flux, defined by solar zenith angle θ_s and solar azimuth angle ϕ_s, and "v" indicates the direction of the reflected flux into viewing or sensor, defined by sensor zenith angle θ_v and sensor azimuth angle ϕ_v (see Figure 2.2), λ indicates wavelength, ρ^s_λ is the reflectance of the Lambertian surface, ρ^a_λ is the normalized flux reflected by the atmosphere, $T(i)_\lambda$ is the normalized downward flux for zero surface reflectance, $T(v)_\lambda$ is the normalized upward total transmittance into the satellite field of view and s_λ is the atmospheric backscattering ratio. A Lambertian surface (Equation 2.8) has been assumed in MODIS AOD algorithm (dark target and deep blue) (Levy et al., 2007b; Hsu et al., 2004, 2006).

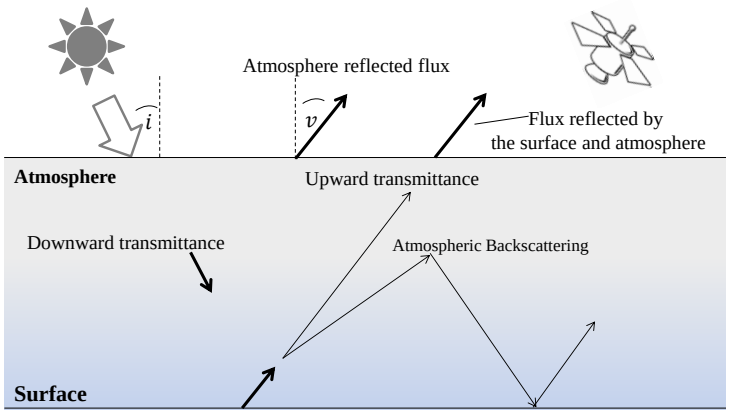

Figure 2.3: The TOA flux observed by the satellite when the surface is assumed to be a Lambertian reflector.

However, this assumption is generally inconsistent with the fact that the surface is well known to be non-Lambertian (anisotropic), i.e. with the reflectance strongly de-

pendent on the angle. Schaepman-Strub et al. (2006) illustrated how the Bidirectional Reflectance Distribution Function (BRDF) can be accounted using nine anisotropic reflectance properties. Many surface BRDF models have been applied in retrieval algorithms especially the ones designed for multi-angle viewing imaging radiometers (e.g., Martonchik et al., 1998; Dubovik et al., 2011; Lyapustin et al., 2011a,b; Pinty et al., 2000b,a, 2005, 2006).

2.6. Single scattering by an aerosol mixture

According to the C6_DT algorithm (Levy et al., 2013b), the total spectral ρ^{tot*} at the top of the atmosphere is assumed to be the weighted sum of the spectral reflectance in fine aerosol-dominated atmosphere (ρ^{f*}) and that in coarse aerosol-dominated atmosphere (ρ^{c*}), i.e.,

$$\rho^{tot*} = \eta\rho^{f*} + (1-\eta)\rho^{c*} \tag{2.10}$$

Where η is the fine / coarse aerosol ratio, and is defined in Remer et al. (2005). Aerosols with a particle size distribution characterized by a fine mode are moderately-absorbing (generic), absorbing (smoke) and weakly-absorbing (urban industrial) aerosols, whereas coarse aerosol is dust (Levy et al., 2007a, 2013a). This method to calculate the total spectral ρ^{tot*} is also called Standard Linear Mixing (SLM) method, which is exact for the single scattering in the atmosphere-surface system. For multiple scattering, the SLM method is still a good approximation due to the small difference in single scattering albedo between the 3 fine aerosol models. As compared to the Modified Linear Mixing (MLM) proposed by Abdou et al. (1997), the SLM method gives a small difference (< 1%) in the simulation of TOA reflectance.

2.7. Aerosol measurements

Both space-borne and ground-based instruments are used to observe the atmosphere and characterize aerosol. Here we introduce a few types of measurements that are used in our study, including MODIS, CALIOP and AERONET data.

MODIS data

The MODIS instrument is operated on board both the Terra and Aqua satellites, both observing the TOA radiance at 36 bands with spatial resolution from 250 m to 1 km (depending on bands and sensor viewing angle) (see Figure 2.4).

Terra and Aqua were launched in 1999 and 2002 respectively. The equator crossing times for Terra and Aqua are 10:30 and 13:30 local time respectively, monitoring the earth daily with nearly global coverage. The raw image data has a swath width of 2330 km. Since the footprint of the Instantaneous Field of View (IFOV) becomes larger as the across-track distance increases, the pixels near the edge are clipped, resulting in a swath width of 2030 km (e.g., Sayer et al., 2015). To obtain high quality measurements, onboard lunar calibration is applied by using onboard solar diffuser (SD) and SD stability monitor (Guenther et al., 2002; Xiong et al., 2003b,a,d,c, 2005d,a,b,c, 2007). Accuracy was found to be 2% for reflectance at Reflective Solar Bands (RSB) under typical conditions

(Toller et al., 2013). Recently, several studies demonstrated that the older MODIS onboard Terra is degrading (Levy et al., 2010, 2013b; Sayer et al., 2015), which would have impacts on the aerosol retrieval epsecially on the retrieval trend analysis (Levy et al., 2013b). This requires additional efforts to improve the radiometric quality by the MODIS team. MODIS Aqua data will be used for our aerosol retrieval.

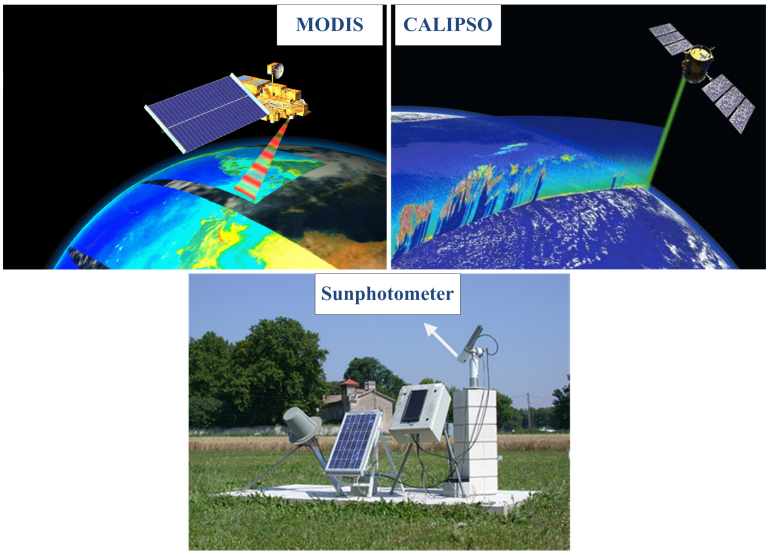

Figure 2.4: Schematic of MODIS, CALIOP instrument, and sun photometer. Figure courtesy of NASA MODIS, CALIPSO and AERONET team.

CALIOP data

CALIOP is a lidar instrument on board the CALIPSO satellite. This active lidar instrument retrieves the vertical profile of clouds and aerosols in the atmosphere by measuring the backscatter signal of its nadir-pointing laser at 532 and 1064 nm. It has been operational since June 2006. The fundamental sampling resolution of the data is 30 meters vertical and 333 meters horizontal. The samples located between -2 and 40 km (30 km for the 1064 nm) are used to generate the profile. The data acquired between 30 and 34 km are selected for the calibration as they contain virtually no signals from aerosol or clouds. In addition, an on-board averaging method was developed by considering that weaker signals are received from the higher atmospheric layers. This method produces full (lower) resolution in the lower (higher) atmosphere such that resolution of 30 m vertical (333 m horizontal) is only up to 8 km altitude (Winker et al., 2006). The averaging method would not affect the quality and usefulness of the data due to the relative homogeneity of the upper atmosphere (e.g., altitude between 20 and 40 km). More details about the calibration are described in Winker et al. (2006) and Hostetler et al. (2008).

CALIOP Level 1 and 2 data are produced by CALIPSO science team (Vaughan et al., 2005; Liu et al., 2005; Winker et al., 2006; Hostetler et al., 2008; Young et al., 2008). The Level 1 data is the measurement of attenuated backscatter coefficients at 532 and 1064

nm after instrument calibration. The Level 2 data provide users with the vertical features and properties of cloud and aerosols. One of the Level 2 products — Vertical Feature Mask (VFM) is generated from the Level 1 data with the feature finder algorithm that detects and determines cloud and aerosol layers (Vaughan et al., 2005).

AERONET AOD data

The sun photometers deployed in the global AERONET network acquire observations of the extinction of incoming direct solar radiation under cloud-free condition at a number of wavelengths (0.34, 0.38, 0.44, 0.67, 0.87, and 1.02 μm). These measurements are analyzed to characterize aerosols in terms of an AOD and probable aerosol type, at high frequency (e.g., every 15 min or better). These AOD retrievals have been systematically used in the validation of aerosol products derived from satellites because of their uniqueness and high quality (AOD uncertainties ~0.01-0.02).

2.8. MODIS collection 6 dark target algorithm over land

MODIS measurements include contributions due to light scattering from aerosols, clouds, atmospheric gases and the surface, as well as from multiple scattering due to the radiative interactions between those constituents. Algorithms have been developed to derive aerosol information from MODIS measurements. After several generations of development (from collection 4 to 6), the operational MODIS Dark Target (DT) AOD retrieval algorithm (C6) over land has been proven to be a mature algorithm. Compared to the previous versions, the current algorithm focused on the upgrade of the calculation at the MODIS central wavelengths, the estimation of Rayleigh Optical Depth (ROD) and the atmospheric gas correction. The core of the algorithm is still unchanged.

The algorithm can retrieve the AOD over vegetated areas using three channels (two visible 0.466- and 0.644 μm and one shortwave infrared channel 2.11 μm), where the surface is relatively dark at two visible channels and the atmosphere is nearly transparent at long wavelength (2.11 μm). It does not work well over bright surfaces e.g., arid zones and deserts, or snow and ice since its accuracy depends on the darkness of the surface target. Lambertian surface is assumed in the algorithm. Here, we give a brief introduction on the MODIS algorithm, including data preparation, ill-posed problems, assumptions on aerosol and surface properties and the retrieval procedure.

MODIS data preparation

Since the MODIS LUT is generated assuming a gas free atmosphere, the effects of gases need to be taken into account, prior to apply the retrieval procedure. Gases include water vapor (H_2O), ozone (O_3), and carbon-dioxide (CO_2) and other gases (e.g., N_2O and CH_4). For the gas correction, ancillary data are used i.e., gas optical depth from NCEP (National Center of Environment Prediction) (Levy et al., 2013b). If NCEP data are missing, then the US 1976 optical depths are used instead. This gas correction approach assumes that there is no interaction between gases and particulates in the atmosphere, and that their effects are additive.

In the algorithm, MODIS level 1B data are firstly processed for atmospheric gas correction (e.g., water vapor, ozone, and carbon dioxide), then aggregated into 20 × 20 pixels (500 m spatial resolution) for cloud mask and dark surface selection, resulting in the

mean reflectance (the dataset of "Mean_Reflectance_Land" in MODIS level 2 data) with the resolution of 10 × 10 km.

Ill-posed problems

In the MODIS algorithm, the surface effects on the AOD retrieval are mitigated by the dark target selection. However, this increases the number of unknowns which have to be determined with limited measurements (three single-viewing channels, 0.466-, 0.644 and 2.11 μm) that are insufficient to solve the inverse RT problem. This is a well known ill-posed problem since measurements are fewer than unknowns. For the AOD retrieval, many variables in the surface-atmosphere system need to be constrained, such as aerosol model and its vertical profile, and spectral surface reflectance.

"A priori" assumptions on aerosol and surface

Aerosol properties: fixed aerosol properties are applied in the MODIS algorithm. Based on geolocation and seasons, an aerosol model is selected among three non-dust aerosols (absorbing, moderately-absorbing, and weakly-absorbing). Aerosol layers are assumed to be static over the globe and dispersed within the atmospheric boundary layer (below 3 - 4 km), with an exponential decrease with altitude.

Parameterization of the spectral surface reflectance: a parameterization is applied to constrain the spectral surface reflectance in the retrieval. The parameterization is derived at two visible bands 0.466- and 0.644 μm and one shortwave infrared band 2.11 μm, by analyzing 4 years of co-located MODIS and AERONET data (Levy et al., 2007b). The relationship is assumed to be a function of scattering angle Θ and Normalized Difference Vegetation Index at infrared wavelengths ($NDVI_{SWIR}$) to account for its variability with surface type and geometrical illumination and viewing angle. $NDVI_{SWIR}$ is described in equation 2.18, where ρ^m is the TOA reflectance observed by MODIS. Note that $slope_{0.644/2.11}^{NDVI_{SWIR}}$ in Levy et al. (2007b) was corrected in Levy et al. (2013b). The corrected one is given here.

$$\rho^s_{0.644} = \rho^s_{2.11} \cdot slope_{0.644/2.11} + yint_{0.644/2.11} \tag{2.11}$$

$$\rho^s_{0.466} = \rho^s_{0.644} \cdot slope_{0.466/0.644} + yint_{0.466/0.644} \tag{2.12}$$

$$slope_{0.644/2.11} = slope_{0.644/2.11}^{NDVI_{SWIR}} + 0.002\Theta - 0.27 \tag{2.13}$$

$$yint_{0.644/2.11} = -0.00025\Theta + 0.033 \tag{2.14}$$

$$slope_{0.466/0.644} = 0.49 \tag{2.15}$$

$$yint_{0.466/0.644} = 0.005 \tag{2.16}$$

$$slope_{0.644/2.11}^{NDVI_{SWIR}} = \begin{cases} 0.58; & (NDVI_{SWIR} < 0.25) \\ 0.58 + 0.2(NDVI_{SWIR} - 0.25); & (0.25 < NDVI_{SWIR} < 0.75) \\ 0.48; & (NDVI_{SWIR} > 0.75) \end{cases} \tag{2.17}$$

with $NDVI_{SWIR}$ and Θ:

$$NDVI_{SWIR} = \frac{\rho^m_{1.24} - \rho^m_{2.11}}{\rho^m_{1.24} + \rho^m_{2.11}} \tag{2.18}$$

$$\Theta = \cos^{-1}(-\cos\theta_s\cos\theta_v + \sin\theta_s\sin\theta_v\cos(\phi_s - \phi_v)) \tag{2.19}$$

Algorithm implementation

The algorithm starts when the preparation of MODIS measurements is completed. With the aid of "a priori" assumptions on surface and aerosol parameters, the AOD is retrieved. The retrieval includes two steps: the (forward) simulation and retrieval (see Figure 2.5).

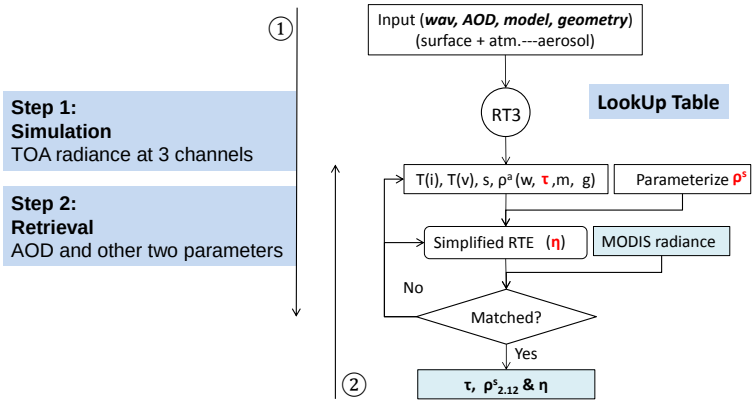

Figure 2.5: The MODIS aerosol retrieval algorithm with the LUT approach. The algorithm includes two steps: simulation of the TOA reflectance at the three channels and retrieval of AOD as well as other two parameters (red text).

Simulation: with the four parameters (ρ^a, $T(i)$, $T(v)$ and s) in the LUT, the TOA reflectance ρ^* is simulated at three channels (0.466-, 0.644- and 2.11 μm) using equation 2.8 and 2.10 (see step 1 in Figure 2.5). The simulations are iterated through 7 aerosol loadings (0.0, 0.25, 0.5, 1.0, 2.0, 3.0 and 5.0), 13 fine ratios ranging from -0.1 to 1.1 with the interval of 0.1 and the 2.11 μm surface reflectance. This gives a database on $\rho^* = \rho^*_\lambda(\tau,\eta,\rho^s_{2.11})$. Note that the spectral surface reflectance at the two visible wavelengths is not explicitly shown since they are parameterized as a function of the 2.11 μm surface reflectance. $\rho^s_{2.11}$ is also a function of aerosol loadings and fines ratios, i.e. $\rho^s_{2.11} = \rho^s_{2.11}(\tau,\eta)$.

Retrieval: the AOD retrieval is achieved by best fitting of the simulated TOA reflectance with the measured one in the three channels (see step 2 in Figure 2.5). At the same time, the other two parameters η and $\rho^s_{2.11}$ are also retrieved. In this process, there may be a fitting error ϵ, which gives the quality of the retrieval.

2.9. Conclusion

In this chapter, we have given an overview of the MODIS algorithm for AOD retrieval with satellite data, including the parameterization, simulation and retrieval technique applied in the algorithm. The definitions and parameterization of aerosol properties and surface reflection in the RT calculation have been explained. A simple and accurate

LUT simulation is applied, which includes coupling with a Lambertian surface. Finally, the operational MODIS algorithm (C6_DT over land) was introduced and discussed, including "a priori" assumptions on aerosol properties (the fixed aerosol model and static profile over the globe) and surface reflection (isotropic reflection).

The assumptions applied in C6_DT, however, lead to potential errors since these assumptions are inconsistent with the fact that aerosol properties vary greatly over time and space, including aerosol type and vertical profile and the land surface reflectance usually is anisotropic. Therefore, in the remainder of this thesis, improvements to the algorithm are proposed, tested and applied.

3

The sensitivity of AOD retrieval to aerosol vertical distribution and type

Based on: Wu, Y., de Graaf, M., and Menenti, M. (2016). The Sensitivity of AOD Retrieval to Aerosol Type and Vertical Distribution over Land with MODIS Data. *Remote Sensing*, 8(9):765.

3.1. Introduction

AOD retrieval by the MODIS algorithm assumes a fixed aerosol type with static vertical profile over the globe. The predefined aerosol properties cannot hold for unusual occurrences, such as smoke raised by forest fire versus the fixed aerosol type or the static profile, or dust lifted to high elevation versus the static profile, which may lead to inaccurate retrieval. To improve the retrieval accuracy, the effect of aerosol type and vertical distribution on the AOD retrieval should be well investigated and evaluated.

To understand these impacts on the AOD retrieval and further improve the retrieval, a sensitivity experiment was designed to investigate the variation of the retrieval due to the dynamic aerosol vertical profiles and different types with the MODIS C6_DT algorithm. In the experiment, synthetic data on the Top Of Atmosphere reflectance are simulated, using an off-line method with LookUp Tables (LUT). Section 3.2 presents the background on the MODIS aerosol retrieval, including the MODIS retrieval algorithm (Levy et al., 2007a, 2013b), and some aerosol climatology. Three non-dust models and one dust model from Levy et al. (2007a) are briefly introduced, as well as many kinds of aerosol vertical profiles. Section 3.3 gives the data and method applied in the sensitivity test. Four experiments are performed with extensive variability in aerosol properties. The experiment results and discussion are illustrated in section 3.4. Conclusions and recommendations are drawn in Section 3.5.

3.2. Background on MODIS Aerosol Retrieval

3.2.1. Aerosol Properties

Aerosol model

The MODIS C6_DT algorithm, applied to the dark surface, considers four aerosol models (3 non-dust and one dust) (Levy et al., 2007a, 2013a). The aerosol models are defined by the bi-lognormal size distribution and refractive indices, given in Table 3.1. More details about the size distribution are provided in Appendix A. The bi-lognormal distribution has two modes (fine and coarse), which is consistent with Dubovik's work that the particles with the radius < 0.6 μm are referred to as fine mode, those with radius size > 0.6 are referred to as coarse mode (Dubovik et al., 2002a). The size distribution and refractive indices uniquely determine the aerosol optical properties, such as single scattering albedo ω_0 and r_{eff}, and the phase function P. These optical properties describe the efficiency of aerosols scattering and absorption in the radiative transfer process. The optical properties of the four models are shown in Table 3.2 (ω_0 and r_{eff}), and in Figure 3.1 (P).

The particle size directly determines the scattering of the light, a schematic of scattering by a particle is shown in Figure 2.1 in Chapter 2. The effective radius of the four types is given in Table 3.2. The dust model presents a significant large particle size ($r_{eff} = 0.68$) as compared to the non-dust models ($r_{eff} < 0.261$). The particle size can be also seen in Figure 3.1 A, where the volume size distribution is given for the four aerosol models. Figure 3.1 B illustrates the corresponding phase function. Due to large particle size, the phase function of the dust presents a peak at the scattering angle of 0°, showing larger value than the non-dust models. From Table 3.2, we note that the smoke presents strong absorption with $\omega_0 = 0.87$, other two fine models present less.

It is possible that for some regions the predefined aerosol model is wrong. The errors

Aerosol Model	Mode	r_v (μm)	σ	V_0 ($\mu m^3/\mu m^2$)	Refracitve Index
Generic					
	Accum	0.1552	0.44205	0.0960	1.43 − 0.009i
	Coarse	3.2689	0.7782	0.0922	—
Smoke					
	Accum	0.1383	0.4231	0.09423	1.51 − 0.02i
	Coarse	3.92235	0.76375	0.06499	—
UrbanIndustrial					
	Accum	0.1821	0.44065	0.097227	1.42 − 0.00625i
	Coarse	3.39575	0.8414	0.05996	—
Speriod/Dust					
	Accum	0.1466	0.68238	0.04277	1.5017 − 0.002i
	Coarse	2.2	0.57429	0.32618	—

Table 3.1: Aerosol physical properties. Four aerosol models are presented with bi-lognormal modes (accumulative and coarse). For each mode, three parameters are listed, including the volume modal radius r_v, standard deviation of the volume distribution σ, and total volume of the mode, V_0. Note that the parameters are given at wavelength of 0.55 μm and AOD = 0.5. The symbol of "—" indicates the same value as the above row. More details are illustrated in Levy et al. (2007a).

Aerosol Model	ω_0	r_{eff}, μm
Moderately Absorbing/Generic	0.920	0.261
Absorbing/Smoke	0.869	0.208
Non-absorbing/UrbanIndustrial	0.947	0.256
Speriod/Dust	0.953	0.680

Table 3.2: The properties of aerosol models used in MODIS C6 algorithm. Single scattering albedo ω_0 and effective radius r_{eff} for aerosol model are presented. Table courtesy of Levy et al. (2007a).

from this possible wrong assumption are investigated in this study.

Aerosol Vertical Distribution

Generally, the aerosol vertical distribution is controlled by the aerosol layer shape and the altitude of the layer lower or upper boundary, which can be modeled using an exponential, power, Gaussian or random function.

Varying the scale height h, exponentially-distributed aerosols tend to change more the layer shape and less the layer height. Thus, to clearly show the effect of the layer shape on the AOD retrieval, an exponential distribution is selected, which can be written as:

$$\tau_{\lambda,z_i} = \tau_\lambda(e^{-z_i/h} - e^{-z_{i+1}/h}) \tag{3.1}$$

where z is the altitude in the atmosphere (z_i starts from 0 km, i.e., the surface), τ_λ is spectrally dependent, hereafter we use τ for 0.55 μm unless specified otherwise.

Figure 3.2 shows the exponential distribution varying with the scale height h, ranging from 1 to 6 in steps of 1. With the increase of scale height, the profile becomes more homogeneous, since the aerosols are distributed more evenly over the column. ExpH1

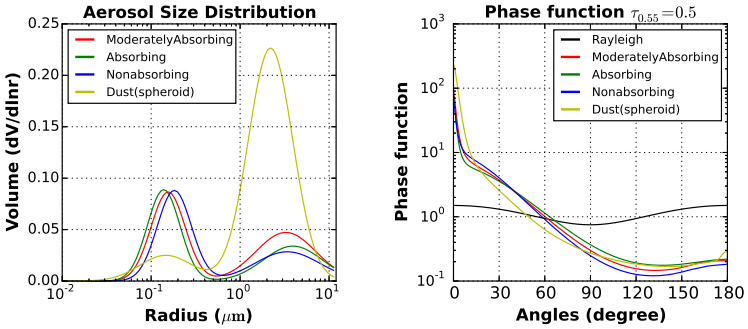

Figure 3.1: Size distribution and phase function for four aerosol models. The result is reproduced using the data provided by Levy et al. (2007a).

indicates the exponential distribution with the scale height of 1, other ExpH series follow the same rule. Note that one of ExpH series i.e., the ExpH2 distribution is applied in the MODIS C6_DT algorithm over land.

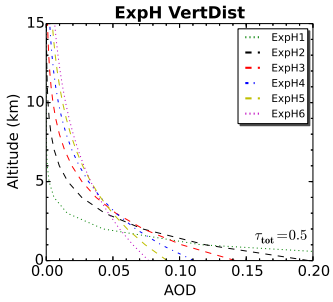

Figure 3.2: Exponential distribution as a function of scale height, ranging from 1 to 6 by step of one (see ExpH1, ExpH2,...and ExpH6). The total AOD (τ_{tot}) is set as 0.5. The tail of the distribution beyond 15 km is vertically cut off since the AOD becomes negligible at high elevation.

To demonstrate the effect of the layer height on the retrieval, two continuous aerosol layers (each layer is 1 km thick) in the atmosphere are assumed:

$$\begin{aligned} \tau_{\lambda,z_i} &= \tau_\lambda(e/(1+e)) \\ \tau_{\lambda,z_{i+1}} &= \tau_\lambda(1/(1+e)) \end{aligned} \tag{3.2}$$

The two-layer distributions are called Exp2L series, varying the bottom layer height from the surface to the altitude of 7 km. In the series, Exp2L0 means aerosols distributed from the altitude of the surface to 2 km, other Exp2L series follow the same rule.

Combining these two series (ExpH and Exp2L), we get 14 possible aerosol vertical distributions in total, where 6 distributions are from ExpH series and 8 distributions from Exp2L series.

3.3. Data and Method

Several studies demonstrated that there are some intrinsic uncertainties in the MODIS algorithm (C5_DT over land) (Kokhanovsky et al., 2010; Levy et al., 2007b). To better understand how the AOD retrieval is affected by the variability in aerosol properties, the intrinsic uncertainty needs to be fully evaluated and discussed before our sensitivity test. In addition, regarding the real case, we need to consider the uncertainty of both aerosol type and its vertical profile in the retrieval. Thus, we designed an experiment to evaluate the sensitivity of the AOD retrieval to aerosol type and vertical distribution by performing four experiments: (1) simulation of the "ideal" condition, i.e. when the algorithm assumptions on the choice of aerosol models and vertical profile are exactly valid; (2) simulation of the possible aerosol vertical profiles that are different from the algorithm assumption i.e. the static profile; (3) simulation of the possible aerosol types that are different from the algorithm assumption i.e. the predefined aerosol type; and (4) simulation of both aerosol vertical profiles and types being different from the algorithm assumptions.

The MODIS C6 DT algorithm over land (Procedure A) was used for the experiments. Note that Experiment 1 is designed to test the algorithm intrinsic errors, and Experiment 4 is used to test the interaction of aerosol vertical distribution and type on the retrieval. The set up of the experiments is given below.

3.3.1. Experiment Set up

With the four parameters (ρ^a, F_d, T and s) in LUT, the TOA reflectance was simulated for 3 aerosol mixtures (weakly-absorbing, moderately-absorbing and absorbing aerosols mixed with dust). Seven aerosol loadings (0.0, 0.25, 0.5, 1.0, 2.0, 3.0 and 5.0) and 5 fine ratios (0, 0.2, 0.5, 0.8 and 1) were used to characterize the mixtures. The experiment was done with 1520 geometrical combinations ($0° \le \phi \le 180°$, $\theta \le 60°$, $\theta_0 \le 48°$). For the experiment, we assumed that the surface reflectance at 2.11 μm $\rho^s_{2.11}$ was 0.15 with the ratios for visible bands (0.466 and 0.644 μm) versus 2.12 μm (i.e., $\rho^s_{0.644} = 0.5\rho^s_{2.11}$ and $\rho^s_{0.466} = 0.25\rho^s_{2.11}$).

To perform Experiments 2 and 4, we need to create the corresponding LUTs with the different aerosol vertical distributions (14 in total). As for Experiments 3 and 4, aerosol models applied in the simulation are different from that in the retrieval.

In the experiments, the relative difference $\delta(\tau)$ of the AOD retrieval is defined as:

$$\delta(\tau) = \frac{\tau - \tau_{\text{ref}}}{\tau_{\text{ref}}} \tag{3.3}$$

where the subscript ref means the reference value of τ. For Experiment 1, the AOD used in the forward calculation (simulation) is viewed as the reference, whereas for the other Experiments, the retrieved AOD with ExpH2 is viewed as the reference. The results of the experiments are summarized by averaging 1520 geometrical combinations unless specified otherwise.

3.4. Experiment Results and Discussions

3.4.1. Experiment 1

Result

Figure 3.3 presents the results with a moderately absorbing aerosol model (generic). In this figure, we note that the AOD is always overestimated while the surface reflectance is underestimated. The errors on the four parameters increase with the mixing ratio between fine and coarse aerosol, and become larger as aerosol loading increases. For instance, the largest relative error $\delta(\tau)$ (7%) was found when the fine ratio η is 0.5 under extreme heavy loading ($\tau = 5.0$). Accordingly, the retrieved fine ratio also give errors of about 16% (0.08). Nevertheless, under aerosol loading $\tau \leq 0.5$, the errors become small (<0.2%). The results with other aerosol models show a similar uncertainty (not shown here).

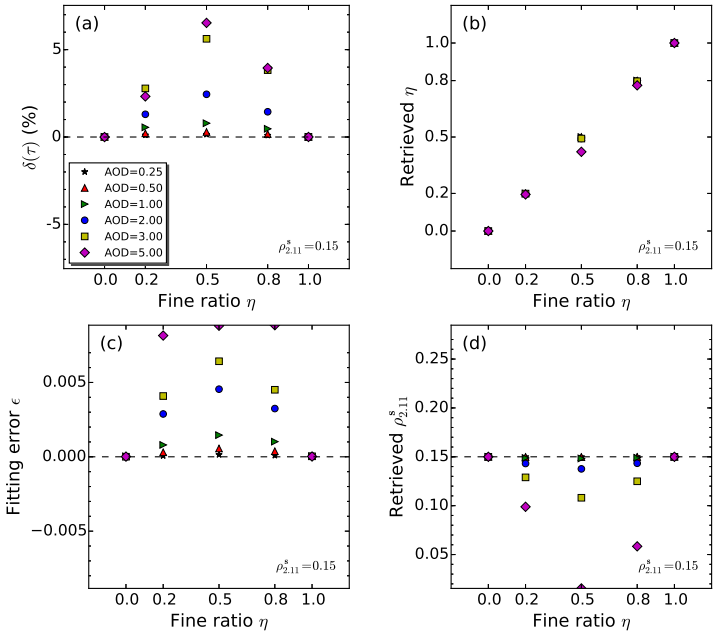

Figure 3.3: The uncertainty of four retrieval parameters as function of fine ratio η in C6 algorithm. Note that the result is achieved by averaging the values of the parameters (τ, η, ϵ, and $\rho^s_{2.11}$) over 1520 geometrical combinations, assuming aerosol model as Moderately absorbing (Generic model in the figure) with the surface reflectance $\rho^s_{2.11} = 0.15$ in the retrieval. (**a**) shows the relative difference of mean AOD between the retrieved and the expected one (reference) (e.g., when aerosol loading is set as 0.5, then the expected AOD should be 0.5 exactly); (**b**–**d**) show the mean values of fine ratio η, fitting error ϵ and the surface reflectance $\rho^s_{2.11}$, respectively.

Discussion

To check the intrinsic error source and its potential effects on the sensitivity test, we recoded the C6_DT standalone algorithm with the complete understanding of the procedure implemented in the algorithm. We found that the intrinsic errors are attributed

to the underestimation/overestimation of the 2.11 μm surface reflectance $\rho^s_{2.11}$, shown as two issues:

- Issue 1: In the MODIS algorithm, the $\rho^s_{2.11}$ is firstly determined, given as a function of the atmospheric condition (aerosol loadings and fine ratios). Obviously, this is inconsistent with the fact that the surface reflectance is invariant with the atmospheric condition. The $\rho^s_{2.11}$ should be independently retrieved as the other two free variables (τ and η).
- Issue 2: to find the possible $\rho^s_{2.11}$ with the rearranged Equation (2.10), the MODIS measurement is expected to be divided into two parts: one part is the reflectance from fine-mode dominated atmosphere, and the one from coarse-mode dominated atmosphere, while the algorithm assumes the measurement to be identical to each part. By doing this, the uncertainty of the retrieval with heavy aerosol loading becomes large. Nevertheless, the uncertainty is expected to be small with low aerosol loading since the TOA reflectance is dominated by the surface contribution and little affected by the atmospheric aerosol.

Figure 3.4 illustrates Issue 1 in the algorithm. In this figure, we selected a simulation with generic mixture ($\eta = 0.5$ and $\tau = 0.5$) under a given geometry (nadir view and $\theta_0 = 24°$). Figure 3.4a shows the derived $\rho^s_{2.11}$ as a function of aerosol loading and fine ratio. This $\rho^s_{2.11}$ was used to generate the surface reflectance at two visible bands (0.466 and 0.644 μm) with the experimental relationship of surface reflectance for VISvs2.11 (see equation 2.12 and 2.11), resulting in the simulated TOA reflectance at the two visible bands (see Figure 3.4b). From Figure 3.4b, we can clearly see that the simulation significantly deviates from the truth, showing a clock-wise twist around the point (located at $\eta = 0.5$ and $\tau = 0.5$). This is due to the algorithm allowing the surface reflectance $\rho^s_{2.11}$ to vary with the atmospheric conditions.

Figure 3.5 presents Issue 2 in the algorithm. In this figure, we chose similar synthetic data as in Figure 3.4 (the effect of Issue 1). Note that the data are generated with heavy aerosol loading ($\tau \geq 2.0$). To remove the effect of Issue 1, the aerosol loading and fine ratio are assumed as known in the retrieval. From Figure 3.5b, we note that the simulation is always lower than the truth, and this becomes significant for the extreme heavy aerosol mixture ($\tau = 5.0$ and $\eta = 0.5$). This would cause the overestimation of the AOD retrieval.

The intrinsic errors in the AOD retrieval are attributed to the wrong estimation of the surface reflectance (the net effect of Issues 1 and 2). These errors could introduce extra uncertainty in the sensitivity test (Experiment 2 to 4), since a distorted (twist and compact) simulation space is created in the retrieval due to the incorrect estimation of the surface reflectance. Nevertheless, the experiments still can reveal the retrieval errors of the algorithm when the aerosol properties are not properly defined.

3.4.2. Experiment 2

Result

Figure 3.6 presents the AOD errors with the four simulations (ExpH2, ExpH3, Exp2L0 and Exp2L3), where the ExpH2 LUT is applied in the retrieval process. The result with the

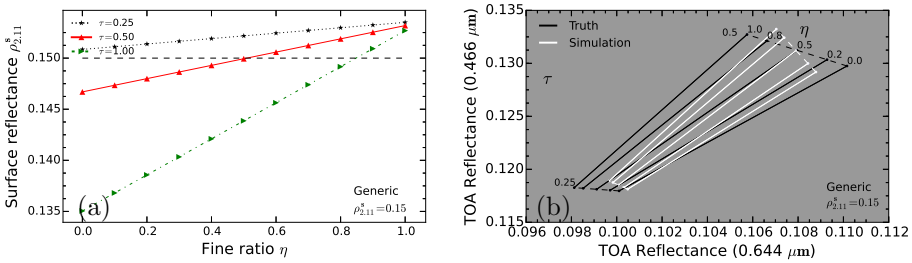

Figure 3.4: The surface reflectance $\rho^s_{2.11}$ and simulation in the retrieval (Issue 1). These parameters are produced by the C6_DT algorithm with a synthetic measurement. The mixture of generic + dust (η = 0.5 and τ = 0.5) is selected to construct the synthetic data at the given geometrical angle (nadir view, $\theta_0 = 24°$). In the algorithm, the possible values of $\rho^s_{2.11}$ are obtained (**a**), shown as a function of aerosol loading and the fine ratio. Note that the $\rho^s_{2.11}$ was plotted out only with aerosol loading (0.25, 0.5 and 1.0), shown as "black *", "red triangle" and "green triangle", respectively. Other values with large aerosol loading were not shown. With the experimental relationship of surface reflectance for VISvs2.11, the possible $\rho^s_{2.11}$ is further applied to generate the simulation for the TOA reflectance at two visible bands (0.466 and 0.644 μm) at each node of aerosol loading (0.25 and 0.5) and fine ratio, given in (**b**). "White" line indicates the simulation, where "solid "and "dash" line means the simulation varied with aerosol loading and fine ratio, respectively. To compare with the simulation, the corresponding "truth" value is also given, plotted as "black" line.

smoke model is given. The results with other models are not shown due to the relatively small errors. We can see that the errors are substantially related to the aerosol vertical distributions. Concretely, the cases with a higher aerosol layer (e.g., ExpH3 and Exp2L3) cause the underestimation of the retrieved AOD. In contrast, the simulation with a lower aerosol layer (e.g., Exp2L0) causes the overestimation. This become more significant with the absorbing (smoke) or large size aerosols (dust) as the aerosol loading increases. Normally, the errors with the smoke and dust ($\eta = 0$ in Figure 3.6) range from 5% to 15%, while showing smaller values (<5%–8%) with urban industrial and generic model.

To further clarify the sensitivity of the AOD retrieval to the vertical distribution, we performed the retrieval with the simulations which were created with 14 distributions (6 "ExpH" and 8 "Exp2L"). Pure smoke and dust were selected with τ = 0.5. To check whether the sensitivity is dependent on the illumination/viewing geometry, we performed the numerical experiement with five angles, which are described as: solar zenith angles of 0°, 12°, 24°, 36° and 48° under nadir view. We change the reference AOD in the evaluation, where the AOD obtained with the "ideal" simulation with ExpH2 and Exp2L0 was selected as "reference" for "ExpH" and "Exp2L" series, respectively.

Figure 3.7 presents the AOD errors with "ExpH" and "Exp2L" series distributions, where the smoke model is given. It seems that the retrieval is more sensitive to the "Exp2L" series than to the "ExpH" series. The errors $\delta(\tau)$ are from 5% to 10% with "ExpH" simulations, whereas they are from 3% to over 20% with "Exp2L" simulations. The errors are strongly dependent on the angles, showing an increase with the decrease of the solar zenith angle (or with the increase of the scattering angle). Focusing on the Exp2L4 simulations, we can see the error $\delta(\tau)$ is 10% at the angle $\theta_0 = 0°$, and increasingly large (25%) at the angle $\theta_0 = 48°$. Generally, the large difference between the vertical distributions would give a significant error $\delta(\tau)$. Specifically, the AOD difference increases linearly

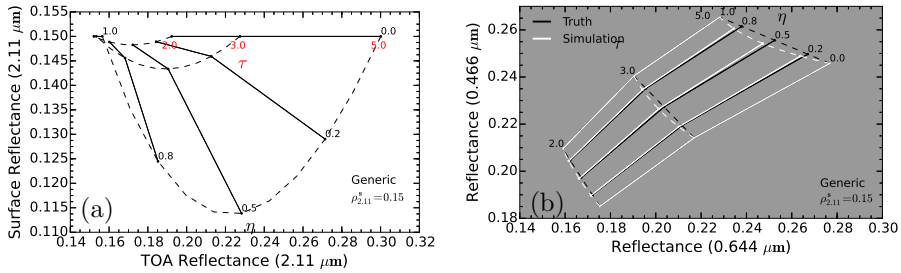

Figure 3.5: The surface reflectance $\rho^s_{2.11}$ and simulation in the retrieval (Issue 2). Selected was similar synthetic data as in Figure 3.4, but with heavy aerosol loading ($\tau \geq 2.0$). Note that that the aerosol loading and fine ratio are assumed as known for the simulation. The possible surface reflectance $\rho^s_{2.11}$ varies with aerosol loading and fine ratio, given as "solid" and "dash" line, respectively in (**a**). The corresponding simulation of TOA reflectance is given in (**b**). Other symbols are similar to Figure 3.4.

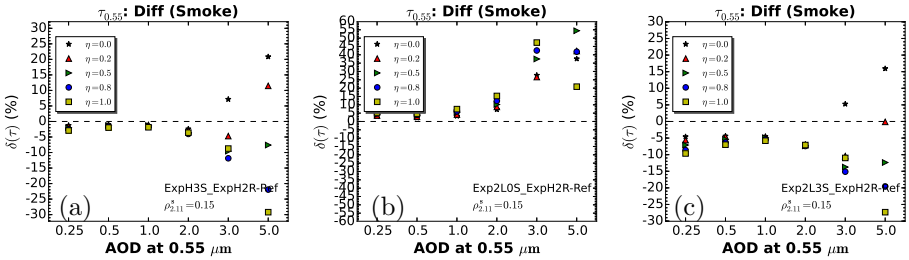

Figure 3.6: The AOD errors caused by different aerosol vertical distributions. The errors $\delta(\tau)$ are calculated by averaging over 1520 geometrical combinations, shown as a function of aerosol loadings in (**a**–**c**); In (**a**), the label of "ExpH3S_ExpH2R-Ref" indicate the AOD difference $\delta(\tau)$ between "ExpH3_ExpH2R"and "Ref", where "ExpH3S_ExpH2R" means the AOD is achieved with ExpH3 simulation, but using ExpH2 LUT in the retrieval. As for "Ref", the AOD is retrieved with ExpH2, using the LUT with the same distribution as in the simulation. Other labels are similar too.

with the layer height ("Exp2L "series) in Figure 3.7. For example, with nadir view and solar zenith angle $\theta_0 = 24°$, we can see that there is a linear increase of the $\delta(\tau)$ between Exp2L1, Exp2L4 and Exp2L7, with the AOD errors of 5%, 15% and 20%, respectively.

Discussion

For the case of an elevated aerosol layer (e.g., Exp2L3 relates to Exp2L0), the TOA reflectance presents lower values due to less isotropic scattering reflected by the Rayleigh layer under the aerosol layer. With the increase of the aerosol-mixture layer height, the TOA reflectance decreases at short wavelength (e.g., 0.466 μm), which leads to a reduction of AOD retrieval.

Figure 3.8 presents the Exp2L simulation series (7 points) falling within the Exp2L0 simulation space. The result is shown with the smoke model. From this figure, we can see that the 0.466 μm reflectance at TOA is significantly decreasing with the increase of the layer height (Exp2L0 → Exp2L7). The reflectance with ExpH series also shows a similar trend, where the mean layer height is determined by the scale height (not shown).

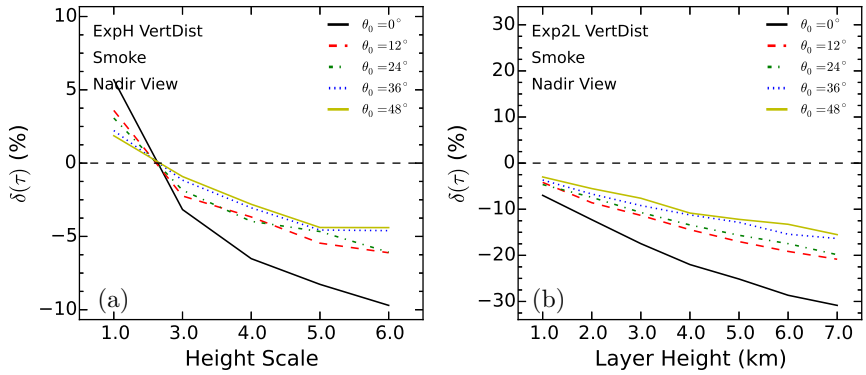

Figure 3.7: The AOD errors caused by different aerosol vertical distributions. The AOD obtained with the "ideal" simulation with ExpH2 and Exp2L0 was selected as "reference" in the comparison of the retrieval with "ExpH" and "Exp2L" series, respectively. The difference for "ExpH" and "Exp2L" are given in (**a**,**b**), respectively. Note the results are obtained with pure smoke aerosol at $\tau = 0.5$, under 5 angles (nadir view with 5 solar zenith angles θ_0). The 2.11 μm surface reflectance is set as 0.15.

With a given aerosol vertical distribution related to the "reference" one, the effect is different for different aerosol models, where the magnitude of the effect is mainly dependent on their single scattering albedo ω_0 (see Table 3.2). The Rayleigh scattering under the aerosol layer is more absorbed by the strongly-absorbing aerosol layer, leading to much lower TOA reflectance. Therefore, the effect becomes larger with strongly-absorbing aerosols. This is the main reason why the largest difference $\delta(\tau)$ (30%) is found with the smoke model since the model has the lowest single scattering albedo ($\omega_0 = 0.869$).

The impact of illumination and viewing geometry on the sensitivity to aerosol vertical distribution depends on the optical properties, especially on the phase function of the aerosol mixture. The atmospheric scattering is attenuated with increasing scattering angle (see Figure 3.8) due to the shorter atmospheric path. However, it is not the case for the dust-dominated atmosphere, in which the atmospheric scattering is still strong at a large scattering angle due to the peak forward scattering of the dust (see phase function in Figure 3.1b). In addition, the discrepancy of the TOA reflectance caused by the vertical distributions does not change too much with different scattering angles. As a result, the AOD errors due to the vertical distribution strongly depends on the scattering angle.

3.4.3. Experiment 3

Result

Figure 3.9 presents the AOD errors due to a wrong assumption on the aerosol model, where the generic and smoke model were used for the forward simulation but using the urban industrial LUT in the retrieval. Some abbreviations of aerosol models are used (G: Generic, S: Smoke, U: Urban industrial). Averaging over 1520 geometrical combinations, the error $\delta(\tau)$ is roughly <8% under $\tau \leq 1.0$, and increases under the heavy aerosol loading ($\tau \geq 2.0$) with the value >8%. Obviously, the improper selection of the pure aerosol

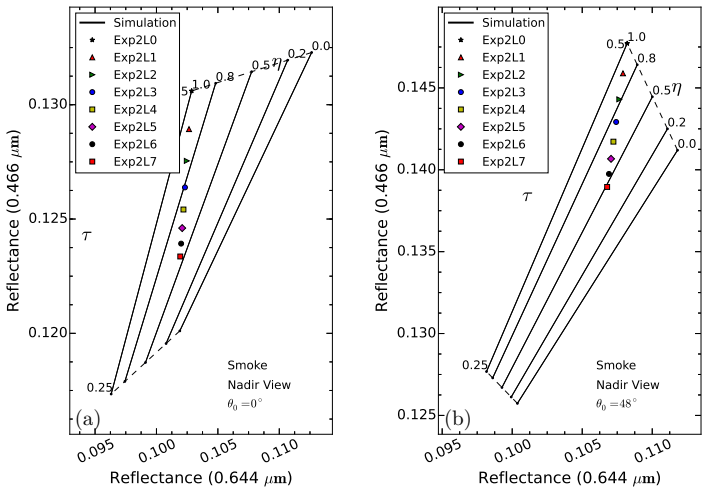

Figure 3.8: The simulations with smoke model, under a given viewing geometry. (**a**,**b**) show the results with nadir view and solar zenith angle $\theta_0 = 0°$ and $\theta_0 = 48°$, respectively. The Exp2L simulation series are created with $\tau = 0.5$, shown as 7 points in the figure. The 2.11 μm TOA reflectance is not shown due to its near nonsensitivity to the aerosol vertical distribution. The $\rho^s_{2.11}$ is set as 0.15.

($\eta = 1.0$) gives the largest errors compared to the case with the other aerosol mixtures.

The sensitivity of the retrieval to aerosol type is further evaluated, using pure aerosols. Similar to Experiment 2, the simulation is with $\tau = 0.5$, at 5 angles. The result is shown in Figure 3.10, giving comparable errors <8%. This means that the retrieval presents a medium sensitivity to the aerosol type. With different angles, the sensitivity does not vary too much with the discrepancy <5%. There is an approximate symmetry in the difference between the pairs such as S_U (smoke simulated but with urban industrial in the retrieval, U_S, G_S and others are similar to S_U) and U_S, presenting an overestimation of AOD in S_U and underestimation in U_S with nearly the same degree.

Discussion

Due to a relatively small difference of the single scattering albedo between non-dust aerosols, the AOD retrieval does not change too much with a different aerosol model when aerosol loading is low (e.g., $\tau \leq 0.5$). As aerosol loading increases, the error of the AOD retrieval becomes significant especially for the large difference between the observed and simulated aerosol, such that the strongly absorbing aerosol (smoke, $\omega_0 = 0.869$) is wrongly assumed as non-absorbing one (urban industrial, $\omega_0 = 0.947$), the error cloud be up >10%.

The sensitivity of the retrieval to aerosol type does not show a strong dependence on the zenith angle as in Experiment 2. This is because the non-dust aerosol models are nearly isotropic in their phase function (see Figure 3.1).

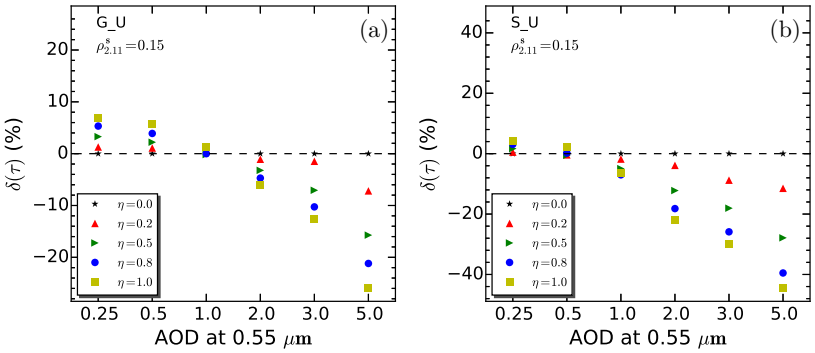

Figure 3.9: The AOD errors by wrongly assuming aerosol models. The mean errors $\delta(\tau)$ are calculated by averaging over 1520 geometrical combinations, with $\rho^s_{2.11}$ = 0.15, shown as a function of aerosol loadings. The "reference" AOD is the one that is achieved in the algorithm by the correctly choosing aerosol model. Some abbreviations of aerosol models are used (G: Generic, S: Smoke, U: urban industrial). "G_U" in (**a**) means the relative difference between the result with that generic aerosol is observed while urban industrial one is given in the retrieval and "reference". Similarly, the result with "S_U" is shown in (**b**).

3.4.4. Experiment 4

To show the interplay effect on the AOD retrieval by the improper assumption of both the aerosol vertical distribution and type on the AOD retrieval, we selected two aerosol models (smoke and urban industrial) and vertical distributions (ExpH2 and Exp2L3) in this experiment. Specifically, for the experiment, the simulation is created using the smoke aerosol with Exp2L3 distribution, but using the LUT of urban industrial with ExpH2 distribution. The result is given below.

Figure 3.11 illustrates the AOD errors in this experiment. The result is roughly equivalent to the one that negatively biases the result in Figure 3.9b. In this figure, we can see that the AOD retrieval is significantly overestimated, with $\delta(\tau) > 6\%$. For example, when aerosol loading is 1.0, the error could be up to 15% in this case.

3.5. Conclusions & Recommendation

It is well-known that the aerosol properties are one of largest uncertainty sources in the MODIS algorithm since the assumption of the fixed aerosol properties remains in Collection 5 and 6. With the aid of the Cloud-Aerosol Lidar and infrared Pathfinder Satellite Observation (CALIPSO) that can provide aerosol information about its type and vertical profile, we might put constraints on the aerosol properties to improve the retrieval. However, as the first step of the improvement, the retrieval uncertainty caused by improper assumptions should be quantified. In this study, we designed experiments to evaluate the sensitivity of the retrieval to aerosol vertical distribution and type. Four experiments were performed with the C6_DT algorithm over land, where the intrinsic uncertainty is also evaluated.

Due to the uncertainty in estimating the surface reflectance, it was found that there is intrinsic uncertainty in the algorithm, with the AOD retrieval error below 0.2% and >3% under low aerosol loading ($\tau \leq 0.5$) and heavy aerosol loading ($\tau > 3.0$), respectively.

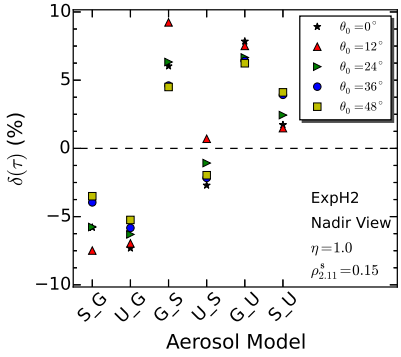

Figure 3.10: The AOD errors by wrongly assuming aerosol models. Note the results are calculated with $\eta = 1.0$ and $\tau = 0.5$ at five angles (nadir view with 5 solar zenith angles θ_0). The other symbols are the same as that in Figure 3.9.

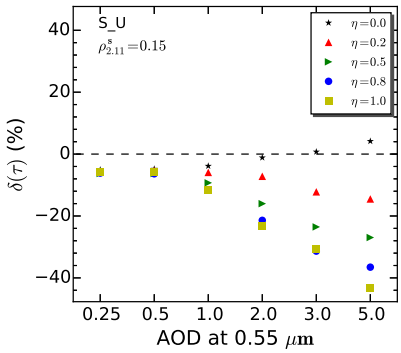

Figure 3.11: The AOD errors by wrongly assuming aerosol vertical distribution and type. The smoke aerosol with Exp2L3 distribution is used in the simulation, but using the LUT of urban industrial model with ExpH2 in the retrieval. Note that the experiments were carried out with $\rho^s_{2.11} = 0.15$. The other symbols are the same as that in Figure 3.9.

The algorithm shows high sensitivity to both aerosol vertical distribution and type of the retrieval.

- With the simulations varied with 4 vertical distributions (ExpH2, ExpH3, Exp2L0 and Exp2L3), about 5% errors can be found in the retrieval. Even larger errors are shown in ExpH and Exp2L simulation series, ranging from 2% to 30% when aerosol loading of 0.5 is assumed. In the vertical distribution, the aerosol layer height is the main variable that affects the retrieval, where the errors significantly increase with the aerosol layer height.

- Furthermore, the errors caused by the layer height present a strong angular dependence due to the large discrepancy of the phase function between non-dust and dust aerosols.

- Generally ($\tau \leq 0.5$), errors in aerosol type assumption can lead to uncertainty up to 8% in the AOD retrieval with the algorithm. By combining the uncertainty of the aerosol type (urban industrial replaced with smoke) with its vertical profiles (ExpH2 replaced with Exp2L3), the AOD errors present a significant negative bias with $\delta(\tau)$ >6%. The errors can be up to 15% when aerosol loading of 1.0 is observed.

In addition, sensitivity to the aerosol properties of the retrieval is insignificant for weakly- and non-absorbing aerosols (e.g., urban industrial and generic) especially when low aerosol loading is observed. Thus to improve the retrieval, more attention should be paid to the cases of air pollution caused by forest fires or extreme dust events. These cases usually are consistent with a heavy and thick elevated aerosol layer, and have a strong impact on climate regionally and globally. We assume that for these cases the bias of the MODIS AOD retrieval can be reduced by 15% based on this study. We also note that the algorithm intrinsic uncertainty refers to the retrieval techniques. This uncertainty should be reduced to near zero by optimizing the retrieval techniques especially the estimation of the surface reflectance. This would help further improve the retrieval accuracy especially when dealing with heavy aerosol loading.

4

Retrieval of AOD using CALIPSO to capture aerosol vertical distribution: case study over dust and smoke regions

Based on: Wu, Y., de Graaf, M., and Menenti, M. (2017). The impact of aerosol vertical distribution on aerosol optical depth retrieval using CALIPSO and MODIS data: case study over dust and smoke regions. *JGR-atmosphere, 122(16):2016JD026355.*

4.1. Introduction

In the previous chapter, we have demonstrated that the AOD retrievals are quite sensitive to the variation of aerosol vertical profile and type. The previous study was still limited to synthetic data. However, for a real case, it needs a further and deeper investigation to understand the impact of dynamic aerosol properties on the retrieval.

In this study, we developed a new algorithm (called Gau_DT) to retrieve the AOD by considering a dynamic aerosol profile with the synergistic use of MODIS and CALPSO data. The inferred aerosol vertical profile from CALPSO data is parameterized into the algorithm to generate an accurate Top Of the Atmosphere (TOA) reflectance for the AOD retrieval. Section 4.2 introduces the Gau_DT algorithm, including the investigation of the relationship between the profile and TOA reflectance, as well as the discussions on the sensitivity of the AOD retrieval to the variation of the profile. Section 4.3 introduces CALIPSO Level 2 data and the derivation of aerosol vertical distribution from it. Section 4.4 provides case studies (smoke and dust aerosol) to show the impact of aerosol vertical distribution on the AOD retrieval with the comparison between Gau_DT and C6_DT AOD. Conclusions are presented in section 4.5.

4.2. Method

The new algorithm is based on the MODIS C6_DT algorithm (Levy et al., 2007b, 2013b). The aerosol vertical distribution and its parameterization in the new algorithm are detailed as below.

4.2.1. Aerosol vertical distribution

The distribution of aerosols in the atmosphere can be very diverse and be different at different elevations. Different distributions of aerosol in different atmospheric layers have been applied in a number of studies. For example, the Gaussian distribution was applied for the dust layer in the Deep Blue AOD algorithm (Hsu et al., 2004), for typical smoke to retrieve the layer height (Lee et al., 2015), and in the POLDER aerosol retrieval algorithm (Dubovik et al., 2011), whereas the exponential distribution was applied for all aerosol models in the MODIS DT AOD algorithm over land (Levy et al., 2007b).

The distribution of aerosols in a layer can be represented as Gaussian and exponential function, as well as power law or random function. To reduce the number of the distributions, we classified them into two groups based on their characteristics. Exponential and power law functions are lumped into one group, because both of them indicate more aerosols in the lower boundary layer and less in the upper boundary layer. Random and Gaussian distributions are lumped into another group. The random distribution with a limited geometric thickness (e.g., 2 km) to some degree can be viewed as a homogeneous layer, thus can be approximately represented as a Gaussian function. Thus, exponential and Gaussian distributions were selected for further analysis.

The vertical profile (layer shape and altitude) is controlled by one or two variables in the selected distributions such as a scale height h in the exponential distribution (see equation 3.1 and Figure 3.2), and the mean height μ and the thickness σ of the aerosol

layer in the Gaussian distribution:

$$\tau_{\lambda,z_i} = \tau_\lambda \frac{1}{\sqrt{2\pi}} (e^{-(z_i-\mu)^2/2\sigma^2} - e^{-(z_{i+1}-\mu)^2/2\sigma^2}) \quad (4.1)$$

where z_i is the altitude of the ith aerosol layer.

For the Gaussian distribution, aerosol layers are assumed to have a limited thickness, where the aerosol particles are truncated into the interval of Gaussian 2-σ. We note that with a low mean height (e.g., μ = 0 km) the Gaussian distributions will give some aerosols below the surface. This is invalid for the real case. To avoid this situation, we keep the aerosols above the surface and remove the aerosols below the surface, but the total amount of aerosol is still kept the same as other normal cases (e.g., $\mu >= 3$). Additionally, the vertical resolution of the aerosol layer is also taken into account since the resolution can change the layer shape. Six kinds of Gaussian distributions (Gau1 → Gau6) are given in Table 4.1 and shown in Figure 4.1. They differ in three variables: mean height (0 and 3 km), geometrical thickness (0.5 and 1 km) and vertical resolution (0.5 and 1 km).

Name	μ or h (km, depending on distribution)	σ (km)	Resolution (km)
Gau1	0	0.5	0.5
Gau2	0	1.0	0.5
Gau3	0	1.0	1.0
Gau4	3	0.5	0.5
Gau5	3	1.0	0.5
Gau6	3	1.0	1.0
GauH0	0	1.0	1.0
GauH1	1	1.0	1.0
...	...	...	...
GauH10	10	1.0	1.0
ExpH1	1	—	1.0
ExpH2	2	—	1.0
...	...	...	...
ExpH6	6	—	1.0

Table 4.1: Gaussian (Gau1 → Gau6 and GauH0 → GauH10) and Exponential distributions (ExpH1 → ExpH6) of aerosol layers varying with the mean height μ or the height scale h. The geometric thickness σ of the layers is applicable for Gaussian distributions. The symbol of "—" indicates a missing value for Exponential distributions. Considering the limited aerosol-atmosphere layers in RT code, vertical resolutions of 0.5 and 1.0 km for the layers are also given.

The relationship between the TOA reflectance and aerosol vertical distribution

To parameterize the aerosol vertical profile into the algorithm, the relationship between the TOA reflectance and aerosol vertical profile needs to be quantified. Since the TOA reflectance is nearly insensitive to the aerosol vertical profile at long wavelengths (e.g., 0.644 and 2.12 μm) (Wu et al., 2016b), we focused on the variation of the TOA reflectance at short wavelength (0.466 μm) over the different profiles including 6 Gaussian (Gau1 → Gau6) and 6 exponential distributions (ExpH1 → ExpH6) (see Table 4.1).

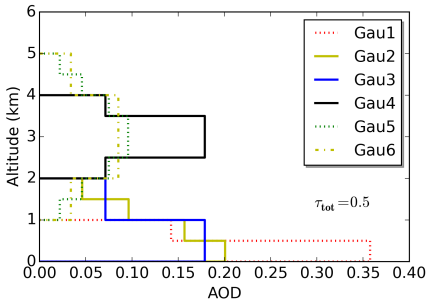

Figure 4.1: Discrete Gaussian distributions. The distributions shown in the figure is also given in Table 4.1. The total AOD τ_{tot} is set as 0.5.

Figure 4.2 presents the simulated 0.466 μm reflectance at TOA with Gaussian distributions (Gau1 → Gau6). Smoke and dust models were used. The TOA reflectance is nearly insensitive to the shape of the aerosol vertical distribution such as the geometrical thickness and vertical resolution of the aerosol layer, while it shows high sensitivity to the mean height. The result with exponential distributions is similar (not shown here). A similar result was also demonstrated in Lee et al. (2015). We found that the TOA reflectance with dust model presents less variation with the mean height than with smoke model. This is because dust is less absorbing than smoke.

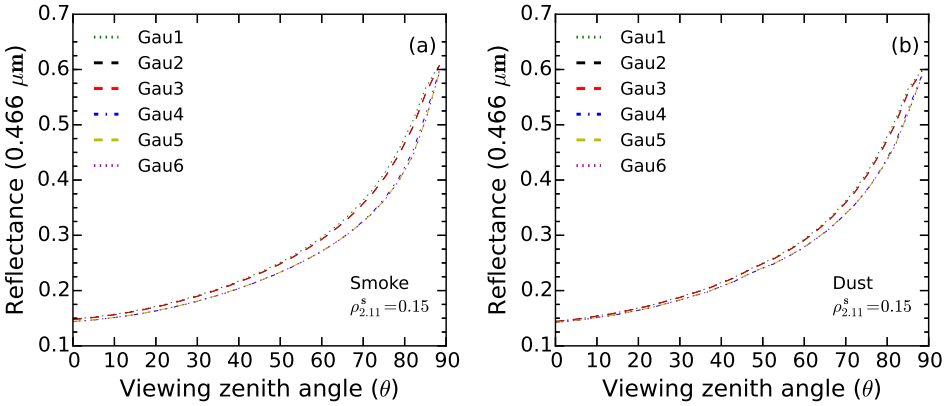

Figure 4.2: The TOA reflectance at 0.466 μm when the Gaussian distributions "Gau1-6" are used. The definition of these distributions is also shown in Table 4.1. The reflectance is calculated for the smoke (a) and dust model (b) with a given Solar zenith angle θ_0 = 48° and relative azimuth angle ϕ = 180° , AOD (0.5) and surface reflectance $\rho^s_{2.11}$ = 0.15. We assume that the surface reflectance ratios of 0.466/2.11 and 0.644/2.11 are 0.25 and 0.5, respectively.

Since the mean height is a major factor that influences the TOA reflectance, it is expected that the TOA reflectance with Gaussian distribution is similar to the one with exponential distribution when their mean heights are equal. To prove this, we simulated the TOA reflectance with one exponential ExpH2 and two Gaussian distributions (μ = 0

and $\mu = 3$, labeled as "GauH0" and "GauH3", respectively).

Figure 4.3 illustrates the TOA reflectance with the three distributions (ExpH2, GauH0 and GauH3), given as a function of viewing angles. From this figure, we can see that the ExpH2 reflectance mostly falls within the envelope of the GauH0 and GauH3 reflectance. Note that in ExpH2 distribution the mean height is $-2\ln(0.5) = 1.4$ km (between 0 and 3 km). Nevertheless, with a large viewing angle (e.g, $\theta_v > 80°$), the TOA reflectance with ExpH2 distribution is less than that with GauH3. This is mainly due to different vertical slant path depending on layer/height thickness in the calculation of radiative transfer.

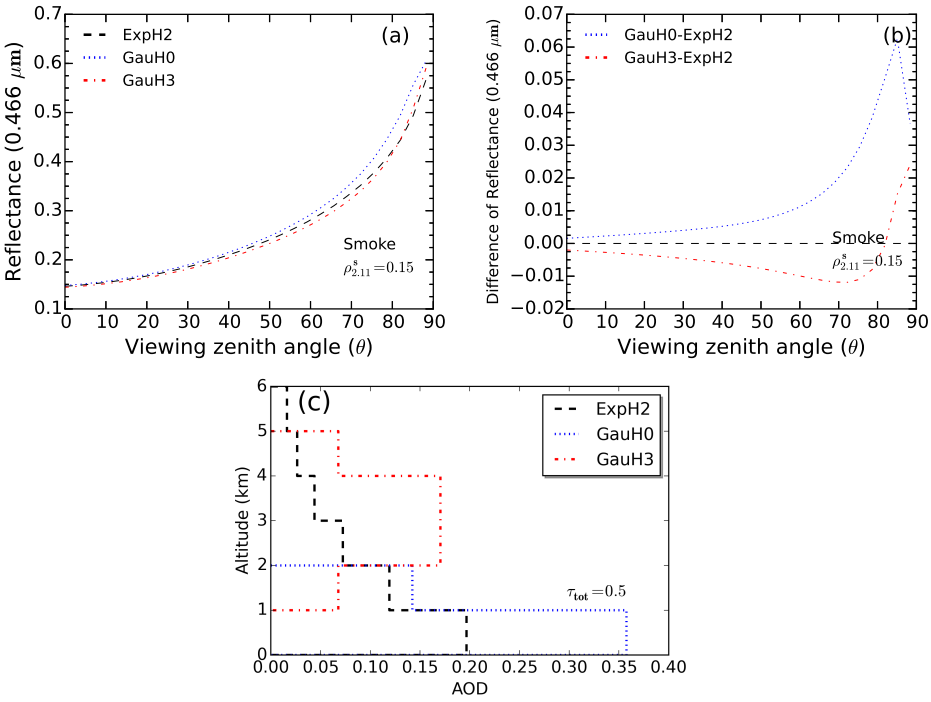

Figure 4.3: The TOA reflectance at 0.466 μm with exponential and Gaussian distributions. All the Gaussian distributions have the same geometrical thickness σ = 1 km and vertical resolution (1 km). "GauHx" means that Gaussian distribution with the mean height of x km. "ExpH2" indicates the exponential function with the scale height of 2. Figure (a) shows the TOA reflectance as a function of viewing zenith angle. Figure (b) shows the difference of the TOA reflectance (e.g., "GauH0-ExpH2"), where the dashed line means zero difference. Figure (c) presents the discrete distributions. Other symbols are similar to Figure 4.2.

To further clarify the relationship between the layer mean height and the TOA reflectance, the Gaussian distribution was selected for the aerosol layer where both the geometrical thickness σ and the vertical resolution of the layer are fixed at 1 km. Taking into account that the layer may climb up to higher altitude such as the dust layers that can reach 3 to 6 km in North Africa and Arabian Peninsula (Liu et al., 2008a; Huang et al., 2015), we extend the mean height to a wider range (e.g., 0 - 10 km) for analysis.

Figure 4.4 presents the TOA reflectance with the Gaussian distributions where the

smoke model is used. With a given geometrical viewing, the TOA reflectance decreases quasi-linearly with increasing altitude of the aerosol layer. This is due to that more isotropic scattering reflected by the Rayleigh layer is attenuated by the aerosol layer.

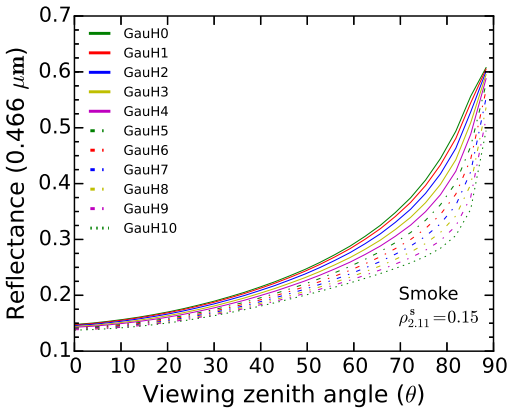

Figure 4.4: The TOA reflectance at 0.466 μm with different mean height (0 − 10 km, GauH0 → GauH10 in Table 4.1). Other symbols are similar to Figure 4.3.

In summary, the TOA reflectance is highly sensitive to the mean height of the aerosol layer, and nearly insensitive to the layer shape. Further, with the increase of the mean height, the TOA reflectance presents a linearly decreasing trend.

4.2.2. The sensitivity of the AOD retrieval to aerosol vertical distribution

Experiment set up

Wu et al. (2016b) demonstrated that the AOD retrieval is affected by different aerosol vertical profiles. Nevertheless, the dependence of the retrieval on the layer mean height was not fully evaluated and needs to be further clarified for our study. To address this, we designed a synthetic experiment in which the TOA reflectance was simulated with Gaussian distributions using off-line LUTs. Four mean heights (0, 3, 6, and 9 km) were set for the distribution (labeled as GauH0, GauH3, GauH6, and GauH9). The MODIS C6_DT algorithm over land (procedure A) is used in this experiment.

Likewise chapter 3 (section 3.3.1), the experiment is also extensively evaluated with aerosol properties and the observation and illumination geometries, as well as the evaluation of the AOD retrieval errors.

Experiment results

Figure 4.5 presents the AOD errors with the four simulations (GauH0, GauH3, GauH6, and GauH9), where the ExpH2 LUT is used in the retrieval procedure. The result with smoke mixtures is shown in the figure, whereas the results with other mixtures are not given due to their generally small errors ($\delta(\tau) < 10\%$). The AOD errors are highly dependent on the mean height. Specifically, the simulation with a low aerosol layer (GauH0) gives an overestimation of the retrieved AOD. By contrast, the simulation with a high

layer (GauH3, GauH6, and GauH9) cause an underestimation. In addition, the underestimation becomes even larger when a higher layer (e.g, GauH6 and GauH9) is used in the simulation. Furthermore, the error increases with increasing AOD. With AOD ≤ 2.0, the errors are limited to 5-20% , whereas the errors increase by > 10% when AOD ≥ 3.0. With the increase of aerosol loading, the errors with dust model ($\eta = 0$) do not steadily increase as with other pure fine models. This points to possible issues with the scattering phase function of the dust model.

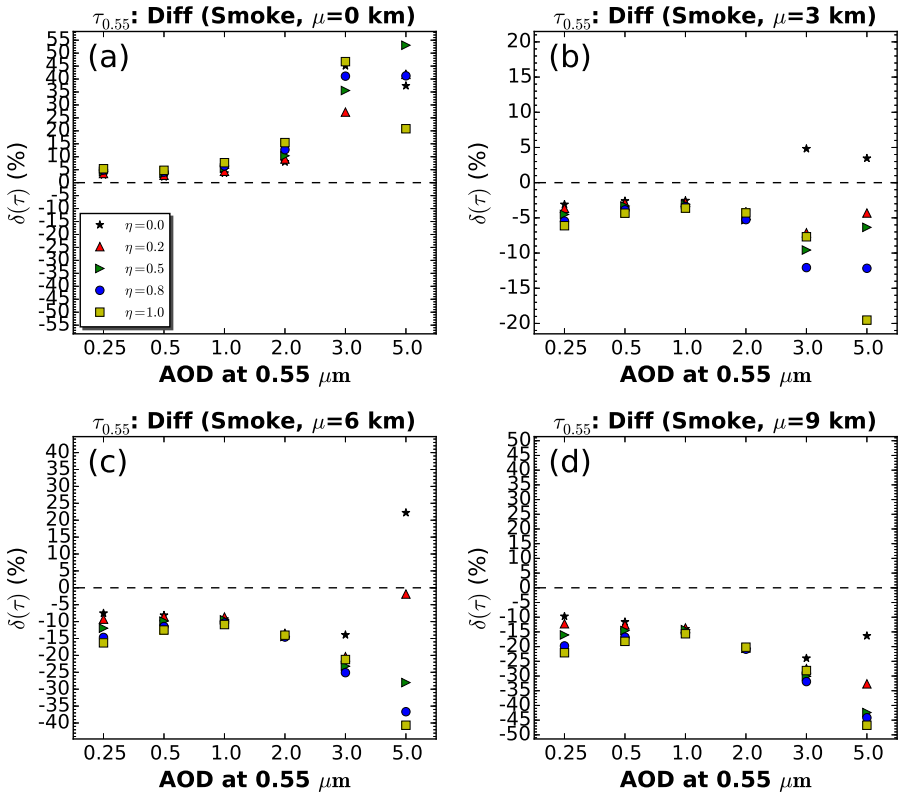

Figure 4.5: The errors $\delta(\tau)$ of AOD retrievals with different vertical distributions (a - d: μ = 0, 3, 6, and 9 km). Smoke model is used in the experiment. The mean differences $\delta(\tau)$ are calculated by averaging over 880 geometrical combinations, shown as a function of aerosol loadings and fine ratios.

4.2.3. New AOD retrieval with dynamic aerosol vertical distribution

The experiment suggests that dynamic profile for aerosol layer has a significant impact on the AOD retrieval. To investigate this impact, we developed a new algorithm (Gau_DT) by parameterizing the profile into the retrieval. In this algorithm, the LUT is precalculated with a known vertical profile which is simply described as the Gaussian distribution, with the mean height μ as single variable. The geometrical thickness σ and the vertical resolution are fixed at 1 km. To avoid too many LUTs that would require

huge data storage, 3 basic LUTs were prepared with the layer mean height of 0, 3 and 6 km. The LUTs will be further linearly interpolated or extrapolated to the measured mean height in the retrieval. The measurements are extracted from MODIS level 2 product "Mean_Reflectance_Land" (MYD04_L2), which is obtained through gas correction, cloud and water mask and dark target filtering, re-sampled to 10 × 10 km. As for the mean height, we derived this parameter from CALPSO data. More details on CALPSO data are introduced in the next section, as well as the derivation of the mean height.

4.3. CALIPSO VFM Data

We use the VFM data for the detection of the aerosol layer. Figure 4.6 (a) shows a sample plot of total attenuated backscatter at 532 nm observed during daytime using CALIPSO Level 1 data (dataset: "Total_Attenuated_Backscatter_532"). Figure 4.6 (b) presents vertical feature mask observed at the same time and place, using CALIPSO Level 2 VFM data (dataset: "Feature_Classification_Flags"). In this figure, several target types are determined such as clear air, cloud, aerosol and the surface. Combining Figure 4.6 (a) and (b), it is apparent that the most attenuated backscatter is determined as "cloud" (white color in Figure 4.6 (a) and cyan color in (b)), whereas the moderately attenuated backscatter is determined as aerosol (orange color in Figure 4.6 (b)). Note that there is no signal (black color) below the cloud in Figure 4.6 (b).

Details on the derivation of the aerosol height are introduced as below.

4.3.1. The derivation of aerosol vertical distribution (layer mean height)

The mean height of aerosol layer is derived from Level 2 VFM product in two steps (also see Figure 4.7):

- Step 1: in this step, clear air and aerosol layers are to be determined within a window of 0.5 × 10 km (16 × 30 pixels in VFM data). An extraction method was developed for these layers. This method searches and counts aerosol pixels from the top to the bottom of the vertical column. The window that has more than 50% aerosol pixels will be assigned as "aerosol". If it is not the case, we count clear air pixels. The window that has more than 50% clear air pixels will be assigned as "clear air", otherwise, it is given as "blank". In the search process, aerosol pixels are always detected in the column first, then clear air pixels. If no aerosol pixel is found, then the whole column is assigned as "blank".

- Step 2: aerosol layer boundary and the layer mean height are extracted. In each vertical column with a width of 10 km, the top and base height of each aerosol layer are detected. The layer mean height is calculated by averaging the height of the top and base. Aerosol vertical profile is assumed to be a single layer.

Figure 4.6 (c) illustrates the vertical feature mask with Step 1. Four types are given in the figure. They are air/cloud, clear air, aerosol and others (could be surface, air, cloud or mixture of them). The undetermined area (white color) indicates that there is no aerosol found in the column. Figure 4.6 (d) shows the boundary and mean height of the aerosol layer after Step 2.

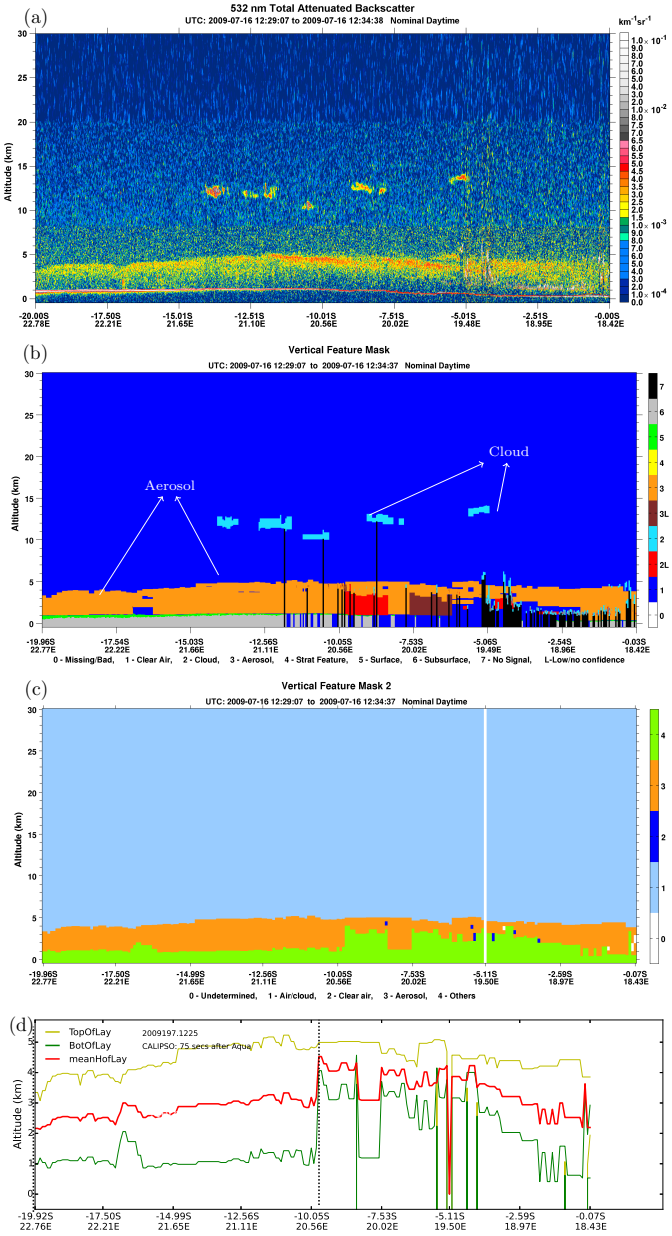

Figure 4.6: Atmosphere vertical profile measured by CALIPSO. The data is captured on 16th July, 2009 during daytime. It is shown as Figure (a-d), based on the different process Levels. Figure (a) shows the total attenuated backscatter at 532 nm (data from CALIPSO Level 1). Figure (b) presents the vertical feature mask (data from CALIPSO Level 2 Vertical Feature Mask), where several types are classified such as Cloud, Clear Air and Aerosol etc. Figure (c) gives the result of types (aerosol, cloud and clear air) after the aggregation of CALIPSO Level 2 data. Figure (d) illustrates the aerosol layer boundary (top: yellow, bottom: green) and mean height (thick red), respectively. The two dashed lines (black) in (d) indicate the region in Figure 4.9.

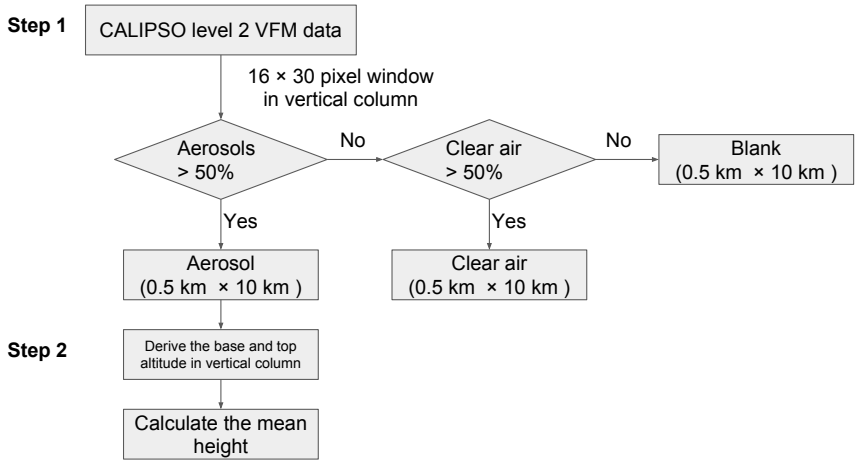

Figure 4.7: Flowchart for the derivation of aerosol layer mean height using CALIPSO Level 2 (VFM) data. Aerosol and clear pixels are detected and determined in the window of 16 × 30 pixels when the window moves from the top to the bottom of the vertical column. Aerosol pixels are firstly detected. If the window has more than 50% aerosol pixels, it will be assigned as "aerosol". If not, we count clear air pixels. The window that has more than 50% clear air pixels will be assigned as "clear air", otherwise, it will be assigned as "blank". The detected aerosols (0.5 × 10 km) are further used to derive the base and top altitude, resulting in the mean height. More details are given in the text.

Due to the nadir view only of CALIPSO, the derived height has a narrow swath (30 m). To solve the mismatch between MODIS (10 km) and aerosol height data, we resampled the height data into seasonal (5 × 5 degrees) and real-time dataset (10 × 10 km), respectively. The seasonal dataset is obtained by averaging the height data over a season, whereas the real-time dataset is obtained by assuming the height to be homogeneous across the CALIPSO track and extending it to the whole MODIS swath (2030 km). These two datasets are used for the new algorithm. We note that the assumptions of a single layer and horizontal homogeneity for the aerosol profile can hold well for the cases of a long range pollution of dust or smoke since the aerosol layers tend to be homogeneous (Lee et al., 2015). It may not hold well for the cases that have complicated atmospheric conditions. In addition, zero values for the layer height could happen under a clear sky. For this case, we use the mean height of ExpH2 (1.4 km) instead.

4.4. Results and Discussions

Gau_DT was applied to smoke and dust regions. Cases of light moderately-absorbing and non-absorbing aerosols are not discussed here. This is because for these cases the impact can be easily covered by some other potential errors that could arise from instrument measurement uncertainty (e.g., calibration and random errors in channels) and from the inappropriate assumptions on the aerosol model and the relationship of surface reflectances in visible versus short wave infrared. Through a sensitivity analysis, Levy et al. (2007b) demonstrated that 3-5% errors (Mean Square Error) of the retrieval could be accounted by the errors of MODIS measurements or the spectral surface

reflectance (presented in Table 4b in Levy et al. (2007b)), and would be even larger by combining these two error sources. These errors are comparable to the ones due to the aerosol dynamic vertical distribution when moderately-absorbing (generic) and non-absorbing (urbanIndustrial) aerosols are observed especially under light aerosol loading (e.g., AOD).

4.4.1. AOD validation with AERONET data

The new AOD retrievals were validated using AERONET AOD data. Following the method introduced in Petrenko et al. (2012), MODIS AOD pixels within a circle of 25 km centered at a ground site were selected and averaged where the maximum pixels is limited to 25. AERONET measurements were averaged over a ±30 minutes interval centered on the Aqua satellite overpass time. A valid collocation requires that at least 3 MODIS pixels and 2 AERONET measurements are present within a selected spatial-temporal window (Levy et al., 2013b). For the comparison with Gau_DT, C6_DT AOD was also added. The AOD bias in the DT algorithms is evaluated as:

$$\text{Bias} = (\text{DT} - \text{AERONET}) \;/\; \text{AERONET} \tag{4.2}$$

Three years (2008 - 2009) of MODIS data were collected over Middle Asia (dust) and Middle Africa (smoke) areas. The related information for the areas is given in Table 4.2. To clearly show the difference between Gau_DT and C6_DT AOD, we chose the data with the layer height > 2 km. There are 437 and 470 cases collected with seasonal and real-time height dataset, respectively.

Figure 4.8 shows scatter plots of MODIS AOD versus AERONET data. There are some improvements on AOD retrieval bias. From Figure 4.8 (a-b), we can see that the bias was reduced in Gau_DT. The reductions are 3% (-3.3% to -0.3%) and 4% (-5.6% to -1.6%) with seasonal height dataset and with real-time dataset, respectively. The improvement becomes more significant for higher layers (height > 2.5 km), as shown in Figure 4.8 (c). We found that the bias was reduced by 5.2% (from -6.2% to -1%) with the real-time dataset. This demonstrates that Gau_DT can substantially reduce the negative bias due to the elevated aerosol layers. Nevertheless, the AOD uncertainty in Gau_DT still remains since there are trivial improvements in the correlation coefficient R. This uncertainty is mainly attributed to the other potential errors, i.e., errors in the spectral surface reflectance. Note that the results with the seasonal dataset are not shown due to too few cases with height > 2.5 km.

Region	Period	Geoinformation
Middle Asia (Dust)	2008 – 2010	15° – 30°N, 70° – 93°E
Middle Africa (Smoke)	2008 – 2010	20°S – 0°, 10° – 40°E

Table 4.2: Information of smoke and dust regions.

To get a better insight, two concrete cases of dust and smoke were selected which are located at Mongu (Middle Africa) and Pantnagar (Middle Asia), respectively. The results are shown with the real-time height dataset.

Figure 4.9 shows C6_DT and Gau_DT AOD over Middle Africa area, obtained on 16 July, 2009. The CALIPSO track is across the MODIS image from the bottom to the top,

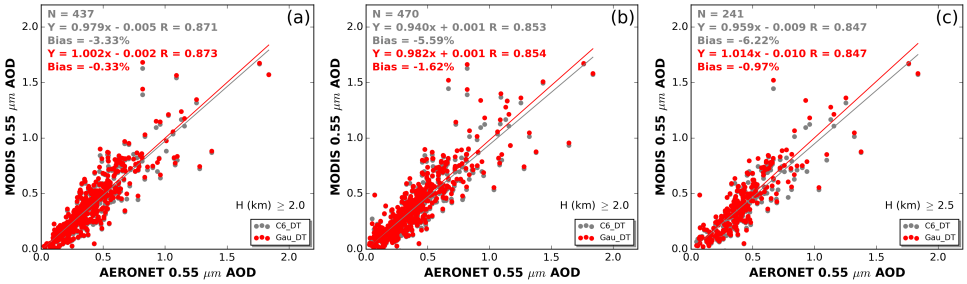

Figure 4.8: Scatter plot of MODIS AOD versus AERONET data. MODIS AOD of Gau_DT (red) and C6_DT (gray) present as a function of AERONET data. Figure (a) is the result with seasonal aerosol height (5 × 5 degrees). Figures (b-c) are the results with real-time aerosol height (10 × 10 km, 75 s delay after MODIS measurements). The symbol of "H" is the mean height of aerosol layers retrieved from CALIPSO measurements.

denoted as a red line in Figure 4.9 (d). The mean height of aerosol layers is given as red line in Figure 4.6 (d). In Figure 4.9 (a), there are a lot of smoke plumes caused by fires where most plumes are originated from the eastern part (24° - 32°E), and raised up to a higher level. The climbed-up layers present much higher altitude (height > 2.5 km, see Figure 4.6) than the assumption (height = 1.4 km) in C6_DT. As result, we can see that for the eastern part (Figure 4.9 (d)) Gau_DT AOD can differ by > 5% (> 0.02) with C6_DT. Further, the new retrieval was found to be less biased by 5% than C6_DT against Mongu measurements. Nevertheless, for the western area, Gau_DT and C6_DT AOD do no differ too much. This is mainly because the impact due to the elevated layers is small under the oblique viewing and light aerosol loading (AOD < 0.1).

Figure 4.10 presents the MODIS DT AOD with the dust event, acquired on 17 July 2008. In Figure 4.10 (b-c), there is no AOD retrieval over large bare soil areas since the DT algorithms cannot be applied over bright surface areas. The retrievals become available over North India (dark surface area). Dust particles were well detected by both the DT algorithms (fine ratios η retrieved as 0). The dusts were from the Middle East (e.g., Iran or Sahara desert) by long distance transport, with the layer mean height ranging from 2.8 to 3.5 km (see Figure 4.11). Regarding this highly elevated layer, Gau_DT AOD presents significantly larger (5% - 10%: 0.02 - 0.04) value than C6_DT. In other words, this means that in this case C6_DT can always give a negative retrieval bias by up to 10%. Particularly, the new retrievals around Pantnagar increased by 5% (0.025) compared to C6_DT and are closer to the ground truth.

4.5. Conclusion

The MODIS C6_DT algorithms can successfully retrieve AOD by using a fixed vertical profile for the aerosol layer over the globe. However, the assumption of the static vertical distribution may lead to some errors in the AOD retrieval especially for elevated aerosol layers.

In this study, a new algorithm was developed that is based on the MODIS C6_DT algorithm to account for the impact of dynamic aerosol profile in the AOD retrieval, by using MODIS and CALIPSO measurements. The relationship between the TOA reflectance

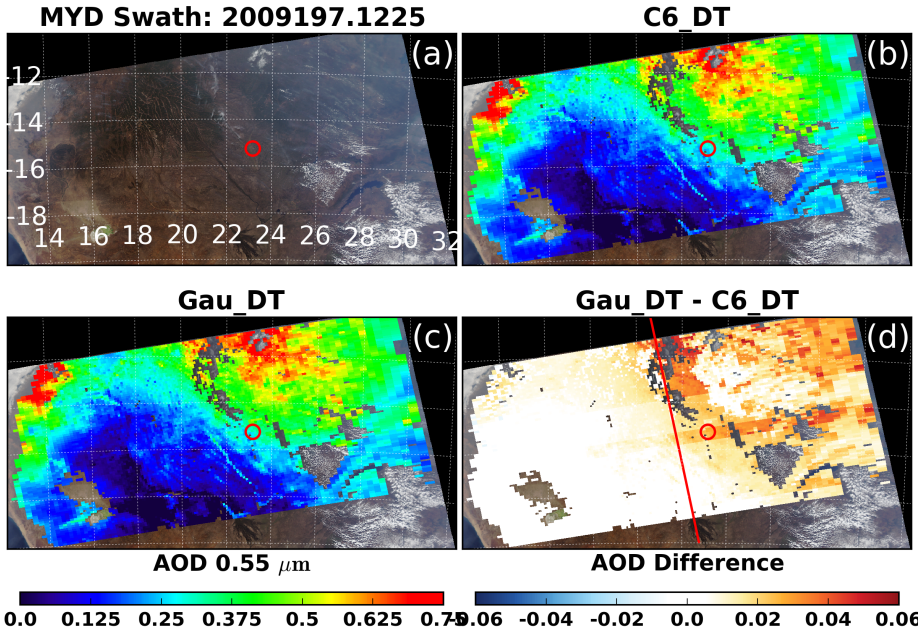

Figure 4.9: The smoke event over Middle Africa. Figures (a-d) are: MODIS true color image (by the combination of channel 4, 3, and 2), C6_DT and Gau_DT AOD, and their difference overlap the MODIS image, respectively. The CALIPSO track (red line) is plotted in Figure (d). Small red circles in Figure (a-d) indicate the location of AERONET site Mongu (15.25°S, 23.15°E).

and aerosol vertical profile was extensively investigated as well as the sensitivity of the AOD retrieval to the aerosol vertical distribution. We found that in the aerosol vertical profile the layer mean height is the major variable that influences the TOA reflectance. Specifically, the TOA reflectance linearly decreases with increasing mean height. This leads to a high sensitivity of AOD retrieval to different profiles especially when smoke or dust aerosols are observed. Normally, the use of the fixed profile (ExpH2 in C6_DT) can cause a 5% to 20% error in the retrieval for smoke or dust cases owing to the dynamic profile. To reduce these errors, the profile was parameterized into the algorithm where the profile was assumed to be a Gaussian function with the mean height as single variable. Three basic LUTs are precalculated and linearly interpolated to the measured mean height in the retrieval process.

The new algorithm was applied to smoke and dust regions with three years (2008-2010) of data. The mean height of the aerosol layer was derived from CALIPSO VFM data and re-sampled as seasonal (5 × 5 degrees) and real-time dataset (10 × 10 km), respectively. Aerosol vertical profiles are assumed to be a single layer and homogeneous at spatial, i.e., 5 × 5 degrees. To show the impact of the vertical profile on the retrieval, the new AOD are compared with C6_DT and validated against AERONET data.

The results show that elevated aerosol layers have a strong influence on the MODIS AOD retrieval. Generally, the elevated layers can negatively bias the retrieval by 3 - 5% in C6_DT. The biases are reduced to within -1.6% by the new algorithm. This becomes

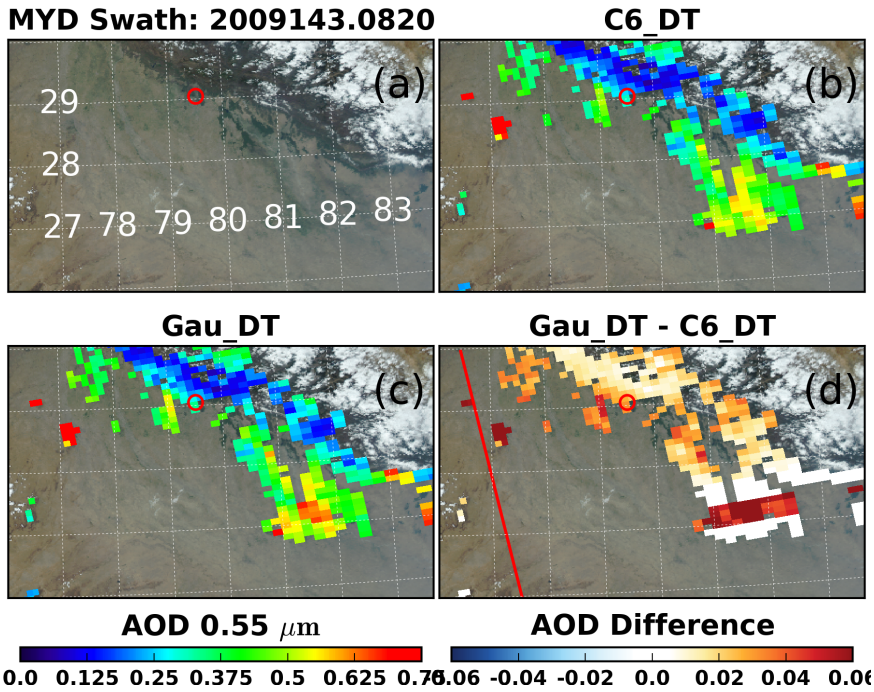

Figure 4.10: The dust event over Middle Asia. Figure (a-d) illustrate similar images as in Figure 4.9. Small red circles in Figure (a-d) indicate the location of AERONET site Pantnagar (29.05°N, 79.52°E).

more significant with the increase of layer height (e.g., > 2.5 km). Two specific cases were shown over AERONET site Mongu (smoke) and Pantnagar (dust).

For the elevated layers such that high altitude (3 - 6 km) dusts frequently occurs over the "dust belt" (Sahara desert, Middle East and Taklamakan desert) during summer (Liu et al., 2008a), the new AOD retrieval can improve the estimate of the direct radiative effect by > 5% when aerosol loading is << 1.0 (Anderson et al., 2005; Levy, 2007). Nevertheless, we note that the AOD uncertainty remains due to the errors in spectral surface reflectance. These are subjects for further study.

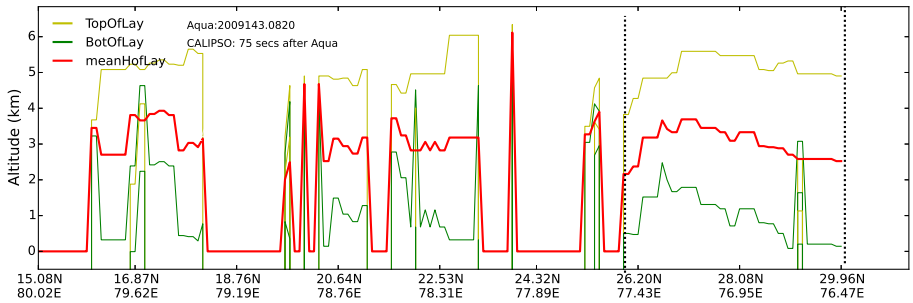

Figure 4.11: Dust layer information derived from CALIPSO. The data is collected on 23th May, 2009 during daytime. Symbols are similar to that in Figure 4.6 (d). The two dashed lines indicate the region in Figure 4.10.

5

AOD retrieval considering surface BRDF effects

Based on: Wu, Y., de Graaf, M., and Menenti, M. (2017). MODIS Aerosol Optical Depth retrieval over land considering surface BRDF effects. *manuscript*.

5.1. Introduction

In the previous chapter, we investigated the effect of aerosol properties on the AOD retrieval with the MODIS algorithm. However, this algorithm still uses a simple RT model of TOA reflectance, by assuming isotropic reflection at the surface. A high quality AOD retrieval requires us accurately interpret satellite observations by taking account of the anisotropic reflection of the surface and its contribution to the observations since there are no actual surfaces with a null reflectance (full absorption). For instance, the surface BRF can vary by a factor of up to 5 or more across the range of illumination and observation angles. Moreover, the contributions of surface direct and diffuse reflection to the satellite measurements can diverge and need to be treated separately, while they are viewed to be identical in the simple RT model with a Lambertian surface. These contributions not only depend on the surface reflection itself, but also depend on the radiation interaction between the surface and the atmosphere. At light aerosol loading, the radiation interaction is small and the surface direct reflection has a strong impact on the measurements since the solar radiation is lightly scattered by the atmosphere. At larger aerosol loading but not extremely large, the interaction due to the surface diffuse reflection becomes significant and is an important contribution to the observations. Simply applying a Lambertian surface model to these cases, the surface contribution to the TOA reflectance is not well estimated and would result in significant errors in the retrieval.

In this Chapter, we present an improvement in the MODIS AOD DT algorithm by coupling the surface BRDF (called BRF_DT) with radiative transfer in the atmosphere. Section 5.2 introduces the data used in the algorithm. The BRF_DT algorithm is presented in section 5.3, including the simulation of the TOA reflectance coupled with a non-Lambertian surface using a LookUp Table approach. The parameterization of the surface reflectance is introduced as well as the retrieval errors due to its uncertainty. In addition, a protocol to assess the quality of the retrieval with the algorithm C6_DT is defined and applied to the new algorithm. Section 5.4 presents the comparison between BRF_DT and C6_DT AOD and the validation with AERONET AOD. Conclusions are drawn in section 5.5.

5.2. Data

5.2.1. MODIS measurements

To be consistent with data preprocessing in C6_DT, BRF_DT directly makes use of the dataset “Mean_Reflectance_Land” in the MYD04_L2 product as input data.

5.2.2. MODIS BRDF/albedo products

The MODIS BRDF/albedo products (MCD43A1) (Lucht et al., 2000; Schaaf et al., 2002), including the surface BRF, black-sky and white-sky albedos, is created using the 8-day (Terra and Aqua) surface reflectance product (MOD09) that has been atmospherically corrected by the internal aerosol retrieval algorithm (Vermote et al., 1997; Vermote and Kotchenova, 2008). The semi-empirical BRDF kernel model (RossThick-LiSparse (LSRT) model) that is made up of Lambertian K_{iso}, geometric-optical K_{geo} and volume scattering kernels K_{sca} was applied to reconstruct the surface BRDF/albedo by a linear combination of the kernels.

Note that each BRDF kernel is predefined and has its own assumption on the background surface. Specifically, the volume scattering kernel K_{vol} assumes "a dense leaf canopy", whereas the geometrical scattering kernel K_{geo} assumes " a sparse ensemble of surface objects casting shadows on the background" (Lucht et al., 2000). These kernels are given as a function of an illumination and viewing angle and thus can be precomputed and stored.

Figures 5.1 and 5.2 show the BRDF kernels and shape as functions of viewing zenith angle (under solar principle and cross-principle plane). The positive (negative) viewing zenith angle indicates the backward (forward) direction. Specifically, the shape of BRDF using the observed model parameters is given in Figure 3 (right panel). The BRDF shows a large value at viewing zenith angle around 45° where solar zenith angle = 45°. Obviously, if there is completely back surface, the aerosol retrieval is definitely not related to the surface BRDF since there is no contribution from the surface to the observation.

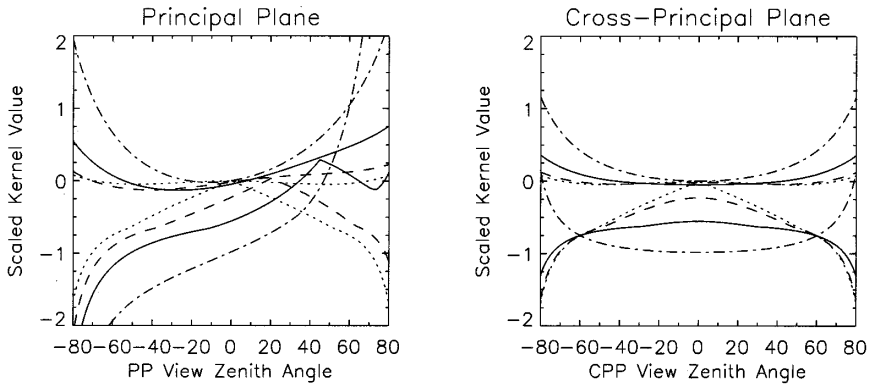

Figure 5.1: Principal plane and cross-principle solar plane plots of the RossThick (upper curves) and LiSparse-R (lower curves) BRDF model kernel values (arbitrary units; the LiSparse-R kernel values were divided by 2 for better plotting). The sun is located at positive zenith angles of 0 (dotted lines), 20 (dashed lines), 45 (solid lines), and 70 (dashed-dotted line) solar zenith angle. The parameter $h = b$ of the LiSparse-R kernel was set to 2.0 and the parameter $b = r$ to 1.0. Figure is copied from Lucht et al. (2000).

Note that black-sky and white-sky albedos are virtual concepts and they imply some assumptions on the atmosphere. The black-sky albedo assumes a totally transparent atmosphere where a diffuse flux is absent, whereas the white-sky albedo assumes a totally homogeneous atmosphere where a direct flux is absent. The black-sky albedo is a function of solar zenith angle, whereas the white-sky albedo is independent on the illumination and viewing angle. The kernels of black-sky and white-sky albedos are the integrals of the BRDF model kernels (see equation 25 and 26 in Lucht et al. (2000)) and also can be precomputed. By minimizing the difference between the atmospherically corrected reflectance and the BRDF kernel model, the model parameters are retrieved and used to generate the surface BRDF/albedo with the calculated kernels.

The BRDF/albedo product has a high accuracy with errors of < 5% and < 10% with the high and low quality, respectively (validation results see http://landval.gsfc.nasa.gov/, accessed in August 2016), with the spatial resolution of 500 m. The studies in Taberner

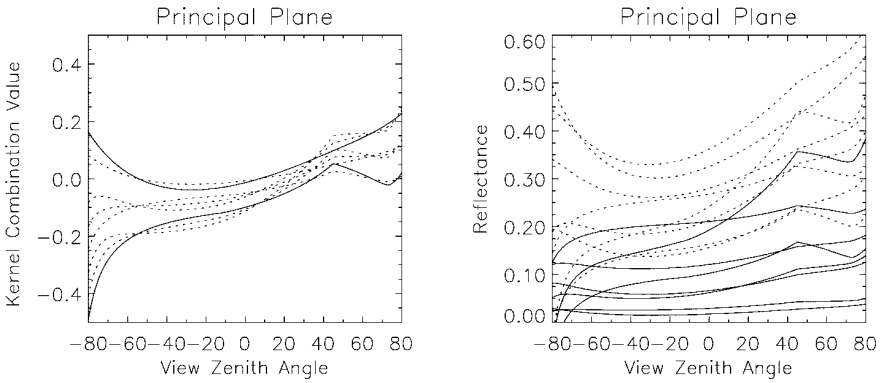

Figure 5.2: BRDF shapes which the Ross-Li BRDF model acquires under natural conditions on the principal solar plane for a solar zenith angle of 45 . Left panel: shape of the BRDF using typical values for the model parameters. The two solid lines represent the maximal volume scattering and geometric-optical scattering found for 18 field-observed BRDF's representing a wide range of barren and vegetated cover types in the red and near-infrared wavebands. The dotted lines are intermediate cases where the parameters take on either their respective maximal value, half of it, or are zero in all possible combinations. Right panel: shape of the BRDF using observed model parameters in the red (solid lines) and near-infrared (dotted lines) wavebands. The datasets used represent sparse brushland, dense broadleaf forest, dense barren trees on snow, dense needleleaf forest, sparse grass, dense grassland, and barren soil (data collected by numerous investigators). Figure is copied from Lucht et al. (2000).

et al. (2010) and Pinty et al. (2010) have shown that on regional and global scales the white-sky albedo product well agrees with similar products generated based on the Multiangle Imaging Spectroradiometer (MISR) land surface BRF parameter. This product is not accurate when the land surface conditions change rapidly over a short period or when large solar zenith angle (> 70°) applies to the observation. This product is used to constrain the surface reflectance in the AOD retrieval. There is some circularity in the retrieval using such a product of atmospheric correction. But the aerosol retrieval in the MCD43A1 product is independently done where the retrieval depends on its own aerosol climatology (aerosol model and loading). Any uncertainty in MCD43A1 product due to the errors in the atmospheric correction can propagate into the BRF_DT algorithm. But it leads not much error in the retrieval. The sensitivity study (in section 5.3.3) shows that the retrieval errors due to the BRDF/albedo uncertainty are smaller than 6.5%. This is mainly because the important factor surface BRF is also retrieved other than using MCD431 product. More details about the use of the product in the surface reflectance parameterization are given in the next sections, as well as the effect of the product uncertainty in the AOD retrieval.

5.3. BRF_DT AOD algorithm

Based on the MODIS C6_DT algorithm (Levy et al., 2013b), the BRF_DT algorithm is newly developed to improve AOD retrievals. It takes into account the surface BRDF effects in the retrieval, which differs from C6_DT where a Lambertian surface is assumed.

To reduce the computational cost of the AOD retrieval, a LUT approach was applied in the new algorithm, to couple the TOA reflectance with the non-Lambertian surface as well as the parameterization of the surface reflectance in the retrieval.

5.3.1. Coupling the TOA reflectance with a non-Lambertian surface

High quality AOD retrieval requires accurate estimates of the contribution of anisotropic or non-Lambertian surface to the TOA radiance. Coupling the TOA radiance with surface BRDF effects was originally proposed by Li et al. (1996), and further improved and validated by Qin et al. (2001) (see equation 5.1). It has a high accuracy (0.7% on average) over several surface cover types (Qin et al., 2001), and is applied in this study. Here, we briefly introduce the TOA radiance by considering non-Lambertian surface, and the retrieval algorithm.

According to the four-stream theory (Verhoef, 1985), the radiation field can be divided into directional (d), and hemispheric part (h) indexed by the subscripts "d" and "h". Since we have an incident and reflected radiation, we get four combinations of these subscripts: "dd", "dh", "hd" and "hh".

A sketch diagram is shown of the TOA radiance observed by a satellite radiometer in Figure 5.3. In this figure, we have a parallel solar beam F_0 with a zenith angle θ_s as incident radiation at TOA. This radiation is scattered and absorbed by the atmosphere before reaching the bottom boundary of the atmosphere. Part of the scattered radiation can get into the view of the sensor, called "path reflected radiance" ρ^a. A fraction of the scattered radiation propagates forward, called downward radiance including hemispherical and directional transmitted radiance $t_{dd}(i)$ and $t_{dh}(i)$, and interacts with the underlying surface. Regarding the underlying surface as a non-Lambertian, the anisotropic reflection of the surface is simply described by four reflectance properties: hemispherical-directional ① (R_{hd}), bihemispherical ② (R_{hh}), bidirectional ③ (R_{dd}) and directional-hemispherical reflection/reflectance ④ (R_{dh}), respectively, see Figure 5.3. The downward radiation undergoes complicated reflections at the surface and scattering in the atmosphere.

The directional flux reflected by the surface could be from the downward transmitted radiance after ① or ③, whereas the corresponding hemispherical component is from the downward transmitted radiance and determined by ② or ④. Here we neglect the multiple reflections between the lower atmosphere and the surface (e.g., strong specular reflection) for the directional flux. The atmosphere backscattering ratio is denoted as s. Finally, there is a directional flux from the lower atmosphere, through the directional transmission $t_{dd}(v)$ into the view of the sensor. Similarly, the sensor receives another directional flux which is from the diffuse flux undergoing the hemispherical-directional transmission $t_{hd}(v)$. Therefore, the TOA reflectance captured by the sensor (radiance converted to reflectance by normalization) is composed of two parts: the atmospheric reflectance (path reflectance) and the reflectance contributed by the interaction of the surface and the atmosphere, which is written as follows (a complete derivation is given Appendix B):

$$\rho^*(i,v) \quad = \quad \rho^a(i,v) + \frac{\mathbf{T}(i)\mathbf{R}(i,v)\mathbf{T}(v) - t_{dd}(i)\,|\mathbf{R}(i,v)|\,t_{dd}(v)s}{1 - R_{hh}s}, \tag{5.1}$$

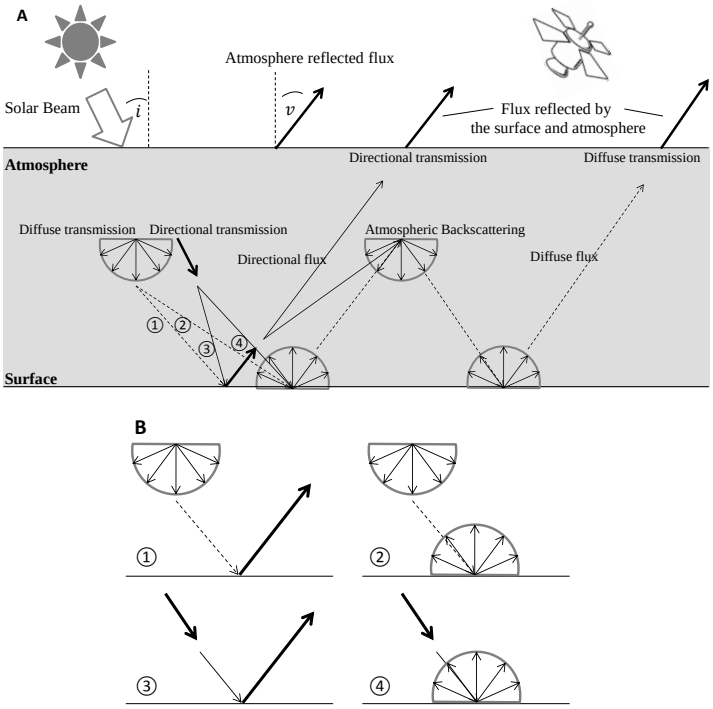

Figure 5.3: The TOA flux observed by the satellite considering the surface BRDF effects. The surface BRDF is simply described as 4 elements: hemispherical-directional ① (R_{hd}), hemispherical-hemispherical ② (R_{hh}), directional-directional ③ (R_{dd}) and directional-hemispherical reflectance/reflection ④ (R_{dh}), also shown in Figure B. Parameters in the radiation-field are solar beam F_0, solar beam scattered and attenuated by the atmosphere at the bottom layer $t_{dh}(i)$ and $t_{dd}(i)$, respectively, (or called the downward diffuse/directional transmitted radiance), the radiance reflected by the atmosphere ρ^a, the directional/diffuse flux from the bottom atmosphere through directional transmission $t_{dd}(v)/t_{hd}(v)$, atmospheric backscattering ratio s. More details are explained in the text.

where,

$$\mathbf{R}(i,v) = \begin{bmatrix} R_{dd} & R_{dh} \\ R_{hd} & R_{hh} \end{bmatrix}$$
$$\mathbf{T}(i) = \begin{bmatrix} t_{dd}(i) & t_{dh}(i) \end{bmatrix}$$
$$\mathbf{T}(v) = \begin{bmatrix} t_{dd}(v) \\ t_{hd}(v) \end{bmatrix} \tag{5.2}$$

For convenience, the dependence of each term on wavelength λ is not explicitly shown here and in subsequent equations. The second term on the right hand side of equation 5.1 shows the contribution of the surface to TOA reflectance. $\mathbf{R}$ is the surface reflectance matrix, which is made up of four components: directional-directional R_{dd}, directional-hemispherical R_{dh}, hemispherical-directional R_{hd} and bidirectional-hemispherical surface reflectance R_{hh}, its determinant is $|\mathbf{R}| = R_{dd}R_{hh} - R_{dh}R_{hd}$. Then

we have the atmospheric transmittance matrix variables $\mathbf{T}(i)$ ($\mathbf{T}(v)$) in equation 5.2 and the correspoinding scalar variables in equation 5.3 and 5.4.

$$T(i) = t_{dd}(i) + t_{dh}(i) \tag{5.3}$$
$$T(v) = t_{dd}(v) + t_{hd}(v) \tag{5.4}$$

where

$$t_{dd} = t_{dd}(\mu, \tau_a) = \exp(-\tau_a/\mu) \tag{5.5}$$
$$\mu = \cos\theta \tag{5.6}$$

τ_a is the total optical depth of the atmosphere, which equals to the sum of AOD and Rayleigh Optical Depth.

We note that equation 5.1 can be approximately or even completely identical to equation 2.8 under certain conditions. Two cases are discussed below.

- Case One: a Lambertian surface, where the four components in $\mathbf{R}$ are equal to ρ^s, makes equation 5.1 to be identical to equation 2.8.

- Case Two: low spectral AOD atmosphere, where the directional incident radiation is less scattered by the atmosphere, leads to a small or nearly zero diffuse radiation. Specifically, we have nearly zero values for the diffuse transmittance $t_{dh}(i)$ and $t_{hd}(v)$, and atmospheric backscattering ratio s. Therefore the surface contribution to the TOA reflectance can be approximated as $t_{dd}(i)R_{dd}t_{dd}(v)$ for both equation 2.8 and 5.1, thus these two equations are approximately identical. Theoretically, Case Two will be used for supporting our assumptions in the new algorithm discussed next.

Nevertheless, the real case that neither has a Lambertian surface nor low spectral AOD atmosphere, requires us to consider the contribution of diffuse-radiation to the reflectance at TOA with equation 5.1.

5.3.2. Parameterization of the surface reflectance in the AOD retrieval

Three parameters, AOD, fine mode aerosol ratio η and surface BRF R_{dd}, are retrieved in the BRF_DT algorithm by fitting the simulated TOA reflectance (using equation 5.1 and 2.10) to MODIS measurements at three wavelengths (0.466, 0.644 and 2.12 μm).

In the new algorithm, three more unknowns (R_{dh}, R_{hd} and R_{hh}) are present in the retrieval compared to C6_DT, which can be determined using the MODIS BRDF/albedo product. Specifically, R_{hh} and R_{dh} are directly provided by MODIS BRDF/albedo MCD43A1 white-sky and black-sky albedo. According to the study in Snyder (1998) , we assume that reciprocity law is valid for the reflectance over structured surfaces (e.g., forest canopies and grasslands) as well as over a flat surface. This law allows us to interchange $R_{hd}(i)$ with $R_{dh}(v)$ for any $i = v$. Note that this law does not require the occurrence that the solar zenith angle and viewing zenith angle are equal. Further, a few assumptions and considerations about the spectral surface reflectance apply as follows.

- Assuming that C6 surface reflectance relationship of VISvsSWIR is suitable for the case of surface BRF R_{dd}. Although a Lambertian surface is assumed in the relationship (equation 2.8), we note that the relationship is derived under low AOD (τ at 0.55 μm < 0.2, hereafter we use τ for 0.55 μm) which approximately meets the requirement in Case Two (mentioned above) where the directional incident radiation is less scattered by the atmosphere. Therefore, the relationship applied for surface BRF is reasonable.

- Assuming that the atmosphere is nearly transparent at 2.11 μm, then we have a low spectral AOD atmosphere that matches Case Two (mentioned above). In this case, we have a high similarity between equation 2.8 and 5.1, which means the reflectance at TOA using equation 2.8 would not yield too large error. Some evidence supports the assumption. The surface reflectance retrieved at 2.11 μm has a very high accuracy (98.62% overall falls in "good" observation $0.005 + 0.05\rho^s$) when assuming Lambertian surface (Vermote and Kotchenova, 2008). By comparing the Lambertian surface reflectance and surface BRF R_{dd}, it was found that the difference in the surface reflectance becomes significant at shorter wavelengths (Wang et al., 2010). Alternatively, it demonstrates that the surface reflectance at longer wavelength would not differ too much using equation 2.8 and 5.1 after rearrangement. On the other hand, by considering the BRDF effect at 2.11 μm, the AOD retrieval does not improve due to relatively large errors in the BRDF/albedo product MCD43A1. We conclude that the TOA reflectance at 2.11 μm can be approximately calculated using equation 2.8. Note that this assumption may not hold well for a heavy AOD atmosphere since the solar radiation at 2.11 μm can be significant scattered by the thick aerosol layer.

5.3.3. AOD retrieval error caused by BRDF/albedo uncertainty

Owing to the use of BRDF/albedo data in the BRF_DT algorithm, the retrieved AOD may suffer from the uncertainty of these data. To test the effects of the BRDF/albedo uncertainty in the retrieval, we performed a sensitivity study over a typical vegetation area. The surface BRF $R_{dd,2.12}$ is calculated with the BRDF kernel code *brdf_forward* (see website `https://www.umb.edu/spectralmass/terra_aqua_modis/modis_user_tools`), giving a value around 0.15. In this test, we set 10% uncertainty for the BRDF/albedo at two visible bands (0.466 and 0.644 μm). The results show that the errors of the AOD retrieval are < 6.5% due to the BRDF/albedo uncertainty. This demonstrates that the albedo product can be well used for the AOD retrieval in the new algorithm.

5.3.4. Quality assurance of AOD retrievals

Since BRF_DT makes use of the same measured mean reflectance ("Mean_Reflectance_Land") as C6_DT (Levy et al., 2013b), the Quality Assessment (QA) of the retrievals applied in C6_DT is also available for BRF_DT. This is because QA, roughly describing the number of dark target pixels used in the retrieval, is flagged in the mean reflectance. The QA systems with the dark target method proceeds over 20 × 20 pixels box (500 m resolution), which requires the measured 2.12 μm reflectance in the box falling between 0.01 and 0.25. By removing the brightest 50% and the darkest 20% of the measured 0.66 μm

reflectance over the box, a maximum of 120 pixels were selected to calculate the mean reflectance. More than 20, 30 and 50 pixels used out of possible 120 pixels are labeled as QA=1, 2 and 3, respectively. The detailed procedure is described in Levy et al. (2007b) and Levy et al. (2013b). The AOD with QA=0 is not discussed here since multiple factors can reduce QA to 0 such as a large fitting error in the retrieval and the detected thin cirrus pixels, in addition to the few dark target pixels used.

5.4. Results and Discussions

The BRF_DT algorithm was used in three case studies: 2008 and 2010 two years data from Eastern China (20°N - 50°N, 100°E - 125°E) and North America (25°N - 65°N, 135°W - 60°W), and four months (January and July in 2008 and 2010, respectively) for global land areas (see Table 5.1). The AODs with different QAs are shown here, where QA ≥ 1 (marginal and better quality) is labeled as "QA123", QA=3 (the best quality) labeled as "QA3".

Area	Lat	Long	Period
Eastern China	20°N - 50°N	100°E - 125°E	2008 and 2010
North America	25°N - 65°N	135°W - 60°W	2008 and 2010
Global land	—	—	Jan and Jul in 2008 and 2010

Table 5.1: Information of three case studies.

5.4.1. AOD comparison between BRF_DT and C6_DT

Figure 5.4 presents a sample over south of China. We can roughly see a high aerosol loading over this area where the AOD retrieved by both DT algorithms are > 0.3. As indicated by a yellow ellipse area (Guangdong province) in the figure, BRF_DT gives lower AOD than C6_DT with the AOD difference being > 0.1, which becomes significant when a high aerosol loading occurs.

Figure 5.5 shows part of Mexico. We note that a clean sky is present over this area where the retrieved AOD by both DT algorithm is in good agreement and mostly < 0.05, except for the central portion of the area i.e. the Sierra Madre Mountain in Mexico (indicated by a yellow ellipse) where the AOD difference goes up to 0.06. In this region, the bright surface is characterized by sparse grass/vegetation, bare soil and rocks. C6_DT AOD is apparently affected by this bright surface, showing a large spatial variability while BRF_DT performs better giving smoother AOD retrievals. Due to the surface effects, the large errors of C6_DT AOD may be denoted by the QA flag. To evaluate this, the AOD retrievals over this area were separated into two groups: one with the best quality (QA3) and the other with a lower quality (QA12), shown in Figure 5.6. We found, however, that the errors on AOD still largely remain in C6_DT for both groups. This demonstrates that QA flag cannot identify good retrievals with C6_DT in this case.

Figures 5.7, 5.8 and 5.9 show histograms of MODIS AOD for Eastern China and North America for four months (January, April, July, and October in 2008), and for global land for two months (January and July in 2008), respectively. Note that an AOD bin labeled as -0.05 means the AOD ranges from -0.05 to -0.03. Negative retrievals are allowed in

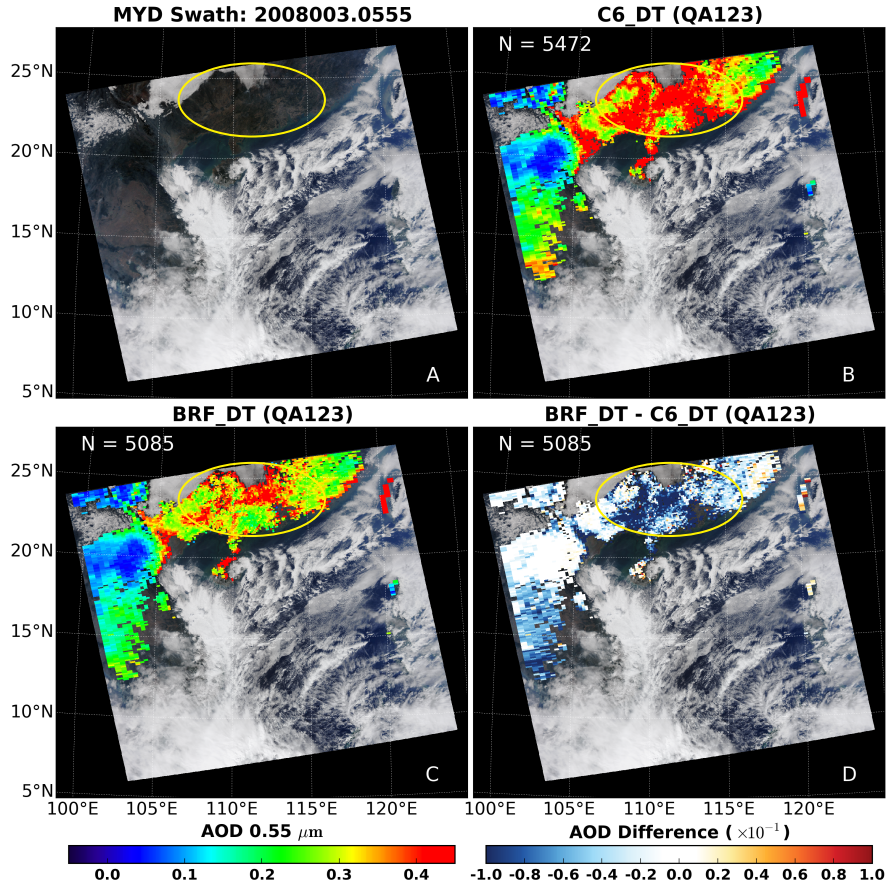

Figure 5.4: AOD over China with QA ≥ 1 (labeled as "QA123"). Figure A-D show MODIS RGB true color, C6_DT, BRF_DT and the difference (BRF_DT - C6_DT AOD), respectively.

the MODIS algorithms and used to make an unbiased statistical analysis (Levy et al., 2007b). This is because the retrievals can be underestimated or overestimated due to the positive or negative uncertainty in the surface reflectance and aerosol properties. Relative or normalized frequencies are given in the plots instead of a total number of AOD retrievals in each bin, because in BRF_DT nearly one-seventh of the retrievals are missing compared to C6_DT, due to cloudy or cloud-contaminated pixels screened out in MCD043A1 during the 8-days period.

Over Eastern China, BRF_DT histograms tend to shift to low bins compared to C6_DT especially for January. This may be caused by the difference between the DT algorithms in estimating the bright surface contribution. Due to less vegetation and more bare soil present in January than in other months, a relatively large AOD is retrieved by C6_DT, while a small AOD is retrieved by BRF_DT. This effect caused by a bright surface is also

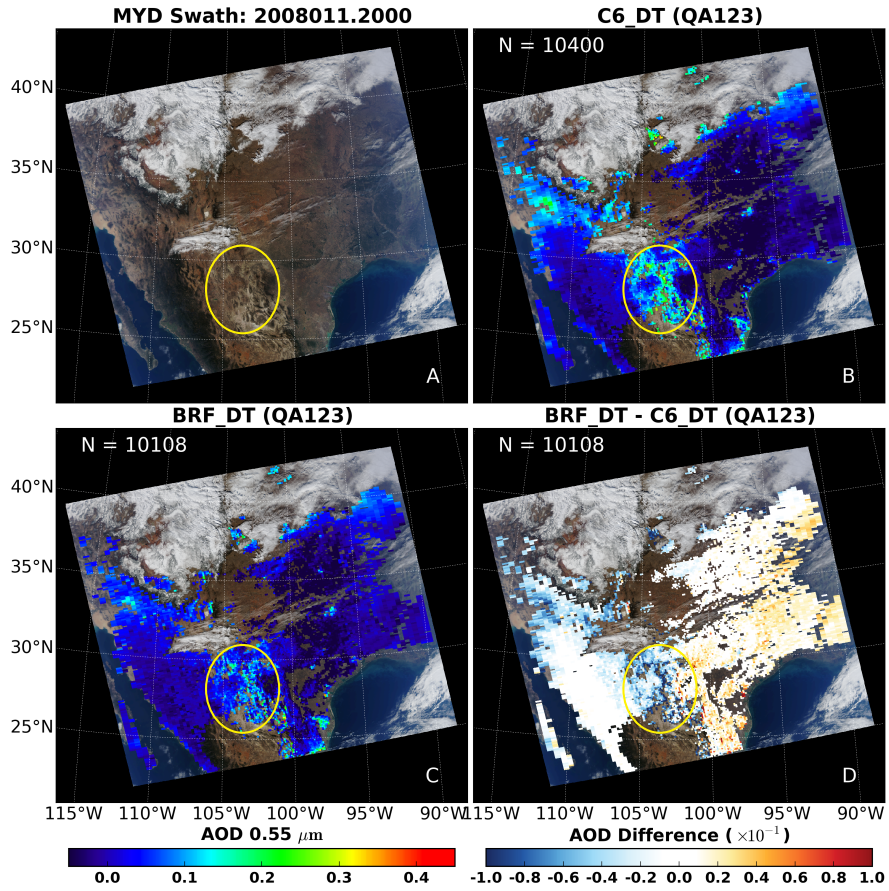

Figure 5.5: AOD over Mexico with QA ≥ 1 (labeled as "QA123"). Symbols are similar to Figure 5.4.

shown in Figure 5.5 as discussed above.

In contrast, the histograms of C6_DT and BRF_DT AOD over North America and global land areas (Figure 5.8 and 5.9) do not show very significant differences as Eastern China. This is mainly due to the relatively low aerosol loading (mostly $\tau < 0.25$) atmosphere over North America and global land areas that would make equation 5.1 close to 2.8 where the diffuse radiation is less observed by MODIS (refer to Case Two discussed above).

5.4.2. Validation with AERONET AOD

The new AOD retrievals were validated using AERONET AOD data with the rule introduced in section 4.4.1 in Chapter 4. To check the performance of the BRF_DT and C6_DT algorithm on QA and scattering angle, the corresponding AOD validation with AERONET measurement is shown.

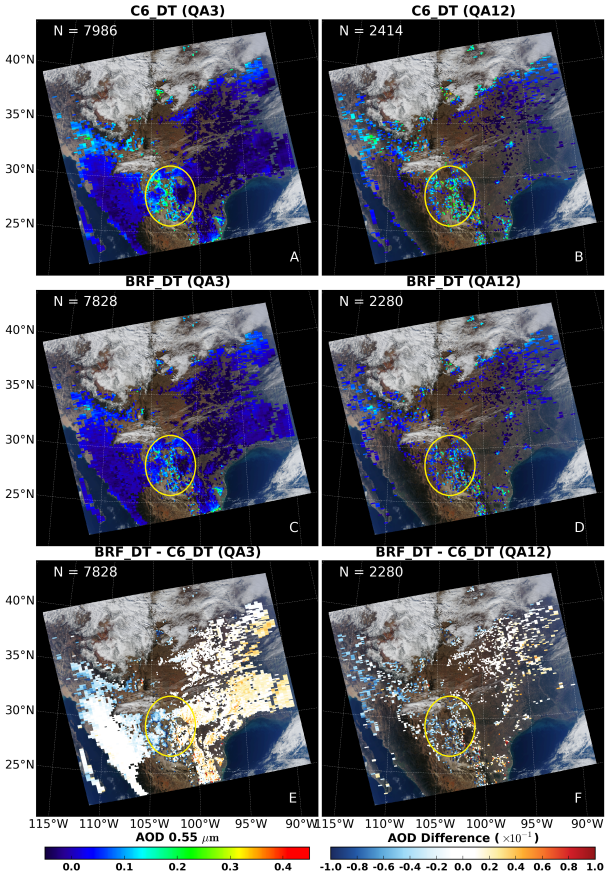

Figure 5.6: AOD with other QA over Mexico. QA=3 was labeled as "QA3", and QA=1 or 2 labeled as "QA12". Symbols are similar to Figure 5.4.

AOD validation with QA

In preparation of the validation experiment, the retrieved AOD were separated into 5 groups based on the combination of QAs, with statistics such as the percentage of data within EE, above EE and below EE, bias (mean(MODIS AOD)-mean(AERONET AOD)), and correlation coefficient R in the linear regression.

Tables 5.2, 5.3 and 5.4 show the statistics of the AOD validation in Eastern China, North America, and global land area, respectively. We note that the retrievals over global land are fewer than over North. America since we just use four months of data for global land whereas two years of data for N. America. The results show that the QA flags work well when using the BRF_DT algorithm. Generally, both DT algorithms show that the AOD accuracy increases as QA flag. For example, QA3 AOD shows 63.7-74% and 71.1-79.5% of retrievals falling within EE for C6_DT and BRF_DT, respectively, which is higher than any other QA or combinations. Compared to C6_DT, BRF_DT shows improvements

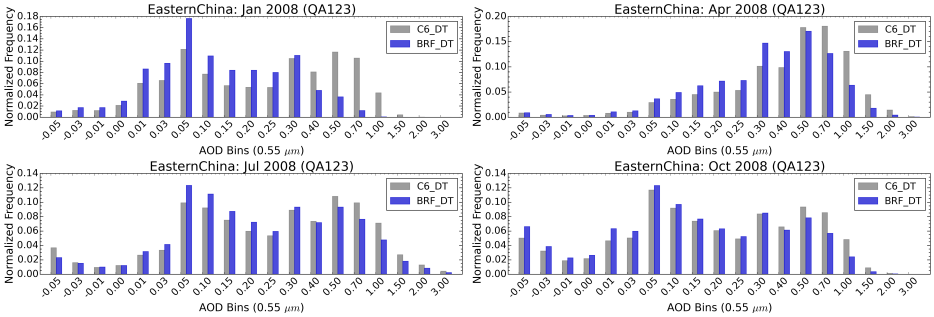

Figure 5.7: Histogram for Eastern China DT AOD (at 0.55 μm) from Aqua for four months. Plotted are data from C6_DT and BRF_DT with QA ≥ 1, labeled as "QA123". Bin labels represent the lower boundary of the bin.

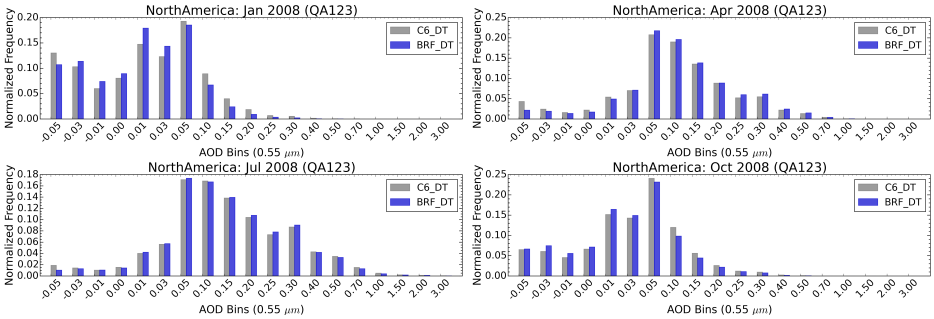

Figure 5.8: Histogram for North America DT AOD (at 0.55 μm) from Aqua for four months. Other symbols are similar to Figure 5.7.

of the AOD retrievals with a larger fraction of retrievals falling within EE, except for QA1 over Eastern China, where a 3 % decrease was found due to too few collocations (60).

Figure 5.10, 5.11 and 5.12 show the scatter plots and box plots for AOD with QA123 and QA3. For the best quality QA3, the accuracy of AOD over Eastern China gets substantially improved in BRF_DT, then North America, with the increase of 7.4% (71.1% − 63.7%) and 5.5% (79.5% − 74%) retrievals falling within EE, respectively, where the biases are significantly reduced from 0.059 to -0.001 and from 0.023 to 0.013. The AOD over global land is less improved with the increase of 2.7% in the retrievals falling within EE. The correlation coefficient R increases only for North America (from 0.80 to 0.83), while it slightly decreases for Eastern China (from 0.94 to 0.93) and global land (from 0.81 to 0.80). AOD with a general quality (QA123) are similar to but show larger improvements where the retrievals falling within EE in BRF_DT increase by 6.4% (66.9% − 60.5%), 9.5% (72.5% − 63.0%) and 5.8% (69.2% − 63.%) over C6_DT, for Eastern China, North America, and global land, respectively.

QA123 AOD in BRF_DT that can meet the 1-σ interval (66%) of EE requirement will be used for a further analysis, which is given in the next section.

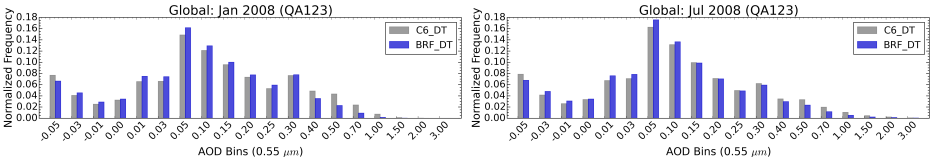

Figure 5.9: Histogram for global land DT AOD (at 0.55 μm) from Aqua for two months. Other symbols are similar to Figure 5.7.

QA	N	% within EE	% above EE	% below EE	Bias	R
1	60	50.0	45.0	5.0	0.075	0.935
	—	**46.7**	**40.0**	**13.3**	**0.022**	**0.750**
12	268	53.7	44.0	2.2	0.097	0.931
	—	**55.2**	**31.0**	**13.8**	**0.020**	**0.838**
123	694	60.5	34.0	5.5	0.072	0.932
	—	**66.9**	**20.7**	**12.4**	**0.001**	**0.895**
23	621	62.6	31.4	6.0	0.070	0.939
	—	**66.8**	**20.6**	**12.6**	**0.004**	**0.910**
3	501	63.7	29.5	6.8	0.059	0.940
	—	**71.1**	**16.8**	**12.2**	**-0.001**	**0.927**

Table 5.2: The statistics of AOD validation over Eastern China. Normal font applies to the C6_DT algorithm, whereas "bold" applies to the BRF_DT algorithm. "—" inicates the same number N in the line above. QA1 means QA=1, QA123 means QA ≥ 1, other QAs are similar to.

AOD validation with the scattering angle

To check whether the performance of DT algorithms depends on geometrical illumination and viewing angle, the MODIS AOD co-located with AERONET measurements were grouped into 20 equal bins and sorted by the scattering angle (the angle between the direction of the solar incident flux and the direction of the reflected flux into the view of the sensor). Eastern China was not shown due to too few co-locations in this region.

Figure 5.13 presents the AOD errors with the two DT algorithms as a function of scattering angle, where AOD retrieval with QA123 are used. One standard deviation 1-σ ("box height"), median ("star or circle") of AOD error and EE line ("dashed line") are plotted in the figure.

The AOD retrievals were significantly improved at small scattering angles ($\Theta < 140°$ and $\Theta < 125°$ for global land and North America, respectively) in BRF_DT where the 1-σ errors are well within the EE line. Nevertheless, this is not the case at a large scattering angle ($\Theta \geq 140°$ and $\Theta \geq 125°$ for global land and North America, respectively), where the retrievals were improved less when $\Theta > 160°$. On the other hand, the positive biases of AOD were substantially reduced in BRF_DT where the median errors of AOD get close to zero, although there are small negative biases at small scattering angles ($\Theta < 110°$).

5.4.3. Summary

Based on the sample plots and histograms as well as analysis and comparison against AERONET measurements, the AOD retrievals in C6_DT were improved by applying BRF_DT.

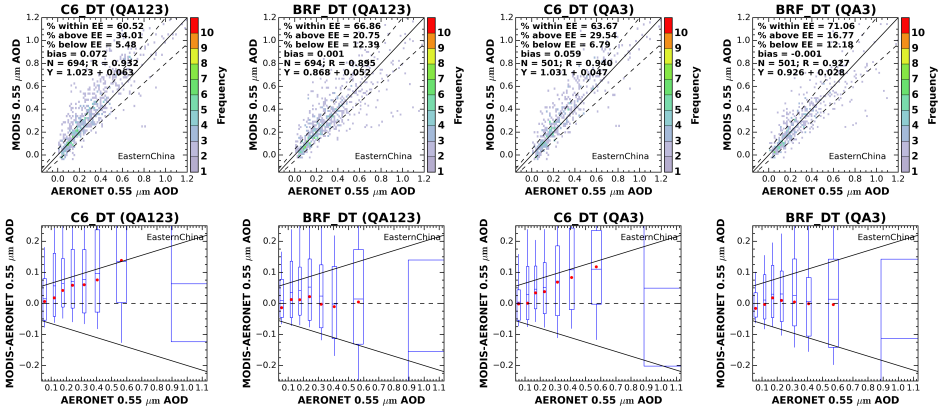

Figure 5.10: The comparison of AOD between C6_DT and BRF_DT algorithm over Eastern China. That shown are scatter and box plots of the retrieved AOD with QA ≥ 1 and QA=3 filtered against AERONET AOD. In scatter plots, dash line is Expected Error (EE) ±(0.05 + 15%) and the solid line is one-one line. Note that QA ≥ 1 was labeled as "QA123" and QA=3 labeled as "QA3". The AOD error (retrieved AOD - AERONET AOD) in box plots are broken into equal numbers bins of AERONET AOD. Dash line and solid black line are zero error and EE, respectively. For each box-whisker, width is 1-σ of the AOD bin, whereas height, whiskers, middle line and red dots are the 1-σ, 2-σ, mean, and median of the AOD error, respectively.

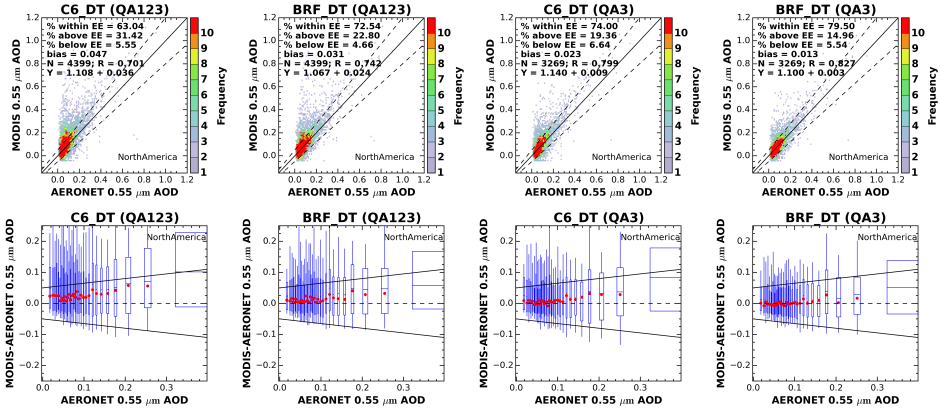

Figure 5.11: Except for North America, others are the same as Figure 5.10.

QA	N	% within EE	% above EE	% below EE	Bias	R
1	408	33.3	60.3	6.4	0.120	0.465
	—	**44.4**	**51.2**	**4.4**	**0.101**	**0.527**
12	1645	39.1	56.7	4.2	0.104	0.605
	—	**52.3**	**45.0**	**2.7**	**0.079**	**0.663**
123	4399	63.0	31.4	5.5	0.047	0.701
	—	**72.5**	**22.8**	**4.7**	**0.031**	**0.742**
23	4015	66.3	27.7	6.0	0.040	0.721
	—	**75.0**	**20.0**	**5.0**	**0.025**	**0.761**
3	3269	74.0	19.4	6.6	0.023	0.799
	—	**79.5**	**15.0**	**5.5**	**0.013**	**0.827**

Table 5.3: The statistics of AOD validation over North America. Other symbols are similar to Table 5.2.

QA	N	% within EE	% above EE	% below EE	Bias	R
1	264	46.6	47.0	6.4	0.081	0.721
	—	**55.3**	**39.4**	**5.3**	**0.062**	**0.651**
12	1100	50.7	44.4	4.9	0.072	0.751
	—	**61.0**	**33.8**	**5.2**	**0.051**	**0.711**
123	2755	63.4	27.3	9.4	0.029	0.777
	—	**69.1**	**18.9**	**11.9**	**0.009**	**0.761**
23	2444	66.0	23.7	10.3	0.021	0.781
	—	**70.7**	**16.2**	**13.0**	**0.002**	**0.772**
3	1923	69.7	18.1	12.2	0.006	0.809
	—	**72.4**	**12.7**	**14.9**	**-0.009**	**0.800**

Table 5.4: The statistics of AOD validation over global land. Other symbols are similar to Table 5.2.

Since much of the Earth land surface is not “dark”, these results are dependent on whether the applied RT model considers the surface anisotropic reflection. The overestimation of MODIS AOD occurring in the case of heavy aerosol loading ($\tau > 0.4$) or bright surface (e.g, Eastern China) was corrected to a large extent. In this case, the surface contribution to the TOA reflectance especially the contribution by surface diffuse reflection is well modeled by BRF_DT, thus yielding a better retrieval. Regional AOD biases can be reduced by the new algorithm. For the case of light aerosol loading ($\tau < 0.25$) and dark surface, the retrievals were less improved (e.g, QA3 AOD over the global land area). This is because the surface BRDF effects are relatively small under these conditions, which substantially reduce the difference in performance between the two DT algorithms.

Further, the angular dependence of the AOD on the scattering angle was significantly reduced, where the overestimations of retrievals were corrected at a small scattering angle. Nevertheless, we found that the overestimation remains at a large scattering angle ($> 140°$). This demonstrates that the strong surface reflectance effect due to the specular reflection or no shadow surface in backward-scattering with the sun behind the sensor, is still underestimated in BRF_DT algorithm, leading to an overestimation of the AOD.

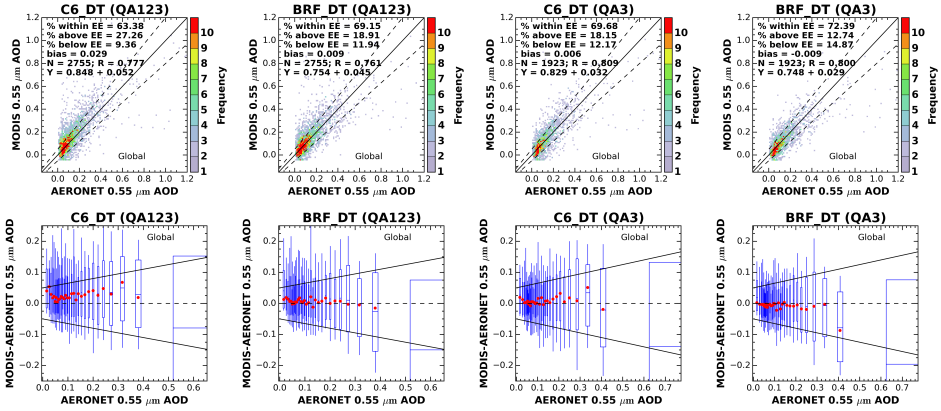

Figure 5.12: Except for global land, others are the same as Figure 5.10.

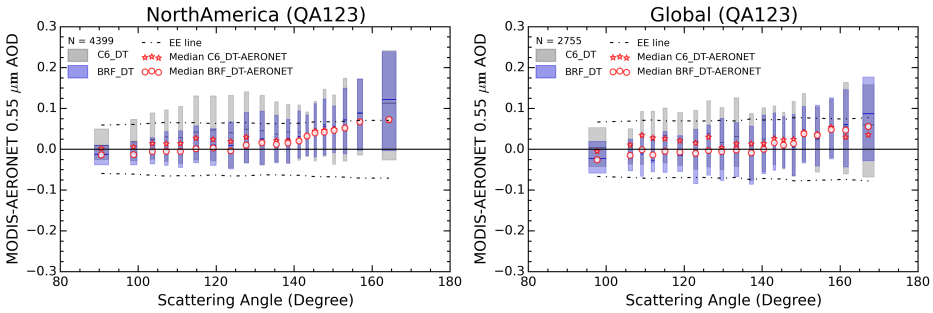

Figure 5.13: AOD at 0.55 μm error as function of scattering angle with QA $\geq$ 1 (labeled as "QA123"). AOD errors are defined as MODIS retrieved AOD - AERONET AOD, broken into equal number bins of scattering angles, the data are plotted for North America and global land respectively. The dash line and solid balck line is EE and zero error. For each box, width is 1-σ of the scattering angles bin, whereas height, middle line are the 1-σ, mean of the AOD error. The colored box "gray" is for C6_DT and "blue" for BRF_DT, whereas red symbols "star" and "circle" are the median of AOD error for C6_DT and BRF_DT, respectively.

5.5. Conclusions

The MODIS AOD produced by the operational algorithm C6_DT can well meet the expected accuracy level of $\pm(0.05+15\%)$ over the global land. However, the AOD over some region violates this accuracy requirement. This problem mainly lies in the uncertainty of the surface contribution in the retrieval since a Lambertian surface is assumed into the algorithm while real land surfaces are non-Lambertian.

In this Chapter, we introduced a new version of the algorihtm to retrieve AOD by considering surface BRDF effects called BRF_DT algorithm. In this algorithm, a lot of legacies were inherited from the C6_DT algorithm, including the gas correction, cloud mask and dark target selection in MODIS data preprocessing as well as the QA flags. The problems were solved in calculating direct atmospheric transmittance and the TOA reflectance in a previous study Yang et al. (2014).

In BRF_DT, three parameters, surface BRF at 2.11 μm, AOD, and fine ratio η, are retrieved. The surface anisotropic reflection is well constrained by using a parameterization of spectral surface BRF and determining surface BRDF albedo (R_{dh}, R_{hd}, and R_{hh}). Specifically, the C6 version relationship is applied for the spectral surface BRF. R_{dh} and R_{hh} are provided by MODIS MCD43A1 black and white sky albedo. Reciprocity law is assumed for hemispherical-directional R_{hd} and directional-hemispherical R_{dh} surface reflectance. Particularly, the TOA reflectance at the long wavelength 2.11 μm is approximately calculated by equation 2.8 due to weak BRDF effects at this wavelength, which differ from the visible (0.466 and 0.644 μm) TOA reflectance that are taken into account by equation 5.1.

The BRF_DT algorithm was applied to three study areas (Eastern China, North America, and global land). With comparisons between the DT algorithms, the results show that the AOD retrievals were significantly improved by BRF_DT. With the best quality AOD (QA3), the number of retrievals falling within EE increases by 7.4%, 5.5% and 2.7% for Eastern China, North America and global land, respectively. Regarding the low quality AOD (QA=1 or 2), the number of retrievals (QA $\geq$ 1) falling within EE increases by 6.4%, 9.5% and 5.8% for these study areas, respectively. Particularly, these retrievals can meet the expected accuracy level $\pm(0.05 + 15\%)$, which means that more reliable AOD retrievals are available for practical use that would greatly benefit users for scientific research. For instance, the retrievals with the full quality (QA123) can give about 50% more points than with the best quality only (QA3). The problem of data gaps due to bright surfaces (e.g, urban and bared soil areas) can be greatly alleviated. This would benefit the aerosol-related research, such as the research on monitoring urban air quality and aerosol radiative forcing.

6

MODIS Dark Target AOD algorithm: Refining the parameterization of land surface spectral reflectance

Based on: Wu, Y., de Graaf, M., and Menenti, M. (2016). Improved MODIS Dark Target aerosol optical depth algorithm over land: angular effect correction. *Atmos. Meas. Tech.*, 9(11):5575–5589.

6.1. Introduction

Following the selection of dark target pixel in the C6_DT algorithm, a new AOD retrieval algorithm called BRF_DT was developed to take into account the anisotropic reflectance of the land surface, and has shown improvements over C6_DT (Chapter 5). BRF_DT still gives a strong angular dependence of the retrieval, however, including a lot of negative retrievals (physically invalid). This is attributed to the parameterization of spectral surface reflectance that causes large errors in the retrieval when aerosol loading is low. Therefore, the parameterization of spectral surface reflectance should be further refined, by considering the variability of the parameterization with land cover and illumination and view angles.

This study aims at reducing the angular dependency of the retrieval by updating the parameterization of the spectral surface BRF. The improved BRF_DT algorithm is called BRF_DT2 here. Section 6.2 describes the AERONET-based Surface Reflectance Validation Network (ASRVN) data to derive the relationship between the VIS and SWIR spectral surface BRF. Section 6.3 describes how this relationship was obtained with 3 years (2005-2007) of ASRVN data. Section 6.4 presents the AOD retrieval by the new algorithm, and its validation with AERONET measurements. The AOD retrievals of the current and operational MODIS C6_DT algorithm and the previous BRF_DT algorithm are used in this Chapter to evaluate the algorithms and get a better understanding of the differences in accuracy. Conclusions are presented in section 6.5.

6.2. ASRVN data

The ASRVN algorithm provides high quality data on spectral surface bidirectional reflectance and albedo by explicitly performing atmospheric correction, using 50 × 50 km^2 samples of MODIS level 1B data and AERONET aerosol and water-vapor information (Wang et al., 2009). With a semi-analytical Green function solution (Lyapustin and Knyazikhin, 2001), LSRT BRDF kernels (the same kernel model as in MCD43A1) are integrated into radiative transfer calculation to generate accurate TOA reflectance. The weights of three LSRT BRDF kernels and the surface BRF are retrieved by the ASRVN algorithm by fitting the simulated TOA reflectance with MODIS measurements over a 4- to 16-day period.

Although the ASRVN BRF data are not yet fully validated with ground truth, it is expected to have a higher accuracy (e.g., errors < 5%) than MODIS BRDF/albedo products. There are two motivations to use the ASRVN data. Firstly, by using AERONET ground measurements, the information on aerosol and water vapor is well integrated in the atmospheric correction. Secondly, a more accurate shape of the surface BRF can be captured by ASRVN dataset since it does not rely on the assumption of a Lambertian surface which can flatten the variation of surface BRF with geometrical illumination and view angles (Wang et al., 2010). Since the LSRT BRDF kernels are applied in the ASRVN algorithm, the errors would be large at a large scattering angle (e.g., sun behind the sensor) and a large solar or view zenith angle (Lucht et al., 2000). This BRF data is used to update the parameterization of spectral BRF in the new algorithm. More details are discussed in section 6.3.

6.3. Updating BRF ratios of VIS/SWIR

To constrain the surface BRF at visible and 2.12 μm wavelengths in the AOD retrieval, the BRF ratios of visible wavelengths to 2.12 μm were applied in this study. Three years (2005-2007) of ASRVN data from Terra satellite were downloaded (> 28,000 cases). To match the grid resolution (10 km) of MODIS measurements in the algorithm, data were averaged over a 10 × 10 km^2 window with the center at AERONET locations where only the cases that have more than 80% good quality (ASRVN quality flag = 0) falling within the window were used. Additionally, the surface brightness and atmospheric condition (e.g., aerosol loadings) that may have effects on the ratios of the spectral BRF are taken into account in this study. The procedure to derive the BRF ratios is also shown in Figure 6.1.

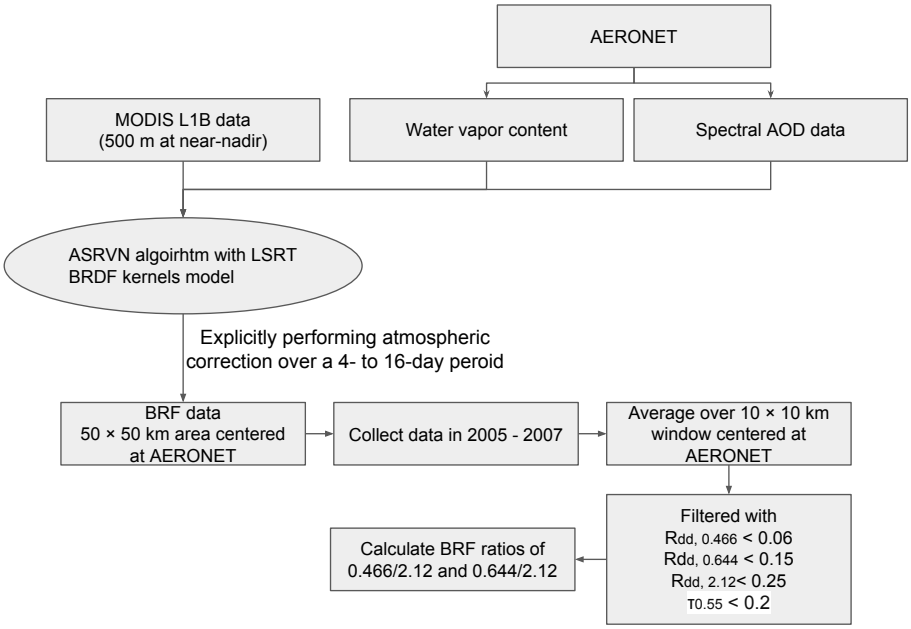

Figure 6.1: Flowchart for the derivation of BRF ratios using ASRVN BRF data. With a semi-analytical Green function solution, the ASRVN algorithm integrates LSRT BRDF kernels into radiative transfer calculation to generate accurate TOA reflectance. This algorithm retrieves the BRF data from MODIS L1B measurements, by explicitly performs atmospheric correction with the information of water vapor content and spectral AOD provided by AERONET. The retrieved BRF data are given in samples of 50 × 50 km with the center at AERONET locations. Three years (2005 - 2007) of BRF data are collected and averaged over the window of 10 × 10 km with the center at AERONET locations, and further filtered with the surface brightness and atmospheric condition, e.g., $R_{dd,0.466} < 0.06$, $R_{dd,0.644} < 0.15$ and $R_{dd,2.12} < 0.25$ with $\tau_{0.55} < 0.2$. The BRF ratios of 0.466/2.12 and 0.644/2.12 are calculated from the filtered data.

To ensure that dark target pixels are used, the BRF dataset was filtered with $R_{dd,0.466} < 0.06$, $R_{dd,0.644} < 0.15$ and $R_{dd,2.12} < 0.25$. The data retained past the filtering are expected to match the required dark surface properties in the DT algorithm in which the measurements are selected after masking the pixels of cloud, water and snow-ice over the 20 ×

20 pixels box (500 m resolution) with the measured 2.12 μm reflectance ranging between 0.01 and 0.25, and removing the brightest 50% and the darkest 20% of the measured 0.66 μm reflectance (Remer et al., 2005; Levy et al., 2007b, 2013b).

The dataset was further filtered with light aerosol loading (τ at 0.55 μm < 0.2, hereafter we use τ for 0.55 μm), to account for the high accuracy of the BRF data for this case (2739 cases). Under light aerosol loading, the measured radiation at TOA is dominated by the directional radiance determined by the bidirectional reflection at the surface. In contrast under heavy aerosol loading, the TOA reflectance is dominated by the diffuse surface reflection. Therefore, the surface BRF is expected to be more accurate under light aerosol loading than under heavy aerosol loading. Actually, with τ < 0.2 the BRF ratio 0.466 μm to 2.11 μm (0.466/2.12) would differ 10% in linear correlation coefficients (R) from that with full aerosol loading.

Figure 6.2 presents scatter plots of the surface BRF ratios for VIS vs SWIR filtered by the dark target and low aerosol loading (τ < 0.2). The BRF ratios obtained by linear regression were 0.268 and 0.589 for 0.466 vs 2.12 and 0.644 vs 2.12, respectively. We note that the 0.466 vs 2.12 data points have a low correlation coefficient R (0.49), with a larger dispersion than 0.644 vs 2.12 (R=0.89). The low correlation of BRF for VIS vs SWIR especially for 0.466 vs 2.12 implies that other factors may have strong effects on the reflectance and their ratios. These factors could be the illumination and view angle and surface cover type. The details of their effects on the ratios are discussed below.

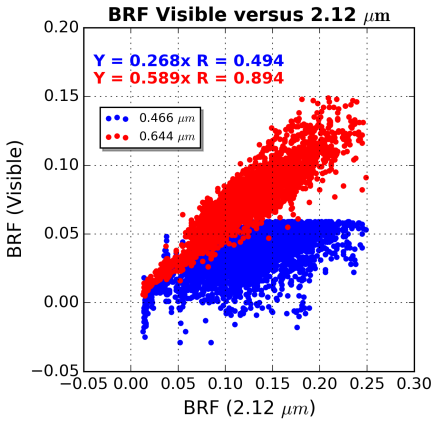

Figure 6.2: The BRF visible (0.466 and 0.644 μm) versus 2.12 μm wavelength, filtered by the dark surface selection i.e. $R_{dd,0.466}$ < 0.06, $R_{dd,0.644}$ < 0.15 and $R_{dd,2.12}$ < 0.25. The data was selected with AOD < 0.2. The ratios are obtained by forcing linear regressions through the origin.

6.3.1. BRF ratios of VIS/SWIR with scattering angle

It was shown that the BRF ratios VIS/SWIR may depend on view and illumination angle over a vegetated area (e.g., Gatebe et al., 2001). This is because vegetation (e.g., plant canopies) is not randomly oriented (Rondeaux and Vanderbilt, 1993), which could lead to different ratios with different angles. Generally, the illumination and viewing angle are: solar zenith angle, solar azimuth angle, sensor zenith angle and sensor azimuth

angle. To simplify the notation for illumination and view angles, we use one variable — the scattering angle (see Figure 2.2 and equation 2.19) instead, which is a function of these four angles (e.g., Levy et al., 2007b; Hsu et al., 2013).

Sorted by the scattering angle, the data (2739 cases) were put into 20 groups of equal size (about 140 points for each bin of the scattering angle), where the median values of each bin were used for the linear or non-linear regression.

Figure 6.3 A - C presents the dependence of the surface BRF on the scattering angle at three wavelengths (0.466, 0.644 and 2.12 μm). The BRFs at 0.644 and 2.12 μm present a fairly flat trend with increasing scattering angle and their low correlation coefficients R (< 0.45). This is not the case for the 0.466 μm BRF data, which show a significant increasing trend (R = 0.75) with the scattering angle. This suggests that the angular shape of the surface BRF tends to be more important at a shorter wavelength. This is comparable with the findings of Wang et al. (2010).

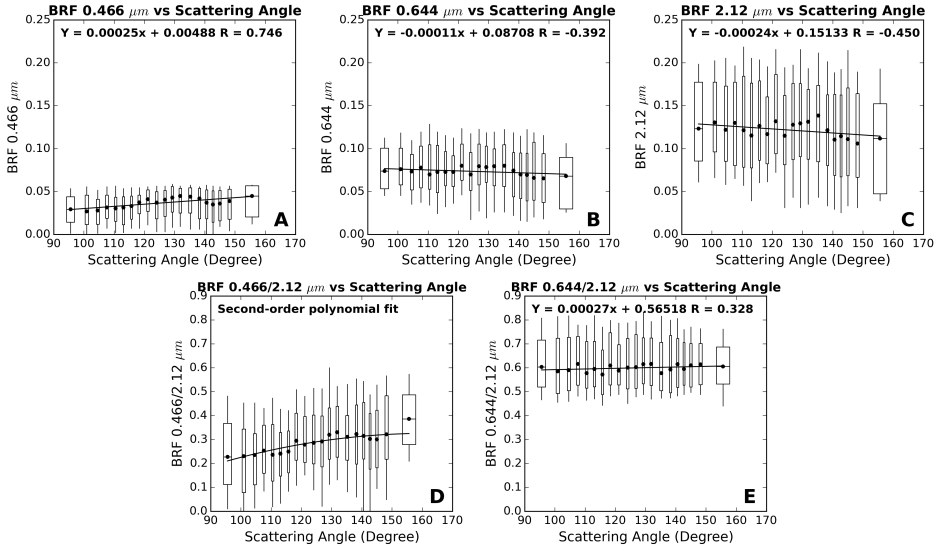

Figure 6.3: The dependence of the spectral BRF on the scattering angle. The dataset (2739 cases) with the dark target pixels was sorted and grouped into 20 bins by the scattering angle. Each bin has around 140 cases. On all subplots, dot, the height of box and the length of whisker for each bin indicate the median value, 1-σ and 2-σ of the reflectance or ratios, respectively. The width of box means 1-σ of the scattering angle for each bin. The first row shows the surface BRF at each wavelength (0.466, 0.644 and 2.12 μm) as function of the scattering angle. The second row shows the ratios of the surface BRF 0.466/2.12 and 0.644/2.12 as a function of the scattering angle.

Figure 6.3 D and E show the dependence of BRF and their ratios on the scattering angle for 0.466/2.12 and 0.644/2.12, respectively. We note that the ratio 0.644/2.12 is nearly insensitive to the scattering angle with a small slope (0.00027) of the regression, but with large uncertainties. The insensitivity of the ratio is due to their similar and nearly flat trend with the scattering angle. The large uncertainties are mainly due to the diverse surface type. This will be further discussed in the next section. To account for the non-linearity of the 0.466/2.12 ratio with the scattering angle, a second-order polynomial fit

was applied. In addition, data with last bin (large scattering angle) were neglected in the fitting process because of the large errors of the BRF in this case as mentioned above.

6.3.2. Effects of surface type or $NDVI_{SWIR}$ in the BRF ratios of VIS/SWIR

To evaluate the variability of the BRF ratios with land cover or season, the MODIS Land Cover Type/Dynamics MCD12C data during the year of 2006 were used for this analysis. The BRF data with urban and non-urban types were regrouped and further separated into summer and winter cases (summer: June-July-August, winter: December-January-February). For urban sites, the ratios of VIS/SWIR (0.466/2.12: ~ 0.3, 0.644/2.12: > 0.6) are generally higher than non-urban sites (0.466/2.12: 0.23 - 0.28, 0.644/2.12: 0.58 - 0.59), while presenting less seasonal variability.

The variability of the BRF ratios due to the change of surface properties might be parameterized using the refined vegetation index $NDVI_{SWIR}$ (see equation 2.18). However, due to the directional effect, $NDVI_{SWIR}$ is insufficient to account for the impact of land cover.

Figure 6.4 shows the dependence of the MODIS observations $\rho^{obs}_{1.24}$ and $\rho^{obs}_{2.12}$ and $NDVI_{SWIR}$ on the scattering angle. These observations were also filtered as done to construct the same dark target pixels dataset as in section 6.3. The medians of $\rho^{m}_{1.24}$ (R=0.89) are much more dependent on the scattering angle than $\rho^{m}_{2.12}$ (R=0.47). As a result, we can see that the median of $NDVI_{SWIR}$ (R=0.874) also gives a significant increasing trend with increasing scattering angle. This suggests that the $NDVI_{SWIR}$ can differ by 0.2 with different scattering angles. This strong dependency of NDVI on surface anisotropy has also been extensively documented in Meyer et al. (1995). The difference of 0.2 in $NDVI_{SWIR}$ would lead to a larger bias by > 0.012 ($\geq 5\%$) in the AOD retrieval when $\tau \leq 0.25$ using C6_DT relationship.

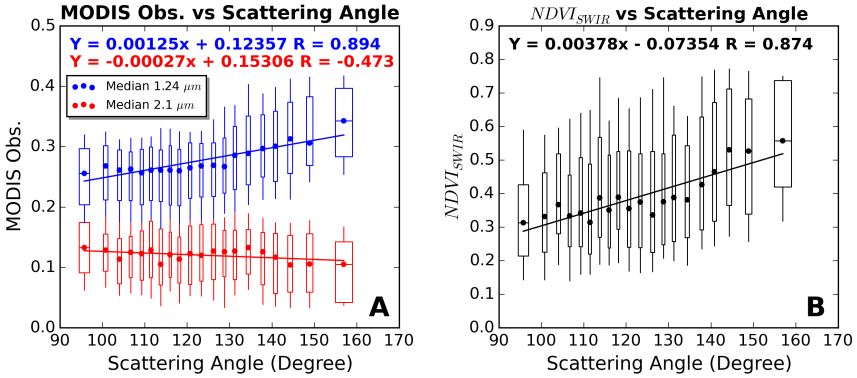

Figure 6.4: The dependence of the MODIS observation at 1.24 and 2.12 μm (obs. in A) and $NDVI_{SWIR}$ (B) on the scattering angle. Blue and red indicate the observation at 1.24 and 2.12 μm, respectively. Except for the color, other symbols are as in Figure 6.3.

Unfortunately, it is not easy to correct the directional effects on $NDVI_{SWIR}$. If we simply follow the linearly regressed relationship in Figure 6.4B, the effects will be poorly corrected because the nonlinearity and large uncertainty $\pm(0.05+0.15)$ add up to a com-

parable magnitude as the directional difference (0.2) in the relationship.

6.3.3. Final BRF ratios of VIS/SWIR

Results of the analysis on the 3-year ASRVN BRF dataset over around 100 AERONET sites show that the BRF ratio of VIS/SWIR has a dependence on the scattering angle and surface type. Due to the disturbance of the directionality, the $NDVI_{SWIR}$ cannot be used to refine the BRF ratio. Thus, $NDVI_{SWIR}$ will not be taken into account in the BRF parameterization. The final ratios in BRF_DT2 are:

$$\begin{aligned} R_{0.644/2.12} &= \frac{R_{dd,0.644}}{R_{dd,2.12}} \\ &= 0.00027\Theta + 0.5651 \end{aligned} \tag{6.1}$$

$$\begin{aligned} R_{0.466/2.12} &= \frac{R_{dd,0.466}}{R_{dd,2.12}} \\ &= -2.663055 \times 10^{-5}\Theta^2 + 8.592420 \times 10^{-3}\Theta - 0.3671062 \end{aligned} \tag{6.2}$$

6.3.4. AOD errors caused by BRF ratio uncertainties

To clarify the effect of omitting $NDVI_{SWIR}$ in the AOD algorithm, we compared the uncertainty in the retrievals between BRF_DT and BRF_DT2 over the global land area. To avoid the angular effects in the results, the retrievals were sorted in bins of the scattering angle. It was found that these algorithms give a similar (< 1%) uncertainty in the retrieval (more details in Section 6.4.2). This demonstrates that the removal of $NDVI_{SWIR}$ would not cause too much error in the new algorithm.

We also note that the BRF ratios still have a large uncertainty even by accounting for the scattering angle, which may cause errors in the AOD retrieval. The standard deviation of the estimated 0.644 vs 2.12 ratio is about ±0.1 and even larger for 0.466/2.12 ratio (about ±0.12). To evaluate the effects of the uncertainty in the BRF ratios on the AOD retrieval, we performed a sensitivity test for a given typical vegetation area where $R_{dd,2.12}$ is around 0.15 calculated with the BRDF kernel code *brdf_forward* (see website https://www.umb.edu/spectralmass/terra_aqua_modis/modis_user_tools). In this test, we added one standard deviation on the BRF ratios (e.g., $R_{0.466/2.12} \pm 0.12, R_{0.644/2.12} \pm 0.1$). We found that the ratios uncertainty can cause > 0.054 (> 22%) errors in the AOD retrieval when $\tau \leq 0.25$. Nevertheless, the errors become small with increasing aerosol loading. For example, when $\tau = 0.5$, the error becomes 0.025 (5%).

Nevertheless, these errors can be generally well absorbed by the expected error (EE) envelope ±(0.05 + 15%). Thus, the current ratios can be used for the new algorithm.

6.4. Results & Discussion

The BRF_DT2 algorithm was applied to the areas with light aerosol loading ($\tau < 0.2$) since heavy aerosol loading (e.g, $\tau = 0.5$) would not produce very different results by updating the new BRF ratios as we discussed. Two cases were selected, in which 2008 and 2010 data are over North America (25°N - 65°N, 135°W - 60°W), and 4 months (January and July in 2008 and 2010, respectively) of data are from the global land areas, see Table 6.1. We note that the global land and North America areas give a mean AOD of 0.15 and 0.1,

respectively. The AOD with the best quality QA=3 (labeled as "QA3") is presented.

Area	Lat	Long	Aerosol Loading
North America	25°N - 65°N	135°W - 60°W	Light (AOD=0.1)
Global land	—	—	Medium (AOD=0.15)

Table 6.1: Information on two case studies. Here, the AOD is obtained by averaging the corresponding AERONET measurements.

To better understand the difference among the DT algorithms, the MODIS C6_DT and BRF_DT AOD retrievals were also investigated in this study. The comparisons were divided into two parts: one is a cross-comparison of AOD retrievals among DT algorithms, the other is the evaluation of their performance against AERONET AOD.

6.4.1. Cross comparison among DT AODs

Figure 6.5 shows an example of Argentina retrieved on 16 January 2008, which illustrates the new AOD and the difference between C6_DT and BRF_DT AOD. The AOD over this area is normally < 0.25. Several surface types are shown in Figure G, including dense dark vegetation (farmland and forest), dry grass or bare soil, and green grass from the western coast to northwestern regions.

In Figure 6.5 D (areas south of 45°S), the differences in the AOD retrievals with both BRF_DT2 - C6_DT and BRF_DT2 - BRF_DT do not vary with $NDVI_{SWIR}$. This demonstrates again that the omission of $NDVI_{SWIR}$ in the parameterization does not significantly affect the retrieval.

In the yellow ellipse area shown in Figure 6.5, we can see that BRF_DT and BRF_DT2 AOD are spatially smoother than C6_DT. This to some degree demonstrates that BRF_DT and BRF_DT2 AOD are much less affected by the anisotropic reflection of the underlying surface. For the whole land area shown in Figure 6.5, the difference of BRF_DT2 - BRF_DT AOD presents a significant dependence on the scattering angle, where a positive difference of 50% (0.06) was found at small scattering angles ($\Theta \leq 130°$), and a negative difference (-0.06) at large scattering angles ($\Theta \geq 150°$), while a weaker dependence was found for the difference BRF_DT2 - C6_DT AOD.

Figure 6.6 and 6.7 present global maps ($1° \times 1°$) of mean AOD retrieved by C6_DT, BRF_DT and BRF_DT2, in January and July 2008, respectively. The new algorithm shows a mean AOD of around 0.144 (January, July: 0.127, 0.160), with a reduction of ~ 0.03 compared with C6_DT. Roughly, the reductions (~ 0.1) mainly appear in large aerosol loading areas, such as northern South America, central Africa (around the Equator) and southern China (around 30°E), whereas light loading areas (e.g., South America and Australia) give an increase of AOD (~ 0.04). The mean AOD difference is small (0.002) between the new algorithm and BRF_DT. This is mainly due to the compensation between small and large scattering angles in the averaging process over 1 month. We will further evaluate the AOD difference between the algorithms in the validation section.

Figures 6.8 and 6.9 show histogram of MODIS AOD (QA=3) for North America over 4 months (January, April, July and October in 2008), and the global land with 2 months (January and July in 2008) of data, respectively. Several AOD bins range from -0.05 to 3.0, where each bin is labeled as one number (e.g., one bin labeled as -0.05 means that the

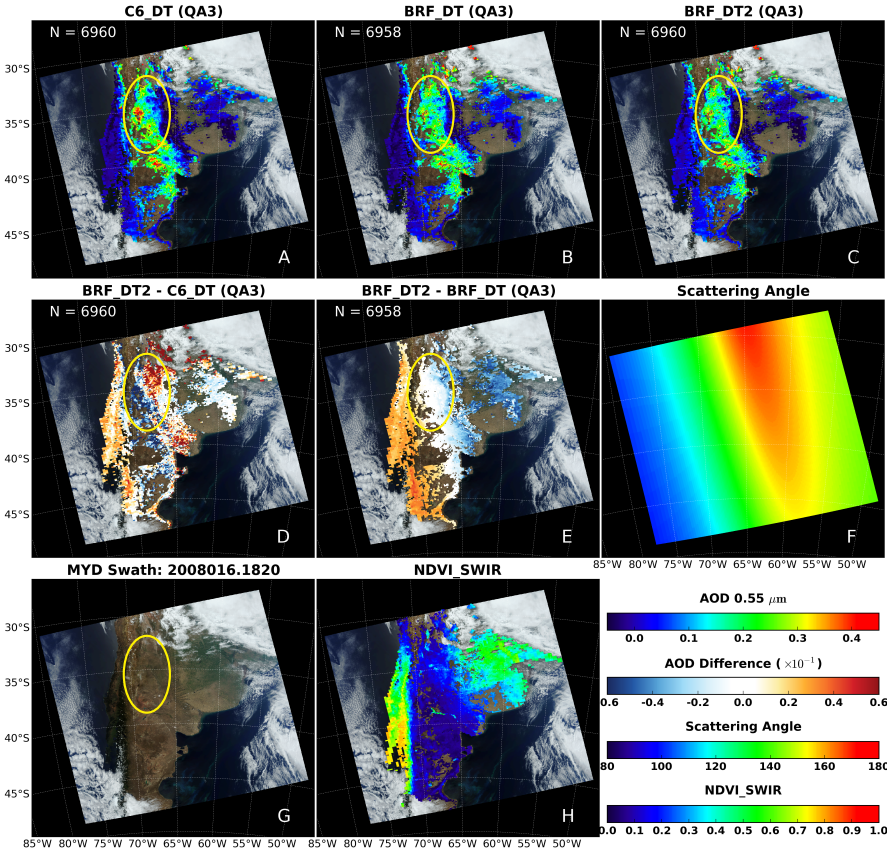

Figure 6.5: AOD over Argentina. Figure A-C show the AOD retrieved by the C6_DT, BRF_DT and BRF_DT2 algorithm. AOD with QA=3 was labeled as "QA3". Figure D and E show the AOD difference between DT algorithms. Figure F - H show the MODIS scattering anle, the MODIS RGB "true color" and $NDVI_{SWIR}$. The MODIS RGB image is obtained through combination of MODIS three channels 1, 4 and 3.

AOD varies between -0.05 and -0.03). Due to the mask of cloudy or cloud-contaminated pixels in ancillary data (8-day MCD43A1), the number of BRF_DT and BRF_DT2 retrievals was near one-seventh less than C6_DT. Thus, the normalized frequency is given for each bin.

A significant difference was found between C6_DT/BRF_DT and the new algorithm. It seems that the difference is dependent on the months or seasons. We can see that a small difference appears in April and July for North America in Figure 6.8. The variation of vegetation amount with the seasons or months is a key factor for accurate retrievals. For North America, the vegetation is abundant and green in spring (e.g., April) and summer (July) and less abundant in autumn (October) and winter (January). $NDVI_{SWIR}$ is saturated over the area with abundant green vegetation, thus showing less directionality than the less vegetated area (e.g., sparse vegetation and bare soil). As a result, BRF_DT

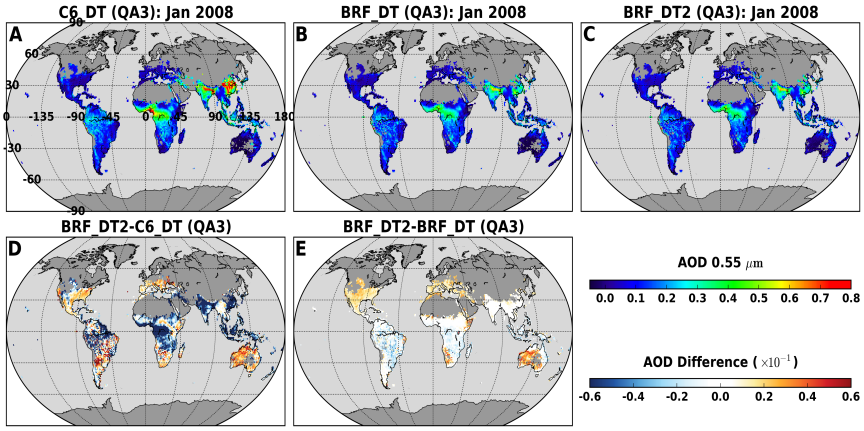

Figure 6.6: January 2008 maps (1° × 1°) of mean AOD filtered with the best quality QA=3 (labeled as "QA3") over global land. Figure A-C show the AOD retrieved from C6_DT, BRF_DT and BRF_DT2, respectively. Figure D and E show the AOD difference of BRF_DT2 - C6_DT and BRF_DT2 - BRF_DT, respectively.

and BRF_DT2 give similar AOD retrievals for a vegetated area and different retrievals with lower vegetation cover.

In the global land area the differences are not so significant as for North America. The differences are smaller in January, and larger in July compared to North America. This is because for the global land the mean vegetation amount does not vary too much over time.

Particularly, the negative retrievals (-0.05 < AOD < 0.0, the sum of the first three bins) are significantly reduced with the new algorithm, compared with C6_DT and BRF_DT. The reduction of the negative retrievals is more significant in North America, with the decrease by 16% (-0.16 = 0.19-0.35) in January and 7% in October. The reduction becomes only 4% for the global land area. Obviously, the negative retrievals tend to be more likely with low aerosol loading (see also Figure 6.6 and 6.7). To further clarify the reduction of the negative retrievals, we evaluate similar histograms for light aerosol loading: Brazil and Australia (see Figure 6.10). The location of these areas is given in Table 6.2. We found that the reduction was 6% - 11% and 11% - 23% in the Brazil and Australia areas when applying the new algorithm, respectively.

Area	Lat	Long
Australia	15°S - 35°N	105°E - 155°E
Brazil	20°S - 0°	55°W - 30°W

Table 6.2: Location of the areas in Brazil and Australia evaluated in the case studies.

6.4.2. Validation with AERONET AOD

The validation method is similar to the one applied in Chapter 4. By this method, we evaluated the AOD accuracy of the DT algorithm against AERONET measurements, as

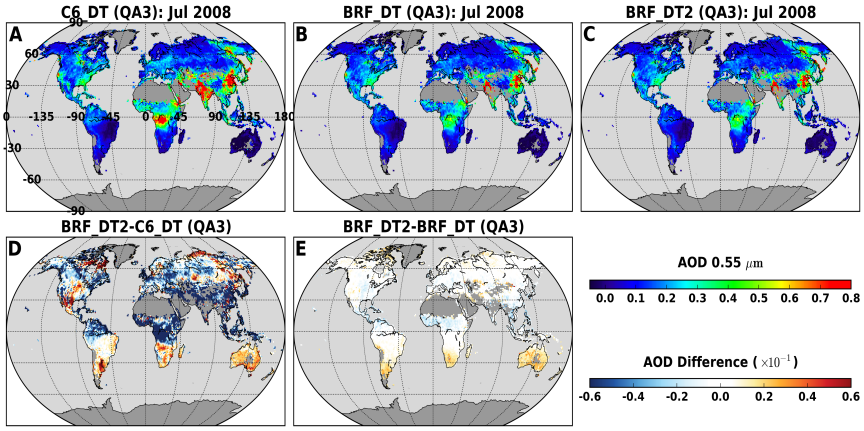

Figure 6.7: July 2008 maps (1° × 1°) of mean AOD filtered with the best quality QA=3 (labeled as "QA3") over global land. Other symbols are similar to Figure 6.6.

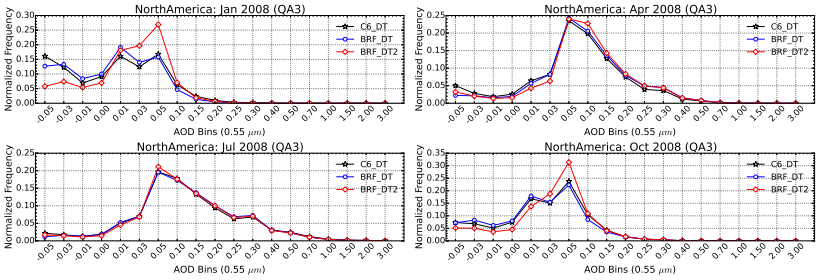

Figure 6.8: Histograms of North America DT AOD (at 0.55 μm) from Aqua for 4 months. Plotted are data from C6_DT, BRF_DT and BRF_DT2 with QA=3, labeled as "QA3". Bin labels represent the lower boundary of the bin. For example, a bin labeled as -0.05 means the AOD between -0.05 and -0.03.

well as the angular dependence of retrievals.

Overall performance of the AOD retrieval

Results are compared with the C6_DT EE $\pm(0.05 + 15\%)$ over land.

Figure 6.11 presents scatter plots of DT AOD retrievals against AERONET over the global land. We can see that there are more retrievals falling within the EE when using BRF_DT2 than C6_DT and BRF_DT, with the increase of 2 and 4.5 % respectively.

Compared with BRF_DT, a 1 % increase of retrievals falling within EE was found in BRF_DT2 for North America (not shown). Although the increase is not significant, it does not really mean small changes between these two algorithms. Applying a stricter EE envelope $\pm(0.03 + 10\,\%)$ for North America, the difference of AOD falling within EE was found to be large (5 % = 64.4–59.5 %) for BRF_DT2–BRF_DT. Nevertheless, this accuracy is so strict that the new retrievals cannot meet the requirement of 1σ interval (66 %).

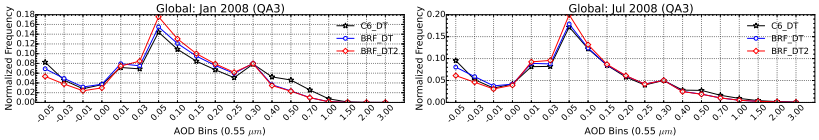

Figure 6.9: Histograms of the global land DT AOD (at 0.55 μm) from Aqua for 2 months. Other symbols are similar to Figure 6.8.

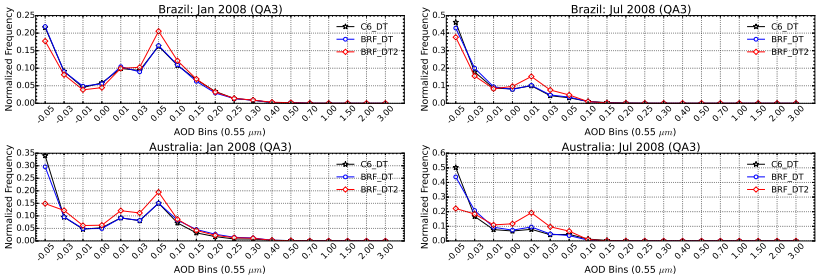

Figure 6.10: Histograms of the AOD (at 0.55 μm) in Brazil and Australia. The AOD data is from the global land area. Other symbols are similar to Figure 6.8.

6

Angular Performance of the AOD retrieval

In order to test whether the AOD retrieval depends on the scattering angle, the MODIS AOD retrievals co-located with AERONET measurements were sorted and grouped into 20 equal bins by the scattering angle.

Figure 6.12 presents the AOD errors of DT algorithms as a function of scattering angle, where the errors are defined as the absolute difference of MODIS - AERONET AOD at 0.55 μm. Several statistics are reported for each bin, which are the 1-σ interval and median (star or circle) of AOD errors that are used to indicate the uncertainty and bias, respectively.

Generally, the errors of the AOD retrievals in all the algorithms vary with the scattering angle. We can see that the 1-σ errors increase with increasing scattering angle. This is mainly due to the estimation accuracy of the surface contribution varying with the scattering angle. The AOD retrieval with the DT algorithms is expected to be accurate when a dark surface is observed since the TOA reflectance is mainly determined by the atmosphere rather than by the surface. Normally, the surface appears darker in the forward scattering angle (eg., $\Theta < 115°$, many shadows observed) while it appears brighter in the backscattering angle (few shadows observed).

The new algorithm presents apparent advantages in the AOD retrieval compared to C6_DT, where the errors of the 1-σ are getting smaller especially for North America. This is mainly due to the accurate estimation of the surface anisotropic reflection in the new algorithm.

Compared to BRF_DT, the new algorithm shows similar 1-σ errors for the two cases. The angular effect on $NDVI_{SWIR}$ in the C6 parameterization leads to a weaker constraint on the spectral surface reflectance, resulting in less accurate retrievals than expected. Conversely, this proves again that the removal of $NDVI_{SWIR}$ in the new parameteriza-

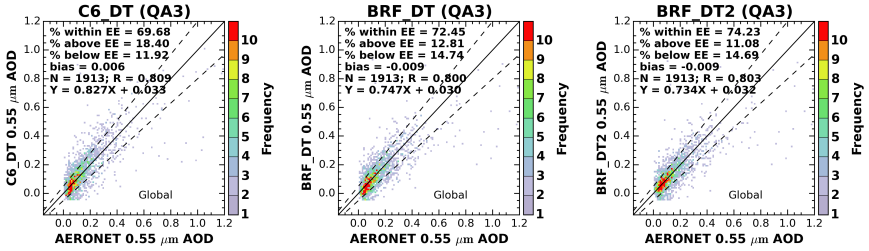

Figure 6.11: The comparison of AOD among the DT algorithms over land. The DT algorithms are C6_DT, BRF_DT and BRF_DT2. The retrieved AOD is filtered with QA = 3, shown against AERONET AOD. The dashed line is Expected Error (EE) $\pm(0.05+15\%)$ and the solid line is the one to one line, respectively. Note that QA=3 is labeled as "QA3".

tion would not give a large error in the AOD retrieval.

Significant differences are observed in the median value of the errors between BRF_DT and BRF_DT2. Over the global land area, the angular bias is largely corrected in the new algorithm compared with BRF_DT, where at small and large scattering angles ($\Theta < 130°$ and $\Theta > 150°$) the median errors of around -0.025 (-17%) and 0.04 (27%), are reduced to ± 0.012 ($\pm 8\%$). The angular correction was also found over North America, although there is still a small positive bias in the new algorithm, over all the scattering angles.

6.5. Conclusions

In the AOD retrieval with satellite measurements, the accurate estimation of the surface contribution is required. Benefiting from the accurate estimation of the surface anisotropic reflectance, the BRF_DT algorithm can yield a better retrieval as compared to C6_DT. However, applied in BRF_DT, the surface reflectance relationship inherited from MODIS C6_DT can lead to an angular dependence of the AOD retrieval. The problem is due to at least two possible issues. The relationship that is derived by assuming a Lambertian surface, is not suitable to estimate the land surface BRF. The vegetation index $NDVI_{SWIR}$ applied in the relationship may have a directional effect, and needs to be reconsidered for the AOD retrieval.

To investigate and improve this situation, BRF_DT was further developed by using new spectral ratios for surface BRF (called BRF_DT2). Three years of ASRVN BRF data were collected and filtered with the dark surface constraints, to derive the new relationship to estimate the surface spectral reflectance. The surface BRFs at 0.466 and 0.644 μm are estimated as a linear function of that at 2.12 μm and the scattering angle. To test the performance of the new algorithm, two areas with different aerosol loading were used: data from North America (light, AOD = 0.1) and the global land area (medium, AOD = 0.15). For the case studies, a cross-comparison of C6_DT, BRF_DT and BRF_DT2 AOD was discussed, as well as the validation with AERONET AOD. The results show that under light aerosol loading (AOD < 0.2) multiple improvements in the AOD retrieval can be achieved with the new algorithm compared to C6_DT and BRF_DT:

- The negative retrievals ($-0.05 < \tau_{0.55} < 0.0$) were significantly reduced, where the reduction can be up to 16% - 23% for some clean air regions ($\tau < 0.1$). The problem

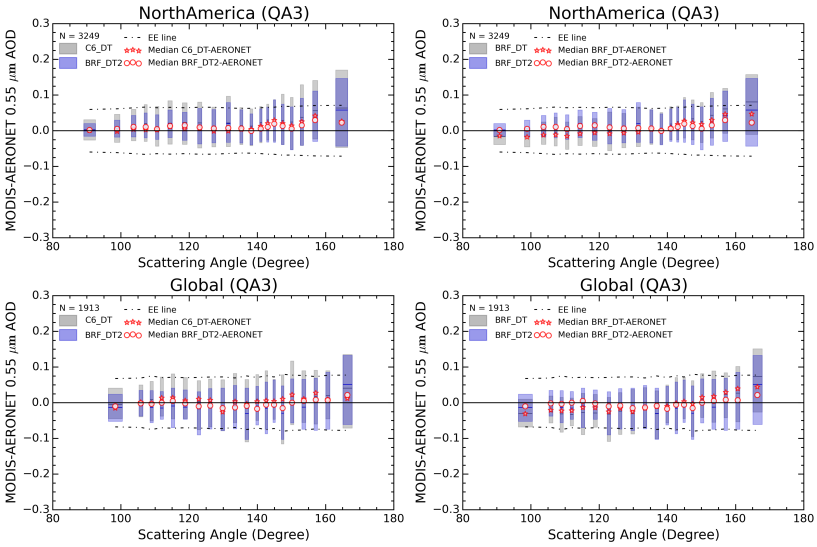

Figure 6.12: AOD at 0.55 μm error as a function of scattering angle with QA=3 (labeled as "QA3"). AOD error is defined as MODIS retrieved AOD - AERONET AOD, broken into equal number bins of scattering angles, the data are plotted for North America and the global land. The dash line and solid black line are EE and zero error. For each box, width is 1-σ of the scattering angles bin, whereas height, middle line are the 1-σ, mean of the AOD error. Shown in the first and second column is the performance between C6_DT and BRF_DT2 and between BRF_DT and BRF_DT2, respectively. Gray indicates C6_DT and BRF_DT and blue is BRF_DT2, whereas red stars are the median of AOD error for C6_DT and BRF_DT and red circles are for BRF_DT2.

of a large number of negative AOD in C6_DT (Levy et al., 2013b), and as well as in BRF_DT, was alleviated with the new algorithm. The ideal result should give none with very accurate surface and aerosol models. Since there are always some uncertainties in these models, obtaining zero negative retrieval becomes impossible.

- The percentage of the retrievals falling within the accuracy level EE=±(0.05+15%) increases 2% and 4.5% for the AOD retrieval over the global land area compared to BRF_DT and C6_DT, respectively. Although a small increase was found in light aerosol loading area North America as compared to BRF_DT, it can still give a significant increase (5%) with a stricter accuracy level ±(0.03+10%).

- The angular bias of the AOD retrieval is largely corrected. At small and large scattering angles ($\Theta < 130^\circ$ and $\Theta > 150^\circ$), the underestimation (-17%) and overestimation (27%) of the retrieval in BRF_DT are reduced to ±8% in the new algorithm, for the global land area. Findings in the North America case study were similar, although a small positive bias of the retrieval remains.

We note that BRF_DT2 does not improve the retieval much over dark surface since the dark surface (e.g., areas in summer) has a small contribution to the TOA reflectance. But the retrievals were significantly improved over not-quite-so-dark surface. This is can be found in areas in Winter (less abundant vegetation), such as North America in January and Australia in July.

7
Conclusion

7.1. Conclusion

In this thesis, we have improved the retrieval of Aerosol Optical Depth (AOD) over land with Moderated Resolution Imaging Sectroradiometer (MODIS) radiometric data. Efforts were invested towards on resolving the main problem targeted by this study: how to improve the MODIS AOD retrieval over land. A brief overview of our research is given as:

- **We have explored the potential error sources in the current version of the MODIS algorithm (collection 6 dark target) (in Chapter 2).**

  The error sources could result from the inappropriate choice of aerosol properties such as predefined aerosol models and a static aerosol vertical profile over the globe, and the land surface that is assumed to be a Lambertian (isotropic reflection).

- **We have evaluated the sensitivity of aerosol optical depth (AOD) retrieval to aerosol vertical profile and type over land with the operational MODIS algorithm (in Chapter 3).**

  In this study, a high sensitivity of the retrieval to different aerosol types and vertical profiles was found under extensive conditions, including 3 aerosol mixtures (3 fine or non-dust aerosols strongly-absorbing smoke, moderately-absorbing generic and non-absorbing urban industrial mixed with dust) and 14 different vertical profiles. With pure smoke or dust aerosols, the retrieved AOD shows errors ranging from 2% to 30% for a series of vertical distributions. Aerosol type errors in the algorithm can lead to errors of up to 8% in the AOD retrieval. The interaction of aerosol type and its vertical profile can give the AOD retrieval errors by over 6%. In addition, the intrinsic errors were found to be > 3% when $\tau > 3.0$.

- **We have developed a new algorithm to obtain an accurate retrieval by considering a dynamic aerosol vertical distribution (in Chapter 4).**

  The impact of the profile on the AOD retrieval was investigated by the synergy of MODIS and Cloud-Aerosol Lidar and Infrared Pathfinder Satellite Observation (CALIPSO) data, over dust and smoke regions. The aerosol vertical distribution has a strong impact on the AOD retrieval. The assumed aerosol layers close to the ground can negatively bias the retrievals in C6_DT. Regarding the elevated smoke and dust layer, the new algorithm can improve the retrieval by reducing the negative biases by 3 - 5%.

- **We have taken into account the land surface anisotropic reflection in our study that would give an accurate estimation of the surface contribution to the top of the atmosphere and yield a better retrieval, with valid physical assumptions (in Chapter 5).**

  The AOD retrieval was significantly improved by our algorithm compared with C6_DT over case studies including Eastern China, North America and global land area. For these cases, all the new retrievals (Quality Assurance QA≥1) can meet the requirement of the Expected Error (EE) $\pm(0.05 + 15\%)$. We found that the retrieval

points falling within the EE increase from 2.7% to 7.5% for the best quality flag only (QA=3), and from 5.8% to 9.5% for the marginal and better quality flag (QA ≥ 1).

- **We have derived an empirical relationship for the spectral surface Bidirectional Reflectance Factor (BRF) using three years of data from ASRVN "IBRF" dataset, to improve the retrieval (in Chapter 6).**

  The retrieval was improved by reducing the angular dependence, including fewer occurrence of the negative retrievals. At small and large scattering angles ($\Theta < 130°$ and $\Theta > 150°$), the underestimation (-17%) and overestimation (27%) of the retrieval in the previous algorithm are reduced to ±8% in the new algorithm over the global land. The reduction of the negative retrievals can be up to 16%-23% for some clean air regions ($\tau_{0.55} < 0.15$). Further, as compared to AERONET measurement, the new retrievals falling within the EE increase to 74.2%, with the increase of 2% and 4.5% than our previous algorithm and C6_DT, respectively.

7.2. Reflection

This thesis is devoted to improving the MODIS-derived AOD (τ) over the dark land surface.

In this study, we contribute to a better understanding of the variation of τ due to different aerosol properties including aerosol type (composed of single scattering albedo ω_0 and phase function P) and their vertical profile. Significant biases in the AOD product can be mainly explained by improper assumptions on aerosol properties. The improper assumption of aerosol type would lead to errors in the AOD retrieval since the TOA reflectance is not accurately simulated due to the use of unrealistic optical properties in modeling scattering and absorption by aerosols. In addition, for an elevated aerosol layer, the TOA reflectance presents lower value due to less isotropic scattering reflected by the Rayleigh layer under the aerosol layer. This becomes more significant for the case of an absorbing and large particle layer since the isotropic scattering is more suppressed. Furthermore, for certain geometrical view and illumination angles, especially at larger viewing angles, high biases in the AOD are caused by improper characterization of the vertical profile.

A further study was to investigate the impact of an aerosol vertical profile on the retrieval using MODIS and CALPSO data. A numeric experiment was carried out to quantify the relationship between the profile and TOA reflectance. It was shown that the mean height of the vertical profile is the main variable that influences the TOA reflectance. As the mean height increases, the TOA reflectance decreases linearly. Therefore, a new algorithm called Gau_DT was developed in which the vertical profile is derived from CALIPSO measurement and parameterized into the RT calculation to yield an accurate TOA reflectance. Over heavy smoke and dust regions (South Africa and the Middle East), a positive difference (3- 5%) Gau_DT-C6_DT AOD was found. This can be used to explain the occurrence of the negative bias of the AOD product over the heavy dust region in the previous study (Levy et al., 2010; Sayer et al., 2013). It also means that the negative bias of the MODIS AOD product can be corrected by our new algorithm.

Another contribution was the analysis of intrinsic errors in the C6_DT algorithm. Through performing the simulation experiment, it was shown that the algorithm always

gives overestimations of the AOD retrieval. We found this is due to the incorrect estimation of the surface reflectance in the retrieval procedure. The intrinsic errors should be further reduced by accurately estimating the surface reflectance in the retrieval. This would further improve the MODIS AOD accuracy.

In addition, this thesis has been devoted to improving the AOD retrieval by considering the anisotropic reflection of the land surface. It is well known that the land surface has anisotropic reflection, i.e., Bidirectional Reflectance Distribution Function (BRDF), which is dependent on the wavelength and the illumination and view angle. We simplified the complicated surface BRDF as: bidirectional, directional-hemispherical, hemispherical-directional, and bihemispherical reflectance, and applied these parameters in the RT process to generate an accurate TOA reflectance. Thus, the background surface contribution is precisely estimated and separated from the TOA reflectance, yielding a better retrieval. In this way, the developed new algorithm has an advantage compared with the previous one where a Lambertian surface (isotropic reflection) is assumed. The validation results show that the regional bias over some regions (e.g, Eastern China and North America) was significantly corrected by the new algorithm. In addition, the AOD data with marginal and better quality becomes available that meets the quality requirements. This means we have more data over the same area.

Finally, this study shows that the angular effects of the AOD retrieval were largely reduced, by refining the relationship of the spectral surface BRF. The Lambertian-based relationship applied in the previous study is not suitable for the surface BRF. In addition, although the relationship varies with surface cover type by considering the vegetation index, this index itself has a directional effect and affects the estimation of the surface reflectance, and finally introduces the uncertainty in the retrieval. This situation has been improved by our study. It was found that the improvement mainly takes effect for light aerosol loading (e.g., North America and global land area, $\tau < 0.15$), where the radiation-field is dominated by the direct radiation since the solar radiation is much less scattered by low-τ atmosphere. The improvement also gives fewer occurrence of the negative retrievals, i.e. more meaningful data can be provided to users.

7.3. Outlook and future perspective

7.3.1. Implication of new aerosol data

A new global map of AOD created in this thesis (Figures 6.6 and 6.7) shows that the overestimation in C6_DT was essentially reduced in the high aerosol loading area (AOD around 0.4), e.g., Middle Africa, India and Eastern China, whereas the underestimation (e.g., negative values) was corrected in the light aerosol loading area (AOD around 0.05), e.g., Brazil and Australia. For example, the positive bias was reduced by about 15% (from 0.059 to 0.001) over Eastern China. This new map can greatly benefit the communities in monitoring air quality, estimating radiative forcing, as well as data assimilation studies that are used for forecasts and climate change and trend.

To predict the surface level PM2.5 concentration, more accurate data including fewer occurrence of negative values can effectively reduce the troubles and problems (e.g., unreliable data over few AERONET site) brought by the retrieval with multi-source data and calibration with AERONET data applied, but would be expected to give the same accu-

racy or even higher in the prediction. The performance of data assimilation for trend analysis and forecasts can be greatly enhanced using this new data as some unknown artificial errors introduced by using empirical corrections described in Zhang and Reid (2006) can be removed. For the estimate of direct radiative forcing following the method in Anderson et al. (2005) and Levy (2007), this new map can improve accuracy by up 15% on regional scale when aerosol loading is << 1.0. Particularly, the AOD data with full quality (QA123) in this study can give much larger coverage (50%) than the operational products, which can significantly reduce problems of data gaps. Additional information on aerosol layer height provided by the algorithm can help the understanding the AOD-PM2.5 relationship in monitoring air quality. This data to some degree can also meet the need for detailed information on atmospheric aerosol such as vertical profile (GCOS, 2011, 2016), to better understand and quantify their impacts.

7.3.2. Applying the aerosol retrieval algorithm to other sensors

The BRF_DT2 algorithm is an adaptation of DT algorithm, which retrieves aerosol (τ and η) and surface properties (ρ^s) over a dark surface with the observations at three channels. This algorithm relies on a few assumptions and the prior knowledge on the spectral surface reflectance. Specifically, the algorithm needs the observations at two visible bands that contain large signals from atmospheric aerosol scattering and small signals from the surface. These observations can be effectively used to retrieve aerosol properties. The algorithm also needs the observation at a longer wavelength that mainly contains the signals from the surface. In addition, prior knowledge of the spectral surface reflectance between the two short wavelengths and the long wavelength should be available. Based on this, we would say yes for Terra since it has the same channels as Aqua. The algorithm can be also applied to MODIS-like sensors VIIRS. It may be applicable to sensors carried by the Sentinel satellites, e.g., MSI on S2. It may not be possible for AASTR instrument since this instrument does not have a similar long wavelength as MODIS, although AASTR does have a bi-angular view (useful for BRDF) and a SWIR channel at a shorter wavelength.

7.3.3. Shortages and future plan

This research dealt with several issues and has shown the improvement of the AOD retrieval with MODIS measurement. Suffering the complexity of the retrieval over the land surface, many efforts still need to be done in the following domains.

- The assumption of the nearly-transparent atmosphere at 2.11 μm may not hold well when a thick aerosol layer is observed (Chapter 5). The atmosphere becomes semi-transparent and turbid since the solar radiation at this wavelength can be significantly scattered due to the thick aerosol layers. This assumption should be replaced by a better or less stringent one for the development of the aerosol retrieval algorithm.

- There is still an ill-posed problem (measurements fewer than unknowns) in our research, although we have integrated Lidar detection sensor CALIPSO (belonging to A-train constellation) with MODIS measurement to consider the aerosol vertical profile in the AOD retrieval. A number of parameters need to be constrained espe-

cially the parameters of the surface reflection, such as three terms of surface BRDF/albedo provided by MODIS MCD43A1 BRDF/product (black-sky and white-sky albedo) and the empirical relationship for the spectral surface BRF derived from ASRVN dataset. Errors from these products or datasets can propagate into the isolation process of surface and aerosol contribution and in turn the AOD retrievals. A new approach should be developed to reduce the uncertainty of the AOD retrieval using multiple retrievals (more than 3) and optimization retrieval technique.

- Although the layer height inferred from CALIPSO data was used to correct the AOD bias due to the elevated aerosol layers and may improve the retrievals for the cases of a long range pollution of dust or smoke, the algorithm is not able to update long-term data over land areas. There are mainly two reasons for that. First, the results with considering the layer height would not be significant over other areas where some other aerosols (non-dust and non-smoke, e.g., urban and industrial emissions) have negligible effects on the Rayleigh scattering below the aerosol layer. Second, there are some limitations to use CALIPSO data including occasional (10 × 10 km) and seasonal (5 × 5 degrees) gridded data. The occasional data that is obtained by assuming the height to be homogeneous across the CALIPSO track and extending it to the wider MODIS swath (2030 km) may not be applicable for the cases that have complex atmospheric conditions such as the atmosphere over rugged mountain areas. In addition, this data may also have a problem of data missing due to cloud mask. The seasonal data that is obtained by averaging the height data over a season may lose some accuracy in the averaging process and cannot be applied in real-time scale.

- The errors due to the improper aerosol type can be corrected using real aerosol type information from CALIPSO VFM data which obtain aerosol type by using the extinction coefficients. Taking account this information into the algorithm, there would be a similar problem as the layer height that needs to assume the homogeneity of aerosol sources. In addition, to be consistent with the MODIS algorithm, aerosol type knowledge from CALIPSO data should be built on the same model as the algorithm does, such as the same size distribution and complex refractive index.

- This thesis focused on the retrieval limited to the dark land surface. Generally, the dark land surface is vegetated area (e.g., forest, grass or black soil), this excludes other bright land surface such as deserts and urban area. To achieve the retrieval globally, a future study could be done over bright areas.

- The AOD product with high spatial resolution (e.g., 3 km × 3 km pixel) should be developed for fine scientific research such as monitoring the air quality in cities, while the produced AOD (10 km × 10 km) by our algorithm may not meet this demand.

A

Aerosol size distribution

We give a brief review of the aerosol size distribution that applied in the MODIS AOD algorithm (Levy et al., 2007a). For any size distribution, the particles number N related to area A and volume V distributions are:

$$\frac{dN}{d\ln r} = \frac{1}{\pi r^2}\frac{dA}{d\ln r} = \frac{3}{4\pi r^3}\frac{dV}{d\ln r}, \tag{A.1}$$

where $dN/d\ln r$ is the number size distribution, with the radius r in μm. In the MODIS C6_DT algorithm over land, the aerosol models are assumed with bi-lognomal distribution. For the size distribution, each lognormal mode has 3 free variables, including the median radius of the volume size distribution r_v (μm in unit), the standard deviation of the radius σ, and the volume of particles per cross section of atmospheric column V_0 ($\mu m^3/\mu m^2$ in unit). Thus, for each single lognormal mode, the number size distribution is represented as:

$$\frac{dN}{d\ln r} = \frac{N_0}{\sigma\sqrt{2\pi}}\exp(-\frac{\ln(r/r_g)^2}{2\sigma^2}), \tag{A.2}$$

where r_g and N_0 are the median radius and the amplitude of the number size distribution, respectively, defined as:

$$\begin{aligned} r_g &= r_v\exp(-3\sigma^2) \\ N_0 &= \int \frac{dN}{d\ln r}d\ln r = V_0\frac{3}{4\pi r_g^3}\exp(-\frac{9}{2}\sigma^2) \end{aligned} \tag{A.3}$$

The effective radius r_{eff} in μm of a lognormal mode is given as:

$$r_{eff} = \frac{\int_0^\infty r^3\frac{dN}{d\ln r}d\ln r}{\int_0^\infty r^2\frac{dN}{d\ln r}d\ln r} = r_g\exp(\frac{5}{2}\sigma^2) \tag{A.4}$$

For lognormal bimodal (1 and 2 for accumulative and coarse mode, respectively), the total number size distribution is:

$$\frac{dN}{d\ln r} = \frac{dN_1}{d\ln r} + \frac{dN_2}{d\ln r}, \tag{A.5}$$

And the corresponding effective radius can be written as:

$$r_{eff} = \frac{\int_0^\infty r^3\frac{dN_1+dN_2}{d\ln r}d\ln r}{\int_0^\infty r^2\frac{dN_1+dN_2}{d\ln r}d\ln r} \tag{A.6}$$

B

The TOA reflectance coupling with non-Lambertian surface

The TOA reflectance coupling with surface BRDF was originally proposed by Li et al. (1996), and further applied by Qin et al. (2001) (equation 5.1), and Yang et al. (2014). Here we basically follow the idea of Li et al. (1996), but deduce the calculation of TOA reflectance in a more rigorous way and correct some errors in Li et al. (1996); Yang et al. (2014).

According to the four-stream radiation theory (Verhoef, 1985), the radiation field of upper (or lower) boundary of atmosphere can be view as four components: directional flux F^+ and F^-, hemispherical flux E^+ and E^- (lower boundary: F_+ and F_-,and E_+ and E_-). The symbol of "+" and "−" means the up and down direction for flux. Note the position of "+" and "−" in F or E.

(1) Assuming ideal black surface below the atmosphere, the upper atmospheric reflectance (up direction) are:

$$\sigma^+_{dd} = \frac{\delta F^+}{\delta F^-}, \sigma^+_{dh} = \frac{\delta E^+}{\delta F^-}, \tag{B.1}$$

where δ indicates infinitesimal quantity. The lower atmospheric reflectance (down direction) are similar to:

$$\begin{aligned} \sigma_{-dd} &= \frac{\delta F_-}{\delta F_+}, \sigma_{-dh} = \frac{\delta E_-}{\delta F_+} \\ \sigma_{-hd} &= \frac{\delta F_-}{\delta E_+}, \sigma_{-hh} = \frac{\delta E_-}{\delta E_+} \end{aligned} \tag{B.2}$$

The ratios of the flux after upward-transmitting the whole atmospheric layer to the upward-incident flux at lower atmosphere (also called atmosphere transmittance) are:

$$\begin{aligned} t^+_{dd} &= \frac{\delta F^+}{\delta F_+}, t^+_{dh} = \frac{\delta E^+}{\delta F_+} \\ t^+_{hd} &= \frac{\delta F^+}{\delta E_+}, t^+_{hh} = \frac{\delta E^+}{\delta E_+} \end{aligned} \tag{B.3}$$

The ratios of the flux after upward-transmitting the whole atmospheric layer to the downward-incident flux at upper atmosphere are:

$$t_{-dd} = \frac{\delta F_-}{\delta F^-}, t_{-dh} = \frac{\delta E_-}{\delta F^-} \tag{B.4}$$

(2) The surface reflectance are defined as:

$$R_{dd} = \frac{\delta F_+}{\delta F_-}, R_{dh} = \frac{\delta E_+}{\delta F_-}$$
$$R_{hd} = \frac{\delta F_+}{\delta E_-}, R_{hh} = \frac{\delta E_+}{\delta E_-} \tag{B.5}$$

More details about these four parameters, please refer to Schaepman-Strub et al. (2006) (case 1, 3, 7, and 9).

Ignoring the effect of atmospheric gas absorption and the impact of neighborhood surface, the flux received by sensor (higher than TOA level) is:

$$F^+(i,v) = F^-(i) \cdot \sigma^+_{dd}(i,v) + F_+(i,v) \cdot t^+_{dd}(v) + E_+ \cdot t^+_{hd}(v) \tag{B.6}$$

Since the transmitted flux is the same as the incident flux, there is $t_{dd}(v,v) = t_{dd}(i,v)$. We use $t_{dd}(v)$ to present $t_{dd}(i,v)$. Two fluxes are unknown in equation B.6. They are F_+ and E_+. To get the explicit expressions of these two fluxes, the radiation field in the lower atmosphere is introduced, where we have four fluxes F_-, F_+, E_- and E_+:

$$F_-(i) = F^-(i) \cdot t_{-dd}(i) \tag{B.7}$$
$$F_+(i,v) = F_-(i) \cdot R_{dd}(i,v) + E_- \cdot R_{hd}(v) \tag{B.8}$$
$$E_- = F^-(i) \cdot t_{-dh}(i) + E_+ \cdot \sigma_{-hh} \tag{B.9}$$
$$E_+ = F_-(i) \cdot R_{dh}(i) + E_- \cdot R_{hh} \tag{B.10}$$

In this radiation field (equations B.7-B.10), the multiple bounces between the atmosphere and the surface are neglected for directional flux F due to the weak directional reflection of the lower atmosphere (σ_{-dd}, σ_{-dh}, and σ_{-hd}). For instance, addition term of $E_+\sigma_{hd}$ is removed on the right side of B.7. But we take account of the multiple bounces for hemispherical flux E.

Combine equation B.9 and B.10, then we get E_+:

$$E_+ = \frac{F_-(i) \cdot R_{dh}(i) + F^-(i) \cdot t_{-dh}(i) \cdot R_{hh}}{1 - \sigma_{-hh} \cdot R_{hh}} \tag{B.11}$$

Substitute equation B.11 into equation B.9, E_- is solved, then F_+.

Now, we go back to calculate the direction flux received by viewer/sensor (equation B.6), by substituting equation B.7, B.8, B.9 and B.10 into it. Note some directions $(i,\ v)$ are not explicitly shown.

$$\begin{aligned} F^+ &= F^- \cdot \sigma^+_{dd} + F_+ \cdot t^+_{dd}(v) + E_+ \cdot t^+_{hd}(v) \\ &= F^- \cdot \sigma^+_{dd} \\ &\quad + F^- \left\{ \begin{bmatrix} t_{-dd}(i) & t_{-dh}(i) \end{bmatrix} \begin{bmatrix} R_{dd} & R_{dh} \\ R_{hd} & R_{hh} \end{bmatrix} \begin{bmatrix} t^+_{dd}(v) \\ t^+_{hd}(v) \end{bmatrix} \right\} \\ &\quad + F^- \left\{ \frac{\begin{bmatrix} t_{-dd}(i) & t_{-dh}(i) \end{bmatrix} \begin{bmatrix} R_{dh} \\ R_{hh} \end{bmatrix} \begin{bmatrix} R_{hd} & R_{hh} \end{bmatrix} \begin{bmatrix} t^+_{dd}(v) \\ t^+_{hd}(v) \end{bmatrix} \sigma_{-hh}}{1 - R_{hh} \cdot \sigma_{-hh}} \right\} \end{aligned} \tag{B.12}$$

Rewrite equation B.12 with matrix form (matrices defined in equation 5.2, some "+−" are not explicitly shown),

$$F^{+} = F^{-} \cdot \sigma^{+}_{dd} + F^{-} \cdot \frac{\mathbf{T}(i)\mathbf{RT}(v) - t_{dd}(i) \cdot \left|\mathbf{R}\right| \cdot t_{dd}(v) \cdot \sigma_{-hh}}{1 - R_{hh} \cdot \sigma_{-hh}} \tag{B.13}$$

Bibliography

Abdou, W. A., Martonchik, J. V., Kahn, R. A., West, R. A., and Diner, D. J. (1997). A modified linear-mixing method for calculating atmospheric path radiances of aerosol mixtures. *Journal of Geophysical Research: Atmospheres*, 102(D14):16883–16888.

Acharya, P. K., Berk, A., Anderson, G. P., Anderson, G. P., Larsen, N. F., Tsay, S. C., and Stamnes, K. H. (1999). MODTRAN4: multiple scattering and bidirectional reflectance distribution function (BRDF) upgrades to MODTRAN. volume 3756, pages 354–362.

Ackerman, S., Frey, R., Strabala, K. I., Liu, Y., Gumley, L., Baum, B. A., and Menzel, W. P. (2010). Discriminating clear-sky from cloud with MODIS: algorithm theoretical basis document (MOD35), 6th Edn. *University of Wisconsin-Madison*.

Ackerman, S. A., Strabala, K. I., Menzel, W. P., Frey, R. A., Moeller, C. C., and Gumley, L. E. (1998). Discriminating clear sky from clouds with MODIS. *Journal of Geophysical Research: Atmospheres*, 103(D24):32141–32157.

Anderson, T. L., Charlson, R. J., Bellouin, N., Boucher, O., Chin, M., Christopher, S. A., Haywood, J., Kaufman, Y. J., Kinne, S., Ogren, J. A., Remer, L. A., Takemura, T., Tanré, D., Torres, O., Trepte, C. R., Wielicki, B. A., Winker, D. M., and Yu, H. (2005). An "A-Train" Strategy for Quantifying Direct Climate Forcing by Anthropogenic Aerosols. *Bulletin of the American Meteorological Society*, 86(12):1795–1809.

Bellouin, N., Jones, A., Haywood, J., and Christopher, S. A. (2008). Updated estimate of aerosol direct radiative forcing from satellite observations and comparison against the Hadley Centre climate model. *Journal of Geophysical Research: Atmospheres*, 113(D10):D10205.

Berk, A., Anderson, G. P., Bernstein, L. S., Acharya, P. K., Dothe, H., Matthew, M. W., Adler-Golden, S. M., Chetwynd, James H., J., Richtsmeier, S. C., Pukall, B., Allred, C. L., Jeong, L. S., and Hoke, M. L. (1999). MODTRAN4 radiative transfer modeling for atmospheric correction. volume 3756, pages 348–353.

Chin, M., Diehl, T., Tan, Q., Prospero, J. M., Kahn, R. A., Remer, L. A., Yu, H., Sayer, A. M., Bian, H., Geogdzhayev, I. V., Holben, B. N., Howell, S. G., Huebert, B. J., Hsu, N. C., Kim, D., Kucsera, T. L., Levy, R. C., Mishchenko, M. I., Pan, X., Quinn, P. K., Schuster, G. L., Streets, D. G., Strode, S. A., Torres, O., and Zhao, X.-P. (2014). Multi-decadal aerosol variations from 1980 to 2009: a perspective from observations and a global model. *Atmos. Chem. Phys.*, 14(7):3657–3690.

Chu, D. A., Kaufman, Y. J., Zibordi, G., Chern, J. D., Mao, J., Li, C., and Holben, B. N. (2003). Global monitoring of air pollution over land from the Earth Observing System-Terra Moderate Resolution Imaging Spectroradiometer (MODIS). *Journal of Geophysical Research: Atmospheres*, 108(D21):4661.

Crutzen, P. J. and Andreae, M. O. (1990). Biomass Burning in the Tropics: Impact on Atmospheric Chemistry and Biogeochemical Cycles. *Science*, 250(4988):1669–1678.

de Graaf, M. (2006). Remote Sensing of UV-absorbing aerosols using space-borne spectrometers. *Phd Thesis, Free University, Amsterdam*, section 6, chapter 1.

Dubovik, O., Herman, M., Holdak, A., Lapyonok, T., Taure, D., Deuze, J. L., Ducos, F., and Sinyuk, A. (2011). Statistically Optimized Inversion Algorithm for Enhanced Retrieval of Aerosol Properties from Spectral Multi-Angle Polarimetric Satellite Observations. *Atmospheric Measurement Techniques*, 4:975–1018.

Dubovik, O., Holben, B., Eck, T. F., Smirnov, A., Kaufman, Y. J., King, M. D., Tanré, D., and Slutsker, I. (2002a). Variability of Absorption and Optical Properties of Key Aerosol Types Observed in Worldwide Locations. *Journal of the Atmospheric Sciences*, 59(3):590–608.

Dubovik, O., Holben, B. N., Lapyonok, T., Sinyuk, A., Mishchenko, M. I., Yang, P., and Slutsker, I. (2002b). Non-spherical aerosol retrieval method employing light scattering by spheroids. *Geophysical Research Letters*, 29(10):1415.

Dubovik, O., Sinyuk, A., Lapyonok, T., Holben, B. N., Mishchenko, M., Yang, P., Eck, T. F., Volten, H., Muñoz, O., and Veihelmann, B. (2006). Application of spheroid models to account for aerosol particle nonsphericity in remote sensing of desert dust. *Journal of Geophysical Research*, 111(D11):D11208.

Eck, T. F., Holben, B. N., Reid, J. S., Mukelabai, M. M., Piketh, S. J., Torres, O., Jethva, H. T., Hyer, E. J., Ward, D. E., Dubovik, O., Sinyuk, A., Schafer, J. S., Giles, D. M., Sorokin, M., Smirnov, A., and Slutsker, I. (2013). A seasonal trend of single scattering albedo in southern African biomass-burning particles: Implications for satellite products and estimates of emissions for the world's largest biomass-burning source. *Journal of Geophysical Research: Atmospheres*, 118(12):6414–6432.

Engel-Cox, J. A., Holloman, C. H., Coutant, B. W., and Hoff, R. M. (2004). Qualitative and quantitative evaluation of MODIS satellite sensor data for regional and urban scale air quality. *Atmospheric Environment*, 38(16):2495–2509.

Evans, K. F. and Stephens, G. L. (1991). A new polarized atmospheric radiative transfer model. *Journal of Quantitative Spectroscopy and Radiative Transfer*, 46(5):413–423.

Gatebe, C., King, M., Tsay, S.-C., Ji, Q., Arnold, G., and Li, J. (2001). Sensitivity of off-nadir zenith angles to correlation between visible and near-infrared reflectance for use in remote sensing of aerosol over land. *IEEE Transactions on Geoscience and Remote Sensing*, 39(4):805–819.

GCOS (2007). GCOS AOPC/TOPC Joint Working Group on Land-Surface/Atmosphere Issues (WG-LSA). Technical report, Report from the meeting at EC Joint Research Centre, Ispra (VA), Italy.

GCOS (2011). Systematic observation requirements for satellite-based products for climate, 2011 update. WMO GCOS Report. 154, New York, USA.

GCOS (2016). The Global Observing System for Climate: Implementation Needs. Report, WMO, Gauyaquil, Ecuador.

Giglio, L., Csiszar, I., and Justice, C. O. (2006). Global distribution and seasonality of active fires as observed with the Terra and Aqua Moderate Resolution Imaging Spectroradiometer (MODIS) sensors. *Journal of Geophysical Research: Biogeosciences*, 111(G2):G02016.

Grey, W. M. F., North, P. R. J., Los, S. O., and Mitchell, R. M. (2006). Aerosol optical depth and land surface reflectance from multiangle AATSR measurements: global validation and intersensor comparisons. *Geoscience and Remote Sensing, IEEE Transactions on*, 44(8):2184–2197.

Guenther, B., Xiong, X., Salomonson, V. V., Barnes, W. L., and Young, J. (2002). On-orbit performance of the Earth Observing System Moderate Resolution Imaging Spectroradiometer; first year of data. *Remote Sensing of Environment*, 83(1–2):16–30.

Guo, J., He, J., Liu, H., Miao, Y., Liu, H., and Zhai, P. (2016a). Impact of various emission control schemes on air quality using WRF-Chem during APEC China 2014. *Atmospheric Environment*, 140:311–319.

Guo, J., Xia, F., Zhang, Y., Liu, H., Li, J., Lou, M., He, J., Yan, Y., Wang, F., Min, M., and Zhai, P. (2016b). Impact of diurnal variability and meteorological factors on the PM2.5 - AOD relationship: Implications for PM2.5 remote sensing. *Environmental Pollution*.

Guo, J.-P., Zhang, X.-Y., Wu, Y.-R., Zhaxi, Y., Che, H.-Z., La, B., Wang, W., and Li, X.-W. (2011). Spatio-temporal variation trends of satellite-based aerosol optical depth in China during 1980–2008. *Atmospheric Environment*, 45(37):6802–6811.

Gupta, P., Christopher, S. A., Wang, J., Gehrig, R., Lee, Y., and Kumar, N. (2006). Satellite remote sensing of particulate matter and air quality assessment over global cities. *Atmospheric Environment*, 40(30):5880–5892.

Henyey, L. G. and Greenstein, J. L. (1941). Diffuse radiation in the Galaxy. *The Astrophysical Journal*, 93:70–83.

Herman, M., Deuzé, J.-L., Marchand, A., Roger, B., and Lallart, P. (2005). Aerosol remote sensing from POLDER/ADEOS over the ocean: Improved retrieval using a nonspherical particle model. *Journal of Geophysical Research: Atmospheres*, 110(D10):D10S02.

Hoff, R. M. and Christopher, S. A. (2009). Remote Sensing of Particulate Pollution from Space: Have We Reached the Promised Land? *Journal of the Air & Waste Management Association*, 59(6):645–675.

Hostetler, C. A., Liu, Z., Reagan, J., Vaughan, M., Winker, D., Osborne, M., Hunt, W. H., Powell, K. A., and Trepte, C. (2008). CALIOP Algorithm Theoretical Basis Document: Calibration and Level 1 Data Products.

Hsu, N. C., Jeong, M.-J., Bettenhausen, C., Sayer, A. M., Hansell, R., Seftor, C. S., Huang, J., and Tsay, S.-C. (2013). Enhanced Deep Blue aerosol retrieval algorithm: The second generation. *Journal of Geophysical Research: Atmospheres*, 118(16):9296–9315.

Hsu, N. C., Tsay, S.-C., King, M. D., and Herman, J. R. (2004). Aerosol properties over bright-reflecting source regions. *IEEE Transactions on Geoscience and Remote Sensing*, 42(3):557–569.

Hsu, N. C., Tsay, S. C., King, M. D., and Herman, J. R. (2006). Deep Blue Retrievals of Asian Aerosol Properties During ACE-Asia. *IEEE Transactions on Geoscience and Remote Sensing*, 44(11):3180–3195.

Huang, J., Guo, J., Wang, F., Liu, Z., Jeong, M.-J., Yu, H., and Zhang, Z. (2015). CALIPSO inferred most probable heights of global dust and smoke layers. *Journal of Geophysical Research: Atmospheres*, 120(10):2014JD022898.

Hutchison, K. D., Faruqui, S. J., and Smith, S. (2008). Improving correlations between MODIS aerosol optical thickness and ground-based PM2.5 observations through 3d spatial analyses. *Atmospheric Environment*, 42(3):530–543.

Hyer, E. J., Reid, J. S., and Zhang, J. (2011). An over-land aerosol optical depth data set for data assimilation by filtering, correction, and aggregation of MODIS Collection 5 optical depth retrievals. *Atmos. Meas. Tech.*, 4(3):379–408.

IPCC (2013). Working Group I Contribution to the IPCC Fifth Assessment Report (AR5) Climate Change 2013: The Physical Science Basis. *Intergovernmental Panel on Climate Change, Geneva, Switzerland*.

Kaufman, Y. J., Tanré, D., and Boucher, O. (2002). A satellite view of aerosols in the climate system. *Nature*, 419(6903):215–223.

Kaufman, Y. J., Tanré, D., Remer, L. A., Vermote, E. F., Chu, A., and Holben, B. N. (1997). Operational remote sensing of tropospheric aerosol over land from EOS moderate resolution imaging spectroradiometer. *Journal of Geophysical Research: Atmospheres*, 102(D14):17051–17067.

Keller, J., Bojinski, S., and Prevot, A. S. H. (2007). Simultaneous retrieval of aerosol and surface optical properties using data of the Multi-angle Imaging SpectroRadiometer (MISR). *Remote Sensing of Environment*, 107(1–2):120–137.

Koelemeijer, R. B. A., Homan, C. D., and Matthijsen, J. (2006). Comparison of spatial and temporal variations of aerosol optical thickness and particulate matter over Europe. *Atmospheric Environment*, 40(27):5304–5315.

Kokhanovsky, A. (2008). *Aerosol Optics - Light Absorption and Scattering by Particles in the Atmosphere*|. Springer.

Kokhanovsky, A. A., Deuzé, J. L., Diner, D. J., Dubovik, O., Ducos, F., Emde, C., Garay, M. J., Grainger, R. G., Heckel, A., Herman, M., Katsev, I. L., Keller, J., Levy, R., North, P. R. J., Prikhach, A. S., Rozanov, V. V., Sayer, A. M., Ota, Y., Tanré, D., Thomas, G. E., and Zege,

E. P. (2010). The inter-comparison of major satellite aerosol retrieval algorithms using simulated intensity and polarization characteristics of reflected light. *Atmos. Meas. Tech.*, 3(4):909–932.

Kotchenova, S. Y. and Vermote, E. F. (2007). A vector version of the 6s radiative transfer code for atmospheric correction of satellite data: an Overview. In *29th Review of Atmospheric Transmission Models Meeting, Lexington, Mass., USA,(13–14 June 2007)*.

Kotchenova, S. Y., Vermote, E. F., Levy, R., and Lyapustin, A. (2008). Radiative transfer codes for atmospheric correction and aerosol retrieval: intercomparison study. *Applied optics*, 47(13):2215–2226.

Kuznetsov, A., Melnikova, I., Pozdnyakov, D., Seroukhova, O., and Vasilyev, A. (2012). *Remote Sensing of the Environment and Radiation Transfer: An Introductory Survey*. Springer Science & Business Media. Google-Books-ID: mVrNwZNiHXIC.

Laden, F., Neas, L. M., Dockery, D. W., and Schwartz, J. (2000). Association of fine particulate matter from different sources with daily mortality in six U.S. cities. *Environmental Health Perspectives*, 108(10):941–947.

Lee, J., Hsu, N. C., Bettenhausen, C., Sayer, A. M., Seftor, C. J., and Jeong, M.-J. (2015). Retrieving the height of smoke and dust aerosols by synergistic use of VIIRS, OMPS, and CALIOP observations. *Journal of Geophysical Research: Atmospheres*, 120(16):2015JD023567.

Levy, R. C. (2007). Retrieval of tropospheric aerosol properties over land from inversion of visible and near-infrared spectral reflectance: application over maryland. *Dissertation (NASA)*, Section 2, Chapter 9.

Levy, R. C., Mattoo, S., Munchak, L. A., Remer, L. A., Sayer, A. M., and Hsu, N. C. (2013a). The Collection 6 MODIS aerosol products over land and ocean. *Atmos. Meas. Tech. Discuss.*, 6(1):159–259.

Levy, R. C., Mattoo, S., Munchak, L. A., Remer, L. A., Sayer, A. M., Patadia, F., and Hsu, N. C. (2013b). The Collection 6 MODIS aerosol products over land and ocean. *Atmos. Meas. Tech.*, 6(11):2989–3034.

Levy, R. C., Remer, L. A., and Dubovik, O. (2007a). Global aerosol optical properties and application to Moderate Resolution Imaging Spectroradiometer aerosol retrieval over land. *Journal of Geophysical Research: Atmospheres*, 112(D13):D13210.

Levy, R. C., Remer, L. A., and Kaufman, Y. J. (2004). Effects of neglecting polarization on the MODIS aerosol retrieval over land. *IEEE Transactions on Geoscience and Remote Sensing*, 42(11):2576–2583.

Levy, R. C., Remer, L. A., Kleidman, R. G., Mattoo, S., Ichoku, C., Kahn, R., and Eck, T. F. (2010). Global evaluation of the Collection 5 MODIS dark-target aerosol products over land. *Atmos. Chem. Phys.*, 10(21):10399–10420.

Levy, R. C., Remer, L. A., Martins, J. V., Kaufman, Y. J., Plana-Fattori, A., Redemann, J., and Wenny, B. (2005). Evaluation of the MODIS Aerosol Retrievals over Ocean and Land during CLAMS. *Journal of the Atmospheric Sciences*, 62(4):974–992.

Levy, R. C., Remer, L. A., Mattoo, S., Vermote, E. F., and Kaufman, Y. J. (2007b). Second-generation operational algorithm: Retrieval of aerosol properties over land from inversion of Moderate Resolution Imaging Spectroradiometer spectral reflectance. *Journal of Geophysical Research: Atmospheres*, 112(D13):D13211.

Li, X., Wang, J., Ni, W., Strahler, A., and Woodcock, C. (1996). Simulation of path scattering and multiple bounces of photons between two media (in Chinese). *Sci. China (Series E)*, 26:457–466.

Li, Z., Zhao, X., Kahn, R., Mishchenko, M., Remer, L., Lee, K.-H., Wang, M., Laszlo, I., Nakajima, T., and Maring, H. (2009). Uncertainties in satellite remote sensing of aerosols and impact on monitoring its long-term trend: a review and perspective. *Ann. Geophys.*, 27(7):2755–2770.

Liang, S. (2003). *Quantitative remote sensing of land surfaces*, volume 23. Wiley-Interscience.

Liou, K. N. (2002). *An Introduction to Atmospheric Radiation.* Academic Press.

Liu, D., Wang, Z., Liu, Z., Winker, D., and Trepte, C. (2008a). A height resolved global view of dust aerosols from the first year CALIPSO lidar measurements. *Journal of Geophysical Research: Atmospheres*, 113(D16):D16214.

Liu, Y., Franklin, M., Kahn, R., and Koutrakis, P. (2007). Using aerosol optical thickness to predict ground-level PM2.5 concentrations in the St. Louis area: A comparison between MISR and MODIS. *Remote Sensing of Environment*, 107:33–44.

Liu, Z., Liu, Q., Lin, H.-C., Schwartz, C. S., Lee, Y.-H., and Wang, T. (2011). Three-dimensional variational assimilation of MODIS aerosol optical depth: Implementation and application to a dust storm over East Asia. *Journal of Geophysical Research: Atmospheres*, 116(D23):D23206.

Liu, Z., Omar, A., Vaughan, M., Hair, J., Kittaka, C., Hu, Y., Powell, K., Trepte, C., Winker, D., Hostetler, C., Ferrare, R., and Pierce, R. (2008b). CALIPSO lidar observations of the optical properties of Saharan dust: A case study of long-range transport. *Journal of Geophysical Research: Atmospheres*, 113(D7):D07207.

Liu, Z., Omar, A. H., Hu, Y., Vaughan, M. A., and Winker, D. M. (2005). CALIOP Algorithm Theoretical Basis Document Part 3 : Scene Classification Algorithms.

Lucht, W., Schaaf, C., and Strahler, A. (2000). An algorithm for the retrieval of albedo from space using semiempirical BRDF models. *IEEE Transactions on Geoscience and Remote Sensing*, 38(2):977–998.

Lyapustin, A. and Knyazikhin, Y. (2001). Green's function method for the radiative transfer problem. I. Homogeneous non-Lambertian surface. *Applied Optics*, 40(21):3495–3501.

Lyapustin, A., Martonchik, J., Wang, Y., Laszlo, I., and Korkin, S. (2011a). Multiangle implementation of atmospheric correction (MAIAC): 1. Radiative transfer basis and look-up tables. *Journal of Geophysical Research: Atmospheres*, 116(D3):D03210.

Lyapustin, A., Wang, Y., Laszlo, I., Kahn, R., Korkin, S., Remer, L., Levy, R., and Reid, J. S. (2011b). Multiangle implementation of atmospheric correction (MAIAC): 2. Aerosol algorithm. *Journal of Geophysical Research: Atmospheres*, 116(D3):D03211.

Lyapustin, A. I. (2005). Radiative transfer code SHARM for atmospheric and terrestrial applications. *Applied Optics*, 44(36):7764–7772.

Lyapustin, A. I., Wang, Y., Laszlo, I., Hilker, T., G.Hall, F., Sellers, P. J., Tucker, C. J., and Korkin, S. V. (2012). Multi-angle implementation of atmospheric correction for MODIS (MAIAC): 3. Atmospheric correction. *Remote Sensing of Environment*, 127:385–393.

Martins, J. V., Tanré, D., Remer, L., Kaufman, Y., Mattoo, S., and Levy, R. (2002). MODIS Cloud screening for remote sensing of aerosols over oceans using spatial variability. *Geophysical Research Letters*, 29(12):MOD4–1.

Martonchik, J., Diner, D., Crean, K., and Bull, M. (2002). Regional aerosol retrieval results from MISR. *IEEE Transactions on Geoscience and Remote Sensing*, 40(7):1520–1531.

Martonchik, J. V., Diner, D. J., Kahn, R. A., Ackerman, T. P., Verstraete, M. M., Pinty, B., and Gordon, H. R. (1998). Techniques for the retrieval of aerosol properties over land and ocean using multiangle imaging. *IEEE Transactions on Geoscience and Remote Sensing*, 36(4):1212–1227.

Martonchik, J. V., Kahn, R. A., and Diner, D. J. (2009). Retrieval of aerosol properties over land using MISR observations. In *Satellite Aerosol Remote Sensing over Land*, pages 267–293. Springer.

McComiskey, A., Schwartz, S. E., Schmid, B., Guan, H., Lewis, E. R., Ricchiazzi, P., and Ogren, J. A. (2008). Direct aerosol forcing: Calculation from observables and sensitivities to inputs. *Journal of Geophysical Research: Atmospheres*, 113(D9):D09202.

Meyer, D., Verstraete, M., and Pinty, B. (1995). The effect of surface anisotropy and viewing geometry on the estimation of NDVI from AVHRR. *Remote Sensing Reviews*, 12(1-2):3–27.

Mie, G. (1908). Beiträge zur Optik trüber Medien, speziell kolloidaler Metallösungen. *Annalen der Physik*, 330(3):377–445.

Mishchenko, M. I., Geogdzhayev, I. V., Cairns, B., Rossow, W. B., and Lacis, A. A. (1999). Aerosol retrievals over the ocean by use of channels 1 and 2 AVHRR data: sensitivity analysis and preliminary results. *Applied Optics*, 38(36):7325.

Mishchenko, M. I. and Travis, L. D. (1994). T-matrix computations of light scattering by large spheroidal particles. *Optics Communications*, 109(1):16–21.

Myhre, G. (2009). Consistency Between Satellite-Derived and Modeled Estimates of the Direct Aerosol Effect. *Science*, 325(5937):187–190.

Nicolantonio., W. D., ., A. C., Bolzacchini., E., Ferrero., L., Volta., M., and Pisoni, E. (2007). MODIS Aerosol Optical Properties Over North Italy For Estimating Surface-Level PM2.5. *Envisat Symposium 2007*, pages 3–27.

North, P. R. J. (2002). Estimation of aerosol opacity and land surface bidirectional reflectance from ATSR-2 dual-angle imagery: Operational method and validation. *Journal of Geophysical Research: Atmospheres*, 107(D12):AAC 4–1.

North, P. R. J., Briggs, S. A., Plummer, S. E., and Settle, J. J. (1999). Retrieval of land surface bidirectional reflectance and aerosol opacity from ATSR-2 multiangle imagery. *IEEE Transactions on Geoscience and Remote Sensing*, 37(1):526–537.

Omar, A. H., Won, J.-G., Winker, D. M., Yoon, S.-C., Dubovik, O., and McCormick, M. P. (2005). Development of global aerosol models using cluster analysis of Aerosol Robotic Network (AERONET) measurements. *Journal of Geophysical Research: Atmospheres*, 110(D10):D10S14.

Petrenko, M., Ichoku, C., and Leptoukh, G. (2012). Multi-sensor Aerosol Products Sampling System (MAPSS). *Atmos. Meas. Tech.*, 5(5):913–926.

Pinty, B., Lattanzio, A., Martonchik, J. V., Verstraete, M. M., Gobron, N., Taberner, M., Widlowski, J.-L., Dickinson, R. E., and Govaerts, Y. (2005). Coupling Diffuse Sky Radiation and Surface Albedo. *Journal of the Atmospheric Sciences*, 62(7):2580–2591.

Pinty, B., Lavergne, T., Dickinson, R. E., Widlowski, J.-L., Gobron, N., and Verstraete, M. M. (2006). Simplifying the interaction of land surfaces with radiation for relating remote sensing products to climate models. *Journal of Geophysical Research: Atmospheres*, 111(D2):D02116.

Pinty, B., Roveda, F., Verstraete, M. M., Gobron, N., Govaerts, Y., Martonchik, J. V., Diner, D. J., and Kahn, R. A. (2000a). Surface albedo retrieval from Meteosat: 1. Theory. *Journal of Geophysical Research: Atmospheres*, 105(D14):18099–18112.

Pinty, B., Roveda, F., Verstraete, M. M., Gobron, N., Govaerts, Y., Martonchik, J. V., Diner, D. J., and Kahn, R. A. (2000b). Surface albedo retrieval from Meteosat: 2. Applications. *Journal of Geophysical Research: Atmospheres*, 105(D14):18113–18134.

Pinty, B., Taberner, M., Haemmerle, V. R., Paradise, S. R., Vermote, E., Verstraete, M. M., Gobron, N., and Widlowski, J.-L. (2010). Global-Scale Comparison of MISR and MODIS Land Surface Albedos. *Journal of Climate*, 24(3):732–749.

Pope III, C. A., Burnett, R. T., Thun, M. J., Calle, E. E., Krewski, D., Ito, K., and Thurston, G. D. (2002). LUng cancer, cardiopulmonary mortality, and long-term exposure to fine particulate air pollution. *JAMA*, 287(9):1132–1141.

Pope III, C. A. and Dockery, D. W. (2006). Health Effects of Fine Particulate Air Pollution: Lines that Connect. *Journal of the Air & Waste Management Association*, 56(6):709–742.

Prospero, J. M., Ginoux, P., Torres, O., Nicholson, S. E., and Gill, T. E. (2002). Environmental Characterization of Global Sources of Atmospheric Soil Dust Identified with the Nimbus 7 Total Ozone Mapping Spectrometer (toms) Absorbing Aerosol Product. *Reviews of Geophysics*, 40(1):1002.

Qin, W., Herman, J. R., and Ahmad, Z. (2001). A fast, accurate algorithm to account for non-Lambertian surface effects on TOA radiance. *Journal of Geophysical Research: Atmospheres*, 106(D19):22671–22684.

Remer, L. A. and Kaufman, Y. J. (1998). Dynamic aerosol model: Urban/industrial aerosol. *Journal of Geophysical Research: Atmospheres*, 103(D12):13859–13871.

Remer, L. A., Kaufman, Y. J., Holben, B. N., Thompson, A. M., and McNamara, D. (1998). Biomass burning aerosol size distribution and modeled optical properties. *Journal of Geophysical Research: Atmospheres*, 103(D24):31879–31891.

Remer, L. A., Kaufman, Y. J., Tanré, D., Mattoo, S., Chu, D. A., Martins, J. V., Li, R.-R., Ichoku, C., Levy, R. C., Kleidman, R. G., Eck, T. F., Vermote, E., and Holben, B. N. (2005). The MODIS Aerosol Algorithm, Products, and Validation. *Journal of the Atmospheric Sciences*, 62(4):947–973.

Remer, L. A., Tanre, D., Kaufman, Y. J., Levy, R., and Mattoo, S. (2006). Algorithm for remote sensing of tropospheric aerosol from MODIS: Collection 005. *National Aeronautics and Space Administration*.

Rondeaux, G. and Vanderbilt, V. C. (1993). Specularly modified vegetation indices to estimate photosynthetic activity. *International Journal of Remote Sensing*, 14(9):1815–1823.

Saide, P. E., Carmichael, G. R., Liu, Z., Schwartz, C. S., Lin, H. C., da Silva, A. M., and Hyer, E. (2013). Aerosol optical depth assimilation for a size-resolved sectional model: impacts of observationally constrained, multi-wavelength and fine mode retrievals on regional scale analyses and forecasts. *Atmos. Chem. Phys.*, 13(20):10425–10444.

Samet, J. M., Dominici, F., Curriero, F. C., Coursac, I., and Zeger, S. L. (2000). Fine Particulate Air Pollution and Mortality in 20 U.S. Cities, 1987–1994. *New England Journal of Medicine*, 343(24):1742–1749.

Sayer, A. M., Hsu, N. C., Bettenhausen, C., and Jeong, M.-J. (2013). Validation and uncertainty estimates for MODIS Collection 6 Deep Blue aerosol data. *Journal of Geophysical Research: Atmospheres*, 118(14):7864–7872.

Sayer, A. M., Hsu, N. C., Bettenhausen, C., Jeong, M.-J., and Meister, G. (2015). Effect of MODIS Terra radiometric calibration improvements on Collection 6 Deep Blue aerosol products: Validation and Terra/Aqua consistency. *Journal of Geophysical Research: Atmospheres*, 120(23):2015JD023878.

Sayer, A. M., Hsu, N. C., Bettenhausen, C., Lee, J., Redemann, J., Schmid, B., and Shinozuka, Y. (2016). Extending "Deep Blue" aerosol retrieval coverage to cases of absorbing aerosols above clouds: Sensitivity analysis and first case studies. *Journal of Geophysical Research: Atmospheres*, 121(9):2015JD024729.

Schaaf, C. B., Gao, F., Strahler, A. H., Lucht, W., Li, X., Tsang, T., Strugnell, N. C., Zhang, X., Jin, Y., Muller, J.-P., Lewis, P., Barnsley, M., Hobson, P., Disney, M., Roberts, G., Dunderdale, M., Doll, C., d'Entremont, R. P., Hu, B., Liang, S., Privette, J. L., and Roy, D. (2002). First operational BRDF, albedo nadir reflectance products from MODIS. *Remote Sensing of Environment*, 83(1–2):135–148.

Schaepman-Strub, G., Schaepman, M. E., Painter, T. H., Dangel, S., and Martonchik, J. V. (2006). Reflectance quantities in optical remote sensing—definitions and case studies. *Remote Sensing of Environment*, 103(1):27–42.

Schwartz, C. S., Liu, Z., Lin, H.-C., and Cetola, J. D. (2014). Assimilating aerosol observations with a "hybrid" variational-ensemble data assimilation system. *Journal of Geophysical Research: Atmospheres*, 119(7):4043–4069.

Shi, Y., Zhang, J., Reid, J. S., Holben, B., Hyer, E. J., and Curtis, C. (2011). An analysis of the collection 5 MODIS over-ocean aerosol optical depth product for its implication in aerosol assimilation. *Atmos. Chem. Phys.*, 11(2):557–565.

Snyder, W. C. (1998). Reciprocity of the bidirectional reflectance distribution function (BRDF) in measurements and models of structured surfaces. *IEEE Transactions on Geoscience and Remote Sensing*, 36(2):685–691.

Stowe, L. L., Ignatov, A. M., and Singh, R. R. (1997). Development, validation, and potential enhancements to the second-generation operational aerosol product at the National Environmental Satellite, Data, and Information Service of the National Oceanic and Atmospheric Administration. *Journal of Geophysical Research: Atmospheres*, 102(D14):16923–16934.

Taberner, M., Pinty, B., Govaerts, Y., Liang, S., Verstraete, M. M., Gobron, N., and Widlowski, J.-L. (2010). Comparison of MISR and MODIS land surface albedos: Methodology. *Journal of Geophysical Research: Atmospheres*, 115(D5):D05101.

Tanré, D., Bréon, F. M., Deuzé, J. L., Dubovik, O., Ducos, F., François, P., Goloub, P., Herman, M., Lifermann, A., and Waquet, F. (2011). Remote sensing of aerosols by using polarized, directional and spectral measurements within the A-Train: the PARASOL mission. *Atmos. Meas. Tech.*, 4(7):1383–1395.

Tao, M., Chen, L., Wang, Z., Tao, J., Che, H., Wang, X., and Wang, Y. (2015). Comparison and evaluation of the MODIS Collection 6 aerosol data in China. *Journal of Geophysical Research: Atmospheres*, page 2015JD023360.

Thomas, G. E., Poulsen, C. A., Sayer, A. M., Marsh, S. H., Dean, S. M., Carboni, E., Siddans, R., Grainger, R. G., and Lawrence, B. N. (2009). The GRAPE aerosol retrieval algorithm. *Atmos. Meas. Tech.*, 2(2):679–701.

Toller, G., Xiong, X., Sun, J., Wenny, B. N., Geng, X., Kuyper, J., Angal, A., Chen, H., Madhavan, S., and Wu, A. (2013). Terra and Aqua moderate-resolution imaging spectroradiometer collection 6 level 1b algorithm. *Journal of Applied Remote Sensing*, 7(1):073557–073557.

Van de Hulst, H. (1957). *Light scattering by small particles*. Wiley New York.

van der Werf, G. R., Randerson, J. T., Giglio, L., Collatz, G. J., Mu, M., Kasibhatla, P. S., Morton, D. C., DeFries, R. S., Jin, Y., and van Leeuwen, T. T. (2010). Global fire emissions and the contribution of deforestation, savanna, forest, agricultural, and peat fires (1997–2009). *Atmos. Chem. Phys.*, 10(23):11707–11735.

van Donkelaar, A., Martin, R. V., Brauer, M., Hsu, N. C., Kahn, R. A., Levy, R. C., Lyapustin, A., Sayer, A. M., and Winker, D. M. (2016). Global Estimates of Fine Particulate Matter using a Combined Geophysical-Statistical Method with Information from Satellites, Models, and Monitors. *Environmental Science & Technology*, 50(7):3762–3772.

Vaughan, M. A., Winker, D. M., and Powell, K. A. (2005). CALIOP Algorithm Theoretical Basis Document Part 2 : Feature Detection and Layer Properties Algorithms.

Verhoef, W. (1985). Earth observation modeling based on layer scattering matrices. *Remote Sensing of Environment*, 17(2):165–178.

Vermote, E. F., El Saleous, N., Justice, C. O., Kaufman, Y. J., Privette, J. L., Remer, L., Roger, J. C., and Tanré, D. (1997). Atmospheric correction of visible to middle-infrared EOS-MODIS data over land surfaces: Background, operational algorithm and validation. *Journal of Geophysical Research: Atmospheres*, 102(D14):17131–17141.

Vermote, E. F. and Kotchenova, S. (2008). Atmospheric correction for the monitoring of land surfaces. *Journal of Geophysical Research: Atmospheres*, 113(D23):D23S90.

Wang, Y., Lyapustin, A., Privette, J., Morisette, J., and Holben, B. (2009). Atmospheric Correction at AERONET Locations: A New Science and Validation Data Set. *IEEE Transactions on Geoscience and Remote Sensing*, 47(8):2450–2466.

Wang, Y., Lyapustin, A. I., Privette, J. L., Cook, R. B., SanthanaVannan, S. K., Vermote, E. F., and Schaaf, C. L. (2010). Assessment of biases in MODIS surface reflectance due to Lambertian approximation. *Remote Sensing of Environment*, 114(11):2791–2801.

Winker, D. M., Hostetler, C. A., Vaughan, M. A., and Omar, A. H. (2006). CALIOP Algorithm Theoretical Basis Document Part 1 : CALIOP Instrument, and Algorithms Overview.

Wiscombe, W. J. (1980). Improved Mie scattering algorithms. *Applied optics*, 19(9):1505–1509.

Wu, Y., de Graaf, M., and Menenti, M. (2016a). Improved MODIS Dark Target aerosol optical depth algorithm over land: angular effect correction. *Atmos. Meas. Tech.*, 9(11):5575–5589.

Wu, Y., de Graaf, M., and Menenti, M. (2016b). The Sensitivity of AOD Retrieval to Aerosol Type and Vertical Distribution over Land with MODIS Data. *Remote Sensing*, 8(9):765.

Wu, Y., de Graaf, M., and Menenti, M. (2017a). The impact of aerosol vertical distribution on aerosol optical depth retrieval using CALIPSO and MODIS data: Case study over dust and smoke regions. *Journal of Geophysical Research: Atmospheres*, 122(16):2016JD026355.

Wu, Y., de Graaf, M., and Menenti, M. (2017b). MODIS Aerosol Optical Depth retrieval over land considering surface BRDF effects. *manuscript*.

Wu, Y., Guo, J., Zhang, X., Tian, X., Zhang, J., Wang, Y., Duan, J., and Li, X. (2012). Synergy of satellite and ground based observations in estimation of particulate matter in eastern China. *Science of The Total Environment*, 433:20–30.

Xiong, X., Che, N., and Barnes, W. (2005a). Terra MODIS on-orbit spatial characterization and performance. *IEEE Transactions on Geoscience and Remote Sensing*, 43(2):355–365.

Xiong, X., Che, N., Guenther, B., Barnes, W. L., and Salomonson, V. V. (2005b). Five years of Terra MODIS on-orbit spectral characterization. volume 5882, pages 58820R–58820R–9.

Xiong, X., Chiang, K., Guenther, B., and Barnes, W. L. (2003a). MODIS thermal emissive bands calibration algorithm and on-orbit performance. volume 4891, pages 392–401.

Xiong, X., Erives, H., Xiong, S., Xie, X., Esposito, J., Sun, J., and Barnes, W. (2005c). Performance of Terra MODIS solar diffuser and solar diffuser stability monitor. volume 5882, pages 58820S–58820S–10.

Xiong, X., K Chiang, J Esposito, B Guenther, and W Barnes (2003b). MODIS on-orbit calibration and characterization. *Metrologia*, 40(1):S89.

Xiong, X., Sun, J., Barnes, W., Salomonson, V., Esposito, J., Erives, H., and Guenther, B. (2007). Multiyear On-Orbit Calibration and Performance of Terra MODIS Reflective Solar Bands. *IEEE Transactions on Geoscience and Remote Sensing*, 45(4):879–889.

Xiong, X., Sun, J., Esposito, J., Liu, X., Barnes, W. L., and Guenther, B. (2003c). On-orbit characterization of a solar diffuser"s bidirectional reflectance factor using spacecraft maneuvers. volume 5151, pages 375–383.

Xiong, X., Sun, J., Wu, A., Chiang, K.-F., Esposito, J., and Barnes, W. (2005d). Terra and Aqua MODIS calibration algorithms and uncertainty analysis. volume 5978, pages 59780V–59780V–10.

Xiong, X., Sun, J.-Q., Esposito, J. A., Guenther, B., and Barnes, W. L. (2003d). MODIS reflective solar bands calibration algorithm and on-orbit performance. volume 4891, pages 95–104.

Yang, L., Xue, Y., Guang, J., Kazemian, H., Zhang, J., and Li, C. (2014). Improved Aerosol Optical Depth and ångstrom Exponent Retrieval Over Land From MODIS Based on the Non-Lambertian Forward Model. *IEEE Geoscience and Remote Sensing Letters*, 11(9):1629–1633.

Yang, P. and Liou, K. N. (1996). Geometric-optics–integral-equation method for light scattering by nonspherical ice crystals. *Applied Optics*, 35(33):6568.

Young, S. A., Winker, D. M., Vaughan, M. A., Hu, Y., and Kuehn, R. E. (2008). CALIOP Algorithm Theoretical Basis Document Part 4 : Extinction Retrieval Algorithms.

Yu, H., Kaufman, Y. J., Chin, M., Feingold, G., Remer, L. A., Anderson, T. L., Balkanski, Y., Bellouin, N., Boucher, O., Christopher, S., DeCola, P., Kahn, R., Koch, D., Loeb, N., Reddy, M. S., Schulz, M., Takemura, T., and Zhou, M. (2006). A review of measurement-based assessments of the aerosol direct radiative effect and forcing. *Atmos. Chem. Phys.*, 6(3):613–666.

Zhang, J. and Reid, J. S. (2006). MODIS aerosol product analysis for data assimilation: Assessment of over-ocean level 2 aerosol optical thickness retrievals. *Journal of Geophysical Research: Atmospheres*, 111(D22):D22207.

Zhang, J. and Reid, J. S. (2010). A decadal regional and global trend analysis of the aerosol optical depth using a data-assimilation grade over-water MODIS and Level 2 MISR aerosol products. *Atmos. Chem. Phys.*, 10(22):10949–10963.

Zhang, J., Reid, J. S., Westphal, D. L., Baker, N. L., and Hyer, E. J. (2008). A system for operational aerosol optical depth data assimilation over global oceans. *Journal of Geophysical Research: Atmospheres*, 113(D10):D10208.

Acknowledgements

Looking back at the journey of my Ph.D. career, it was full of challenges and unknowns, but more gains and luckiness. This thesis would never be possible without the support and help from many people.

Firstly I would like to thank my promotor Prof. Massimo Menenti for offering me the opportunity to study in TUDelft. My Ph.D. career started when we met at RADI in Beijing in 2012 for the interview. When I came to Delft, I have been impressed by his spirit and energy that he always worked all day long from the early morning till the night (say the building closing time). This is because he was always busy. But even though so, I was encouraged to knock his door at any time to have a discussion with him as long as he was at his office. This thesis would never be finalized without his critical thinking and constructive comments on my research.

I want to express my sincere gratitude to Dr. Martin de Graaf. He became my co-promotor and daily supervisor in the second year (2013) of my study, introduced by Massimo. I am very grateful to him for his knowledge in the aerosol-related field that contributes a lot to my research. He always encouraged me to do the work on one's own but with sharing his useful skills and experience. To make me grow up quickly, he encouraged me to participate international conference to share my findings and discuss with the experts and scientists. Beside of this, I also would like to thank him for his translating part of my thesis into Dutch.

Special thank goes to Dr. Robert C. Levy at NASA for his kindly providing me the source code of Dark Target (DT) algorithm in the early stage of my Ph.D. career, as well as lookup table and aerosol parameters. This really helped me go much deeper into the aerosol retrieval research in details of physic and technique. Since then, I have become much more confident about my study. This thesis would never come out without his generous support.

I appreciate the colleagues from the section group of Optical and Laser Remote sensing, Roderik Lindenbergh, Ben Gorte, Seyed Enayat Hosseini Aria, Jochem Lesparre, Elyta Widyaningrum, Beril Sirmacek, Monica Herrero Huerta and Silvia Alfieri. I am very grateful to Ali Mousivand for teaching me how to use modtran software and explaining the surface BRDF. I am very enjoyable with my Chinese colleagues from this group, Junchao Shi, Haolu Shang, Jinhu Wang, Jie Zhou, Kaixuan Zhou, Yueqian Sheng. We had a lot of useful discussions about scientific research and life in The Netherlands. I am also grateful to Reenu Toodesh and Julien Chimot for their helpful communications.

I want to thank all my Chinese colleagues in the department, Prof. Jinliang Li, Prof. Xiaojun Luo, Prof. Yu Chen, Ling Chang, Yanqing Hou, Jianjun Ran, Pang Chen, Yunlong Li, Xiang Guo, Jiapeng Yin, Yangmeng Shi, Han Dun, Hongyang Ma, Hao Zhang and Hufeng Ming. I had a lot of funs during my study because of all of you. Particularly, I would like to thank Yu Sun for his generously helping me get through the tough time when my house was in repair (April, 2017). Many thanks have to go to my friend, Jianzhi Dong. Discussions with him contributed so much to my study and life.

I am very grateful to our secretaries, Lidwien de Jong, Debbie Rietdijk, Irma Zomerdijk, Suzanne de Hoog-Dollee and rebeca domingo for their kind help, such as extending my hospitality many times, providing me with one more monitor, and so on.

This thesis has been greatly improved with the constructive and useful comments by all the committee members. Thank you all for your very carefully reading and academic thinking of this thesis.

I would like to give my sincere gratitude to my Msc promotor Prof. Xiaowen Li at Beijing Normal University and co-promotor Prof. Jianping Guo at Chinese Academy of Meteorological Science. I am very glad to do the aerosol-related research with satellite data with your patience and supervision. I really appreciate Prof. Suhong Liu at Beijing Normal University for her encouraging me to pursue a doctor degree in the Netherlands.

Finally, I would like to thank my family. Their unconditional love and support always help me keep going and going...

Yerong Wu
Delft, December 2017

About the author

Yerong Wu was born in Xiangtan, Hunan, China, on 25 Oct. 1986. He became a bachelor student major in Geographical Information System in Capital Normal University (Beijing) in 2005. He obtained the bachelor degree of science in 2009 and won the outstanding graduate award. In the same year, he was admitted as a master student in Cartography and Geographical Information System in Bejing Normal University. During the master study, he mainly focused on estimation of particulate matter mass from satellite aerosol optical depth product using artificial neural networks, supervised by Prof. Xiaowen Li and Prof. Jianping Guo. He won the professional scholarship award in the second year of his master study. In June of 2012, he obtained the master degree of science. Later on (September), he was admitted as Ph.D candidate in section of Optical and Laser Remote Sensing in department of Geoscience and Remote Sensing at Delft University of Technology. He was mainly working on retrieval of aerosol optical depth over land by inverse modeling of multi-source satellite data, supervised by Prof. Massimo Menenti and Dr. Martin de Graaf.

List of publications

5. **Yerong Wu**, Martin de Graaf, and Massimo Menenti. MODIS Aerosol Optical Depth retrieval over land considering surface BRDF effects. *manuscript*, 2018.

4. **Yerong Wu**, Martin de Graaf, and Massimo Menenti. The impact of aerosol vertical distribution on aerosol optical depth retrieval using CALIPSO and MODIS data: Case study over dust and smoke regions. *Journal of Geophysical Research: Atmospheres*, 122(16):2016JD026355, August 2017.

3. **Yerong Wu**, Martin de Graaf, and Massimo Menenti. Improved MODIS Dark Target aerosol optical depth algorithm over land: angular effect correction. *Atmos. Meas. Tech.*, 9(11):5575–5589, November 2016.

2. **Yerong Wu**, Martin de Graaf, and Massimo Menenti. The Sensitivity of AOD Retrieval to Aerosol Type and Vertical Distribution over Land with MODIS Data. *Remote Sensing*, 8(9):765, September 2016.

1. **Yerong Wu**, Jianping Guo, Xiaoye Zhang, Xin Tian, Jiahua Zhang, Yaqiang Wang, Jing Duan, and Xiaowen Li. Synergy of satellite and ground based observations in estimation of particulate matter in eastern China. *Science of The Total Environment*, 433:20–30, September 2012.